IACMI/R0012-2021/3.2

Optimized Carbon Fiber Intermediate Development to Enable High-Volume Manufacturing of Lightweight Automotive

Author: Patrick Blanchard
Date: October 28, 2021

Final Technical Report
PA16-0349-3.2-01

Approved for Public Release.
Distribution is Unlimited.

Optimized Carbon Fiber Intermediate Development to Enable High-Volume Manufacturing of Lightweight Automotive Composites

Principal Investigators: Patrick Blanchard (Ford) and David Bank (Dow)

Organization: Ford Motor Company & Dow Chemical

Address: 2101 Village Rd, Dearborn, MI 48124

Phone: 313-390-6230

Email: pblanch3@ford.com

Co-authors: Lawrence Drzal (Michigan State University) Johnathan Goodsell (Purdue University), Dayakar Penumadu (University of Tennessee, Knoxville)

Date Published: (October 2021)

Prepared by:
Institute for Advanced Composites Manufacturing Innovation
Knoxville, TN 37932
Managed by Collaborative Composite Solutions, Inc.
For the
U.S. DEPARTMENT OF ENERGY
Under contract DE- EE0006926

Project Period:
(07/2017 – 05/2019)

Contributing Authors

Ford Motor Company
Patrick Blanchard
Jeff Dahl
Zachary Pecchia
Matthew Rebandt

Dow Chemical
David Bank
Jason Reese

Michigan State University
Lawrence Drzal,
Michael Rich
E. K. Drown
P. A. Askeland

University of Tennessee, Knoxville
Dayakar Penumadu
Matthew Kant

Purdue University
Johnathan Goodsell
Rebecca Cutting
Ben Denos
Anthony Favaloro
Drew Sommer

Table of Contents

Contents

Lists

List of Acronyms

1K	Single component (adhesive)
2K	Two component (adhesive)
3D	Three-dimensional
CAD	Computer-aided design
CAE	Computer-aided engineering
CAT scan	Computerized axial tomography scan
CF	Carbon fiber
CF-SMC	Carbon fiber sheet molding compound
CTQ	Critical-to-quality
DIC	Digital image correlation
DMA	Dynamic mechanical analysis
DSC	Differential scanning calorimetry
GPa	giga Pascals
HPLC	High-performance liquid chromatography
IACMI	Institute for Advanced Composites Manufacturing Innovation
ILSS	Interlaminar shear strength
IMR	Internal mold release
IPA	Isopropyl alcohol
MSU	Michigan State University
ORNL	Oak Ridge National Laboratory
PATTI	Pneumatic adhesion tensile testing instrument
PEEK	Polyetheretherketone
ROS	Random-orientated strand
RT	Room temperature
SEA	Specific energy absorption
SEM	Scanning electron microscope
SMC	Sheet molding compound
SPH	Smoothed particle hydrodynamics
TDIC	Thermal digital image correlation
Tg	Glass transition temperature
TMA	Thermal mechanical analysis
UD	Unidirectional
UTK	University of Tennessee Knoxville
UV	Ultraviolet
UVO	Ultraviolet ozone
XPS	X-ray photoelectron spectroscopy

List of Figures

List of Tables

1.0 Executive Summary

The ongoing pursuit of improved fuel economy and reduced greenhouse gas emissions has resulted in sustained interest for lightweight materials technologies. In this context, carbon fiber composites have captured the imagination of automotive engineers due to the potential to achieve substantial mass reduction when compared to traditional steel construction. That stated, the use of carbon fiber composites in automotive has been limited for the most part to premium supercars and other derivative platforms. In these cases, manufacturing costs are less of an obstacle to implementation, and the performance benefits of carbon fiber have enabled production of structures offering more than 50% weight savings. In practice, translating these low-volume demonstrations onto high-volume vehicle platforms has remained challenging. This can be attributed to several factors, with the absence of suitable high throughput production methodologies being a key impediment. To date, structural, crash critical components have relied upon manufacturing techniques born out of the aerospace industry. This has created a disconnect between automotive production systems that are accustomed to manufacturing multiple parts per minute and the aerospace technologies that have cycle times in the order of hours.

Consequently, the focus of this project is the development of manufacturing process technology for carbon fiber composites that can support a mainstream vehicle program at an assumed throughput of 100,000 vehicles per year. In practice, this translates to a part-to-part cycle time of less than 3 minutes. Project participation included contributions from a broad range of academic, industrial and national lab partners. The primary scope of work, being the development of new carbon fiber epoxy compounds that are stable at room temperature and suited to high throughput automated processing.

For project management, the work streams were divided into six key areas, with the lead organization in parentheses.

- Carbon fiber/epoxy materials formulation development and scale up (Dow)
- Simulation of discontinuous near isotropic meso-structure intermediates (Purdue)
- Simulation of mechanical performance of compression molded components (Purdue)
- Meso-Scale morphological analysis and correlation with structural performance (UTK)
- Paint and adhesion durability analysis (MSU)
- Demonstrator part design, prototype production, and validation testing (Ford).

The primary goal at the commencement of the project was development of a chopped carbon fiber sheet molding compound (SMC) that offered a three times improvement in tensile modulus over a comparable glass-based SMC. In addition to meeting mechanical performance targets, the resin kinetics were modified to achieve a processing cycle time of less than 3 minutes. Other critical-to-quality (CTQ) specifications were also stipulated to account for a broad range of materials and processing characteristics. To achieve the above, staff scientists at Dow Chemical created an extensive series of new epoxy blends for testing and validation. Throughout this development, a key challenge was attaining material performance goals without impacting processing behavior and paintability of finished components. The latter required a new internal mold release system being developed by Dow that was designed to complement the kinetics of the rapid cure epoxy.

As a complement to work studies at the industrial partners, the teams from academia executed a series of analytical and experimental studies to investigate potential factors influencing CF-SMC performance. Unit cell models were developed to capture the meso-scale representations of the fiber matrix architecture. Results of this analysis and subsequent morphological investigations led to the design of a novel composite derivative comprising carbon fiber platelets embedded in an epoxy matrix; the platelet size and aspect ratio playing significant role in final composite properties. This approach was a departure from previous research in CF-SMC development whereby bulk filamentization or disassembly of the carbon fiber rovings had been considered the most effective means of achieving both fiber wet through and wet-out. As the course of the academia studies progressed, the aspect ratio of the fiber constituents was further optimized before finalizing material attributes and processing conditions.

For the purposes of technology validation, the Ford team led a work stream devoted to the design, fabrication and testing of demonstration components. The carbon fiber SMC material has the potential to displace numerous stampings and castings on an automotive structure but ultimately vehicle closure applications were selected to showcase the abilities of the CF-SMC to achieve both mass reduction and business case for large complex structures. Using target properties established by the Dow staff scientists, the complete closure system for a full-size sedan decklid and a mid-size wagon liftgate were engineered. Prototypes for both applications were fabricated using production representative processing methods to allow for physical testing and performance validation of the CF-SMC structures. Following completion of a testing program that concluded with a FMVSS301 [27] 55 mph offset rear crash, the CF-SMC formulation was declared by the Ford team to have met all engineering requirements.

To summarize, the joint development activities during this project led to significant technical breakthroughs and achievement of all milestones. The result was the development of a novel, tack-free carbon fiber molding compound that is suited to automated processing. This combined room temperature stability, fast cure kinetics, and internal mold release system facilitates cycle times that are conducive to high-volume production. The VORAFUSE M6400 successfully passed technology validation at Ford and is now eligible for consideration on future production commercial vehicle programs.

2.0 Introduction

The never-ending drive for improved performance and increased efficiency demands ongoing innovations in material systems and the processes for component production. For many automotive applications, this creates a tension between the space or volume made available for a component design and the required performance in terms of stiffness, strength, and other functionality. Consequently, as the design space shrinks, the material options also become limited if performance and function are to be maintained.

A key deficiency in composite materials can be their relative stiffness when compared to metallic solutions. For example, the tensile modulus of isotropic materials such as steel, aluminum and magnesium is 210 GPa, 69 GPa, and 45 GPa, respectively. By comparison, chopped glass reinforced composites typically offer a modulus of between 5 GPa and 15 GPa. These deficiencies in intrinsic stiffness can be overcome through shape complexity and increased section height. However, many applications may not be able to expand the necessary design space in order to meet system level performance. In other words, the design space for adjacent components may be infringed upon as section size grows to meet stiffness targets.

A solution to the problem is a substitution of glass fiber reinforcement for carbon fiber. Standard modulus carbon fiber has a tensile modulus of around 240 GPa. Hence, even as a chopped fiber compound there remains an opportunity to compete more effectively against metallic solutions. Consequently, this project was focused on developing a carbon fiber-based sheet molding compound that offered more than a three times improvement in tensile modulus when compared to glass fiber SMC. But a transition from glass fiber to carbon fiber SMC is not a trivial undertaking. The diameter of carbon fiber (7 microns) is typically half that of glass, effectively increasing the surface area to be wet out during compounding and molding. Furthermore, compatibility of carbon fiber with typical SMC resins is limited, resulting in poor interfacial strength and limited improvement in overall part performance. This required the team to match the carbon fiber with an epoxy-based resin. This in itself introduced additional challenges as conventional epoxy systems are not conducive to handling requirements and manufacturing processes associated with high-volume automotive production. Therefore, beyond any fiber and sizing developments, a new epoxy system had to be developed to deliver the final carbon fiber SMC solution.

In parallel to technical development activities, the team also completed a deep dive into application opportunities. More than a hundred parts across multiple vehicle subsystems were investigated. The intent was to identify candidate parts that would benefit from a transition to a carbon fiber composite solution. In general terms, the increased modulus of the CF-SMC resulted in an ability to develop competitive design solutions when compared to many cast components produced from aluminum or magnesium. Large closure assemblies (liftgate and decklid) such as those demonstrated in this project also showed promise. Direct replacement of steel sheet metal assemblies proved to be more challenging depending upon the perceived needs of different vehicle programs and the corresponding tradeoff between weight reduction opportunities and resultant incremental cost. So overall, if applications had potential for transition away from steel to an aluminum or magnesium solution, then the carbon fiber SMC was worthy of consideration. Although it was noted that the benefits of reduced investment for the carbon composites were often undermined as annual production volumes increased. This can

be attributed to raw materials costs beginning to dominate total program costs as the number of vehicles produced over a model's lifetime increased. As a side note, it should be stated that exterior vehicle body panels were omitted from the business assessment study as the proposed CF-SMC material was not developed toward meeting exterior Class A surface finish specifications.

For ultimate consideration of the CF-SMC material for implementation into series production, an extensive design, verification and test plan was executed. By means of demonstration, liftgate and decklid closure systems were selected to evaluate the overall material performance and processing characteristics. A more complete description of the testing program executed at Ford Motor Company is described in the following sections. However, final conclusions for the test program demonstrated capability to meet all requirements, with the project successfully passing through an internal <Application Readiness> gateway. With successful completion of this phase of the project, the carbon fiber SMC is now under consideration for implementation on future model year vehicles under development.

3.0 Background

Carbon fiber composites have attracted considerable attention due to the potential for substantial mass savings, with many examples now implemented in the low volume luxury car market. However, migration to higher-volume applications has been hindered by the absence of both affordable material formats and high-volume manufacturing methods. Therefore, the work program executed under this joint development agreement has focused on the development of high-volume materials and manufacturing. The opportunity was made possible by combining Ford's capabilities and experience in design, testing, assessment of vehicle manufacturing economics and high-volume production with Dow's capabilities and experience in high-volume materials (carbon fiber, resin, and related manufacturing processes) development and supply. This industrial partnership was complimented with critical contributions from academic partners at Purdue University, University of Tennessee, and Michigan State University in addition to support from Oak Ridge National Lab. Together, the team was able to successfully generate materials and process technology to demonstrate cost-effective production of advanced carbon fiber composites in support of future high-volume vehicle programs.

As a foundation for development of the CF-SMC, the team leveraged work from some earlier conceptual studies between Ford and Dow focused on an aligned carbon fiber and epoxy resin chemistry to produce structural automotive components. This work required the development of novel processes and chemistry to achieve the following goals;

(1) tack-free haptics for automated handling.
(2) room-temperature shelf stability (> 30 days at 30°C).
(3) automated fast (< 1 minute) preforming.
(4) snap curing (< 2 minutes)/ultra-fast part processing (< 3-minute total cycle time).
(5) recycle of in-plant prepreg scrap.

This work was extended to develop a revised resin chemistry for compatibility with a chopped fiber SMC format while also adding additional functionality to assist with processing. Specifically, as an extension to the above, the team was tasked with delivering

(6) a discontinuous “random” carbon fiber intermediate format

- conducive to production of reasonably formless molding charges
- capable of charge flow during compression to fill complex 3D automotive tooling.

(7) novel internal mold release “IMR” chemistry to enable release without external mold release application.
(8) mechanical performance metrics demonstrating quasi-isotropic performance in molded plaques that exhibit 300 MPa strength and > 30 GPa stiffness.

3.1 Project Scope

Materials Characterization, Simulation and Development

The approach for creating the chopped fiber format included slitting of prepreg tape into platelets to form a molding material or blank. While this has been successfully implemented in commercial aerospace composites for small structural components, the technology has not been developed for large scale structural applications, nor has it been executed with rapid cure thermoset resin systems appropriate to automotive production rates. Furthermore, conventional sheet molding compound (SMC) materials are not typically developed for fiber volume fractions above 30%. On the contrary, adoption of a platelet geometry within the meso-phase provided the ability to optimize processing and performance characteristics such as flowability and tensile strength. Thus, the materials developed in this project were able to yield a new level of structural performance not possible with conventional SMC systems. The process proposed to produce carbon fiber epoxy compounds for testing and validation is shown in Figure 1.

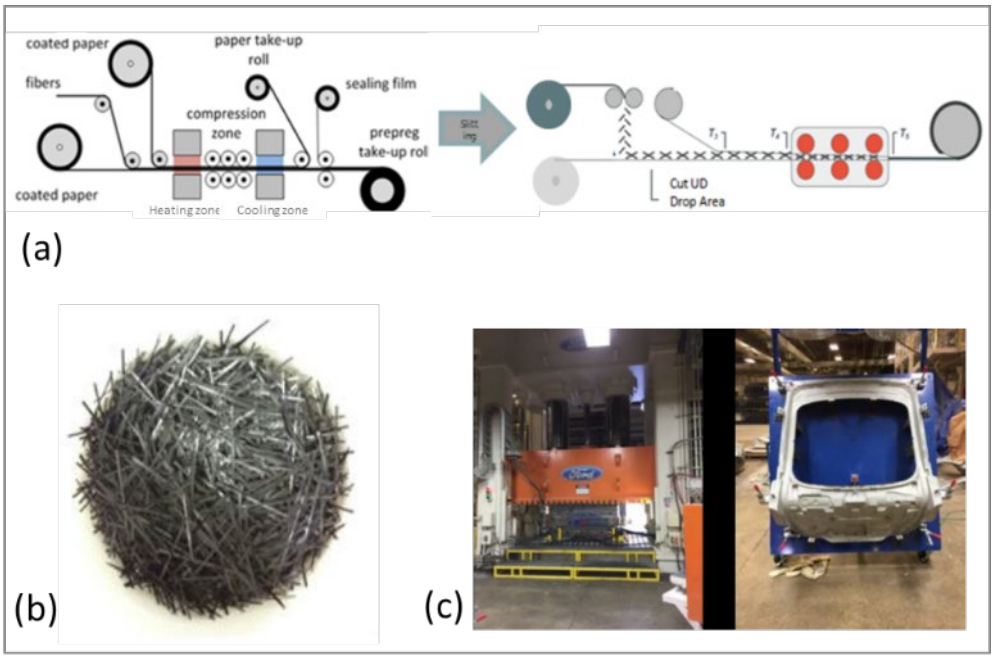

Figure 1. (a) Schematic of process envisioned to enable development of epoxy-based random fiber intermediate, (b) example of novel epoxy-based chopped “random fiber” intermediate, (c) compression molding press used to produce an automotive liftgate inner panel.

To complement the activities at Ford, Dow and IACMI Corktown, Purdue, MSU and UTK were

tasked with exploring the relationship between meso-scale structure and final mechanical properties. Simulation and experimentation were planned to examine translation of fiber modulus and tensile strength to composite properties as input to the meso-structure simulations. Multiple meso-structure geometries (random fiber intermediates) were examined to determine optimum platelet geometry to achieve the maximum tensile strength for the planar isotropic configuration. Predictions were made for optimum platelet architecture that would result in achieving target properties for materials produced via prepreg production, slitting and chopping, and compression molding.

Throughout these investigations, the modeling and experimental teams traded data to further refine the meso-scale models and improve upon the flow simulation capabilities. The models were further developed to capture cure-kinetics and anisotropic viscosities as a function of fiber orientation distribution and meso-structure geometry and fiber volume fraction. Rheo-kinetic models were developed to determine optimum time-temperature histories appropriate to establish levels of cure of the polymer matrix and induced shrinkage due to cure while elucidating the ability to predictably fill and pack large complex parts. Plaque-sized flat samples of several of the material compositions were formed and the mold coverage varied. By varying the blank size, it was possible to establish the mold coverage necessary for optimum molding conditions. Flow simulations were also used to determine optimum charge pattern, compression rates, knit line formation, and local meso-structure fiber orientation. Thus, fiber orientation distribution within the flat plaques was simulated for the squeeze flow conditions and subsequently measured using micro-CAT scans of all regions of interest in the plaques. Simulations and CAT scan results were compared for validation of the flow predictions.

Figure 2. Double dome compression molding tool.

To examine the geometric scale-up character of this innovative material system, the double dome mold geometry shown in Figure 2 was used in molding studies. Molding simulation of the material flow, state of cure and fiber orientation distribution within the double dome was carried out to determine regions of deleterious orientation state, lack of fill or incomplete fill. Micro-CAT scans of regions of interest were conducted to validate molding simulations. DMA measurements were taken to validate state-of-cure predictions. Ultimately, flow and heat transfer simulations were used to design the material charge geometry for the large-scale part molding studies.

In parallel to processing and analytical studies, a separate work stream was executed at Michigan State University toward surface characterization of the molded samples. A byproduct of using an epoxy-based matrix with the carbon fiber was the need to develop an appropriate internal mold release system that would promote uninterrupted production and minimum mold maintenance. Another consideration was the surface condition of parts in the context of adhesive bonding and paint adhesion. Therefore, the team at Michigan State executed a series of investigations to determine the effect of the internal mold release system on final surface characteristics, which would lead to insights into the adhesive bond and long-term paint durability.

To support this work, 30-by-30cm plaques were manufactured with the carbon fibers and epoxy matrix according to a range of temperature, time and pressure conditions expected to be encountered in manufacturing. Composite specimens were tested for modulus, strength and fracture toughness. Failure surfaces were examined with surface microscopic and spectroscopic analytical methods. The adsorption strength of the IMR to the CF surface in the presence of the epoxy constituents and during the curing process were also investigated. A final evaluation of adhesion durability included environmental testing of cured composite panels and aluminum adherends prepared according to accepted manufacturing procedures for automotive structural bonding. A priming and painting protocol based on industry practices was implemented to paint the composite panels identified above. Multi-material adhesive joint (aluminum to polymer composite) and paint adhesion mechanical tests as well as durability tests were conducted to assess the IMR role. Both adhesively bonded specimens and painted specimens were subjected to durability testing using Ford- and Dow-defined protocols involving cyclic exposure to salt, wet, and elevated temperature environments.

Scale-up of Material Production and Part Processing

To execute this portion of the program, facilities at IACMI Corktown were established to support the prepreging element of Figure 1a. Hence, the team was tasked with purchasing, installation and commissioning of the line to enable scale up of laboratory studies that had been completed at Dow beforehand to establish proof of concept. Material to be produced would determine the basic mechanical properties of building blocks that are required to accurately simulate the performance of 3D parts. A summary of the activities scheduled for the IACMI Corktown facility is as follows:.

(1) Commissioning a state-of-the-art prepreg line
   a. Scale-up of a novel epoxy chemistry based random carbon fiber intermediate
   b. Demonstration of concept and ability to achieve metrics (described above)
   c. Execution of a plan to increase prepreg throughput (target 8 m/min) without sacrificing mechanical performance.

(2) Implementing a state-of-the-art compression molding capability for large part molding
   a. Support of molding for relevant parts (decklid and liftgate)

Design Validation Testing

From an automotive perspective, final validation of any material system requires prove-out at a scale that is representative of the intended application. This includes not only manufacture of parts using production intent processes but also execution of an experimental test program that

will subject the parts to prescribed load cases. In the case of the rear closures (decklid and liftgate in Figure 3), this involved buildup of fully functional prototype assemblies for component and vehicle level testing. During each part of the test program, the CAE performance predictions were compared to physical testing to ensure adequate correlation. Ultimately, the test program was concluded with a carbon fiber SMC decklid assembly being mounted to a vehicle and subjected to a 55 mph rear offset crash. With testing complete, a final assessment of material performance was made based upon the potential applications under consideration.

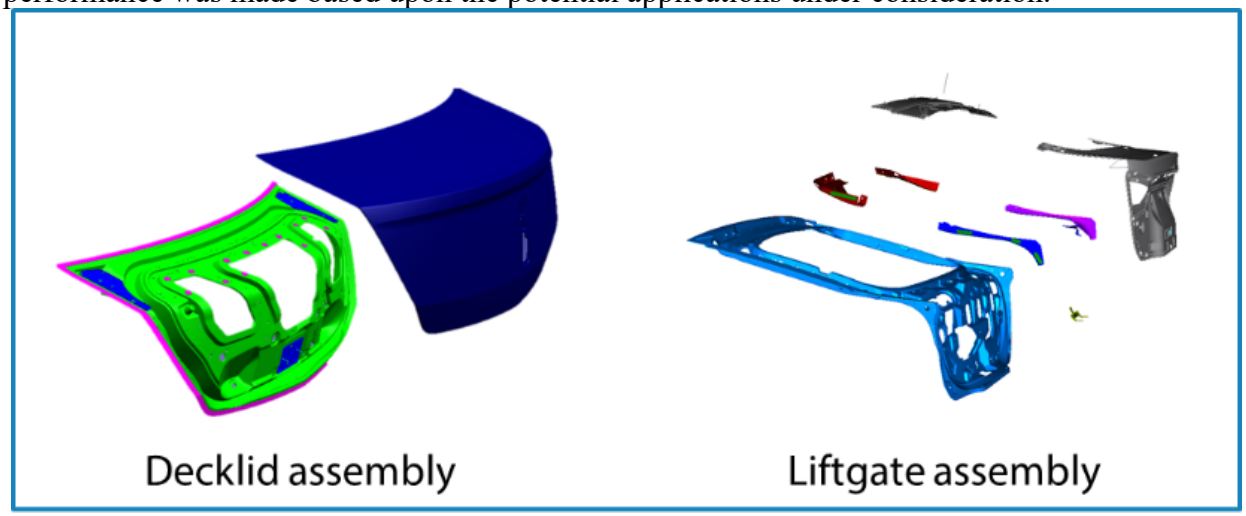

Figure 3. CAD rendering of decklid and liftgate assembly used to demonstrate material performance and processing characteristics of the platelet-based CF-SMC.

Project Milestones

For project management and tracking purposes, a set of milestones was agreed upon by the US Department of Energy, Advanced Manufacturing Office. These milestones, which coincide with Budget Periods 3 and 4 of the IACMI cooperative agreement, are shown in the table below.

Table 1. Project milestones

	Milestone or Go/No-Go	Title of Milestone	Lead Organization
Budget Period 3 (July 1st 2017 - March 31st 2018)	3.2.1.1	Delivery of a model enabling the simulation of impregnation of prepreg produced via hot melt processing of 186 gsm Unidirectional tape to the Dow VORAFUSE™ M6400 specification intended for the IACMI-MSU SUF implementation	Purdue
	3.2.1.2	Start-up of prepreg line at the IACMI-MSU SUF and validation of target throughput (8m/min) and mechanical performance of resultant novel epoxy based random fiber product	MSU
	3.2.2.1	Delivery of a model enabling the simulation of impregnation and mechanical performance (300MPa strength and >30 GPa stiffness) of prepreg produced via hot melt processing of 186gsm UD to the Dow VORAFUSE™ M6400 specification intended for the IACMI-MSU SUF implementation	Purdue
	3.2.2.2	Validate production of 10 Ford liftgate components that meet dimensional specifications derived from Ford part specifications and demonstrate consistent internal mold release function (i.e. no mold sticking) based on Dow epoxy carbon fiber molding compound (VORAFUSE™ M6400)	MSU
	3.2.3.1	Evaluate meso-scale structure prediction with experimentally measured meso scale morphology features (fiber orientation) at target location(s), for DD and/or B-pillar parts molded using VORAFUSE™ M6400 such that predicted static part mechanical performance correlates within 15% with actual performance	University of Tennessee
	3.2.4.1	Report out on the role of IMR modified epoxy on the surface properties of the cured composite panels; and identify the conditions causing it to affect the surface and its paintability and adhesive bonding performance as it pertains to the Ford lift gate application produced with a VORAFUSE™ M6400 inner structural molding and an Al outer	MSU
	3.2.5.1	Establish structural testing methods and characterize compression molded parts (Dow/Ford Double Dome) at sub-scale and part-scale level for fiber orientation at target location (s) such that part mechanical performance (lift gate) can be predicted within 15% of actual using simulation tools derived in subtask 3.2.3	University of Tennessee
	3.2.6.1	Simulation of lift gate part complete and correlation to actual crash results within 15%	Purdue
	Go/No-Go 3.2.1	Achieve part level material performance as measured by application testing such that Ford is willing to declare the subject epoxy random carbon fiber intermediate acceptable for specification on future vehicle platforms	Purdue, MSU
Budget Period 4 (April 1st 2018 - May 31st 2019)	3.2.1.1	Additional compaction units outlined in Phase 2 Litzler line program are operational, as demonstrated by processing >5m of prepreg.	MSU
	3.2.1.2	Refined technoeconomic model for platelet-based prepreg system based on process optimization and back-integration, with results summarized in a confidential white paper	Dow
	3.2.1.3	Production of prepreg and compression-molded composite needed for model validation and experimental testing	MSU
	3.2.1.4	White paper comparing of standard mechanical properties of molded prepreg from chopped unidirectional prepreg prepared from standard process and from the low-cost textile grade carbon fiber.	Ford
	3.2.2.1	Platelet flow model capable of designing prepreg charge placement for consistent material properties within two parts of complex geometry. Flow model summarized in a confidential final report reviewed with DOE.	Ford
	3.2.2.2	Model capable of predicting dimensional changes during fabrication of a Ford designated carbon fiber component into an assembly with dissimilar materials.	Purdue
	3.2.2.3	Testing protocol (including part and testing geometry) necessary to obtain material data card parameters and predict composite material response to crash test.	Purdue
	3.2.3.1	Internal report documenting key failure modes associated with platelet-based composites as a function of platelet orientation	Purdue
	3.2.3.2	Confidential final report evaluating routes to characterize platelet orientation in complex part geometries, including at least one Ford-designated component	UTK
	3.2.3.3	Determine the magnitude of residual stress in a complex platelet-based molded component and validate its importance in controlling part dimensions	UTK
	3.2.4.1	Internal report prioritizing approaches for surface preparation of carbon fiber composite based on commercial accessibility, expense, and positive impact on adhesion	UTK
	3.2.4.2	Internal report of recommended adhesive rheo-kinetic and mechanical properties and application conditions for at least one Ford-designated component	MSU
	3.2.5.1	Internal report summarizing options for novel resin chemistries and recommending a specific class for further development	MSU
	3.2.5.2	Internal report summarizing standard static mechanical properties for plaques prepared from UD composites with next-generation prepregs.	Dow
	3.2.1 Go/No-Go	Achieve part level material performance as measured by application testing such that Ford are willing to declare the subject epoxy random carbon fiber intermediate acceptable for specification on future vehicle platforms	Dow
	3.2.2 Go/No-go	Project leadership will make a decision on the pursuit of prepreg with an alternate resin system based on cost-benefit analysis.	Ford

4.0 Results and Discussion

The sections that follow describe collaborative efforts across the project partners in support of meeting the declared project milestones. These results are broken down into the following key activities:

4.1 Critical-to-quality characteristics for materials and processing.
4.2 Material modeling and process simulation.
4.3 X-ray tomography and thermal digital image correlation.
4.4 Surface analysis and adhesive bond durability.
4.5 Validation of materials processing and performance.

4.1 Critical-to-Quality Characteristics (CTQs)

To ensure development of high-performance composite materials, ready for high-volume manufacturing, detailed critical-to-quality (CTQ) metrics were established for processing speed, molded part Tg, and mechanical performance. A few relevant CTQs are shown in Table 2.
A key CTQ for the CF-SMC is a cured Tg higher than the cure temperature when cured for two minutes at ~150°C. A Tg > 150°C allows a part compression molded at around 150°C to be released while still hot without warping. That is, it enables parts to have sufficient integrity to be demolded without first cooling the mold and part, which in turn enables shorter molding cycle times. In addition, a Tg > 150 °C provides a composite material with the property of high heat distortion temperature, which is needed for demanding applications.

Table 2. Key processing/property requirements

Process/Property		**Required performance**
SMC storage stability		50 days at ≤ 40°C
Molding		Compression molding
Mold temperature		145°C155C
# of parts between mold maintenance		1000
Cure speed (resin cure kinetics)		< 2 min @ 150°C (DSC)
Degree of cure after molding		> 95%
Cured Tg		150°C–160°C (DMA)

From a processing perspective, maintaining a cycle time of 3 minutes per part with 1000 parts molded between applications of an external mold release is essential for uninterrupted production. Epoxy polymers, being excellent adhesives, bond tenaciously to metals, making it necessary to utilize a release agent so that parts can be quickly and easily removed from the metal mold without damage or distortion. Internal mold release agents are preferred because they eliminate the need for frequent application of external release agent to the mold, thereby increasing productivity and reducing part cost.

Influence of Aspect Ratio on Performance of the Novel CF-SMC Materials
The CF-SMC system developed is based on an epoxy resin formulation designed to be compatible with an e-coat process for the vehicle body in white. In practice, this means tolerating the thermal exposure during the e-coating and paint processes. The use of carbon fiber as the polymer reinforcement increased stiffness by approximately threefold over glass-based SMC products, while also offering substantial improvement in strength. Figure 4 demonstrates the targets of strength and stiffness for material development.

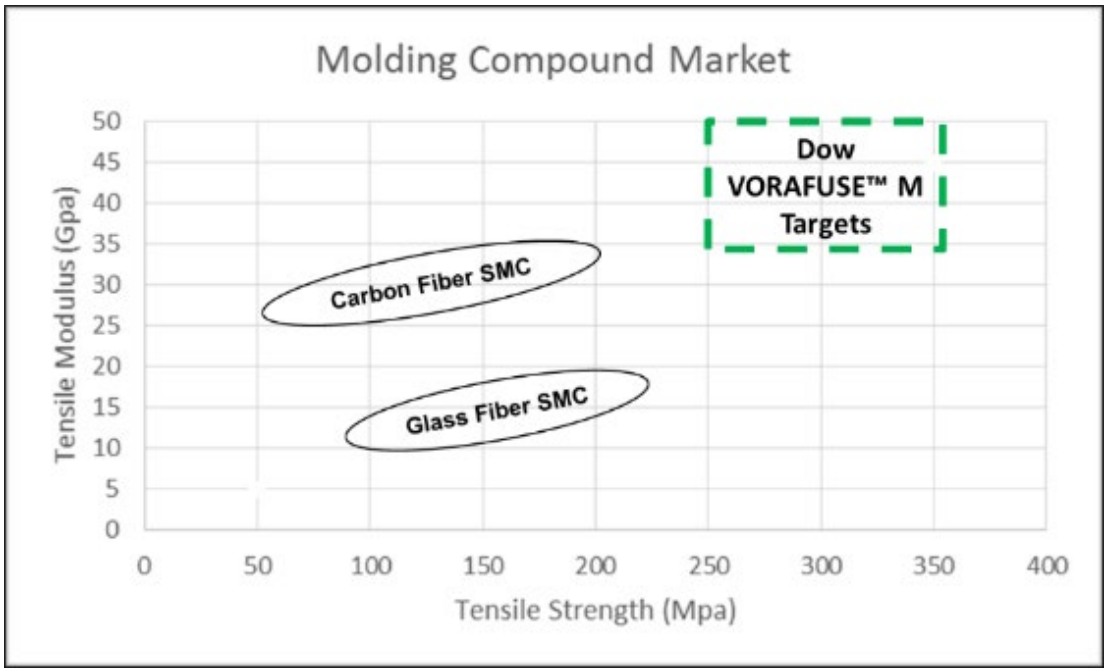

Figure 4. Market for modulus vs strength for SMC systems

Key challenges to be resolved prior to meeting these targets included:

- Achieving strength and stiffness while allowing material to flow during the compression molding cycle to create complex 3D geometry.
- Infusing the carbon fiber to reduce voids in a high-volume production rate.
- Defining a repeatable fiber aspect ratio to achieve predictable performance.

The physics of the carbon fiber aspect ratio controls both physical properties and the ability to flow the CF-SMC during compression In production, the platelets are produced in a two-step operation. First, a prepreg tape is slit down the length to create a tape of desired width. Then a chopper is used to cut the tape to the prescribed length. The length and thickness dictate the aspect ratio. The challenge was to establish a fiber aspect ratio that provided strength and modulus in the target range and provided enough flow during compression molding. This was essential if the materials were to be suited to complex 3D part geometries. For example, a fiber aspect ratio of < 10 may provide an excellent flow material with poor physical properties. A fiber aspect ratio of > 100 may provide excellent physical properties but near zero flow. The zero flow material may be useful in low production volume, simple geometry parts; however, these designs were not the target of this development. Ultimately, a controlled range of aspect ratios

was defined that was able to yield both material and processing attributes required by the components under investigation. Initial processing and mechanical property testing were completed using a 305-mm by 305-mm flat plaque mold. Table 3 provides a summary of key physical properties for samples excised from molded panels.

Table 3. Representative properties for Novel Carbon Fiber SMC

	VORAFUSE™ M 6400 Sheet Molding Compound – Typical Molded Properties			
Property – Molded Plaque Composite	Method	Units	Fiber Aspect Ratio L/W = 17	Fiber Aspect Ratio L/W = 34
Density	ASTM D792	g/cm3	1.5	1.5
Fiber Content	ASTM D3171 Method 1, procedure B	Wt %	60	60
Resin Content		Wt%	40	40
0º Tensile Strength at Break, Average	ASTM D3039	MPa	275	319
0º Tensile Strength at Break, Std Dev			28	44
0º Tensile Modulus, Average		GPa	42	50
0º Tensile Modulus, Std Dev			2.9	3.7
0º Tensile Elongation, Average		%	0.70	0.64
0º Tensile Elongation, Std Dev			0.06	0.08
0º Compressive Strength, Average	ASTM D6641 Procedure B, Tabbed	MPa	324	347
0º Compressive Strength, Std Dev			31	26
90º Tensile Strength at Break, Average	ASTM D3039	MPa	279	302
90º Tensile Strength at Break, Std Dev			31	69
90º Tensile Modulus, Average		GPa	43	49
90º Tensile Modulus, Std Dev			5.9	8.8
90º Tensile Elongation, Average		%	0.69	0.64
90º Tensile Elongation, Std Dev			0.06	0.05
90º Compressive Strength, Average	ASTM D6641 Procedure B, Tabbed	MPa	331	309
90º Compressive Strength, Std Dev			30	45
ILSS, Short Beam Shear, Average	ASTM D3518	MPa	55	58
ILSS, Short Beam Shear, Std Dev			5.2	5.0
0º Flexural Strength, Average	ASTM D 7264	MPa	482	522
0º Flexural Strength, Std Dev			78	102
0º Flexural Max Strain, Average		%	1.76	1.56
0º Flexural Max Strain, Std Dev			0.36	0.30
0º Flexural Chord Modulus, Average		GPa	32	39
0º Flexural Chord Modulus, Std Dev			5.1	6.9
Onset Tg (pk storage modulus)	ASTM D 5418	°C	127	132
Tg (peak tan delta) by DMA			159	160

4.2 Material Modeling and Process Simulation

Simulation studies within this project considered the effects of the material and manufacturing process on the static and crash performance of structures fabricated from CF-SMC. The sequence of modeling simulation is illustrated in Figure 5. Models were developed to aid in the design of the material system architecture by modeling the effects of platelet morphology on resulting processability and mechanical performance. The material meso-structure arising from the compression molding process was predicted by modeling the anisotropic flow characteristic of compression molding process. This is illustrated by considering two charge patterns and predicting the flow fronts that arise during the compression molding process in addition to the resulting platelet orientations. The models thus provide a tool to predict the effect of charge placement on resulting platelet orientations and thereby on the overall performance of the part. The molding models were validated through comparison of experimental short shots of a double-dome geometry. Microscopic investigation of the platelet orientations was also performed at selected regions in this part. The performance models considered the effect of the platelet orientations arising from the manufacturing process and predicted the resulting mechanical stiffness and strength. Finally, the crash performance of parts fabricated from CF-SMC was modeled. While the crash model was applied to predict the performance of the liftgate inner under assumed loading conditions, the model was validated using experimental lab-scale crush tubes. Details of each of the models and the experimental validation are contained in this report.

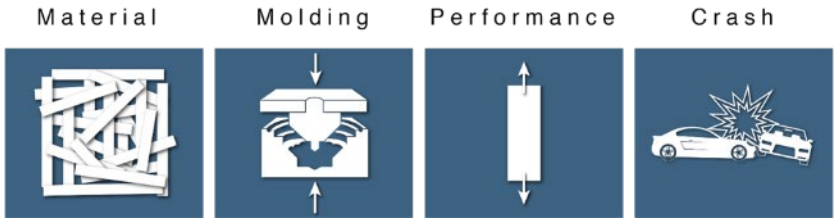

Figure 5. The modeling considered the effects of the material and manufacturing process on the static and crash performance of structures fabricated from CF-SMC.

4.2.1 Modeling Approach

The performance of structures produced with CF-SMC is highly dependent on platelet orientation. Therefore, an anisotropic viscosity model was developed to capture the flow behavior of CF-SMC to predict the platelet orientations resulting from the manufacturing process. Flow simulation–informed performance models included static stiffness and strength and crash behavior. The static strength model accounts for the discontinuous nature of the CF-SMC by assigning local material orientation to each finite element. The crash behavior was also characterized and models developed to predict crash performance. These simulation predictions were validated on crush tube geometries. However, simulation models, workflow and results were ultimately implemented for predicting the manufacturing and performance of the liftgate.

Aside from platelet orientation, a key parameter influencing the CF-SMC performance is the platelet aspect ratio, defined as the length-to-thickness ratio of a platelet. As has been identified previously [1]–[3], the platelet aspect ratio has significant influence on both the processability

and final performance of the CF-SMC component. As the addition of collimated fibers increases the viscosity of the system, particularly in the fiber direction, one measure of processability is the ratio of the neat resin viscosity, η to the system extensional viscosity, η_{xx}, of a suspension with a planar random orientation distribution. A measure of performance is the strength of a tensile coupon fabricated from an array of platelets whose orientation is uniformly distributed in the plane.

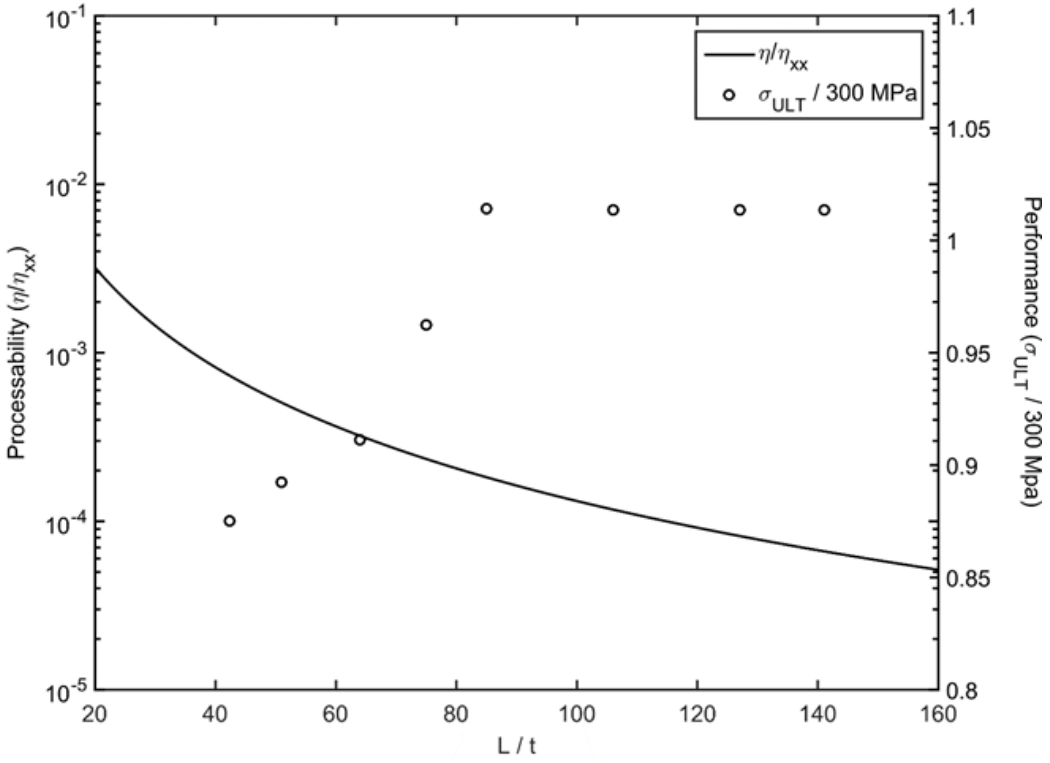

Figure 6 . Platelet aspect ratio significantly affects processability and performance.

The effect of platelet length to thickness, L/t, on processability and performance is shown in Figure 6. It is observed that processability decreases with increased aspect ratio; longer fibers are harder to process. Conversely, it is observed that increasing platelet aspect ratio increases strength, to a point, after which the strength of the system does not increase with increasing platelet length. This is consistent with observations reported in [1]–[3]. Thus, there is a maximum aspect ratio beyond which processability decreases without increase in strength. For this material system, this "sweet spot" is at an aspect ratio of approximately 85 and is consistent with the range in which Dow engineered the CF-SMC.

Significant portions of this work have been presented previously, including most recently at the CAMX Expo in 2019, held in Orlando, FL [4]. For completeness, significant portions of that work are reproduced in entirety. In addition, recent results beyond that work are also presented herein. The modeling and simulation section is organized as follows: The need for an integrated

simulation workflow to predict manufacturing-informed performance is introduced. An overview of the molding simulation to capture anisotropic flow, together with experiments to validate flow and platelet orientation phenomenon in the double dome geometry, is presented. Static strength and stiffness predictions for regions of the dome are presented and compared against experimental results from tensile tests of coupons excised from corresponding regions of the dome. The methodology for characterizing and predicting crash behavior of specimens fabricated from CF-SMC is presented.

4.2.2 Development of an Integrated Workflow

The high degree of variability in platelet orientation makes it difficult to immediately assume a uniform state of quasi-isotropic or uniform random orientation equivalent properties. The orientation state's dependence on flow during the manufacturing process requires flow analysis to account for any significant reorientation. However, incorporating the results of any flow simulation into a finite element model for stiffness, strength, or crash analysis with the correct level of detail is the next challenge. Taking a complete volume orientation average, such as the second order orientation tensor, from flow simulation and applying it over an entire model is likely to smear out important local stochastic morphologies. Commercial mapping tools, such as Digimat-MAP, can transfer local orientation and other details from a number of simulation and model outputs onto a target mesh, and output anisotropic, orientation tailored material models for every element [5]. In cases where a direct mapping is unreasonable and assigning homogenized properties is also insufficient, Digimat-FE can be used to generate a stochastic set of platelet-like inclusions with a target orientation tensor for a rectangular prism-shaped model. An alternate approach is to map the orientation data directly into a finite element model and allow the solver to handle material properties with a local orientation state in each element. This also allows for a single orthotropic material definition and lends itself to the use of user subroutines that can be customized for desired failure models and results visualization.

The material system specific workflow proposed for CF-SMCs is similar to that of SMCs (sheet molding compounds) by Görthofer, et al. [6]. From initial material charge shape and size to the crash response of molded CF-SMC parts, modeling and experimental validation are presented to highlight individual capabilities that fit into a larger workflow.

4.2.3 Orientation State Prediction and Validation

The orientation of fibers in discontinuous composites is widely known to greatly affect mechanical properties [7]. Herein, a previously developed flow simulation method [8], [9], and modeling effort on a double dome geometry [10] is validated versus experimental orientation measurements using a newly developed microscopy method for nearly elliptical cross-section fibers [11].

Compression Molding Flow Simulation

To briefly summarize the method, Abaqus/Explicit with a constitutive model implemented through a vumat user subroutine and the smoothed particle hydrodynamics (SPH) method were utilized as the simulation framework for compression molding, such that a large deformation, Lagrangian simulation capability is available. Within this numerical framework, a fully coupled anisotropic viscosity model is implemented, such that the evolving fiber orientation affects the

viscosity while the flow field evolves the fiber orientation. Fiber orientation evolution is achieved through direct affine motion of test fibers using the available deformation gradient (equivalent to Jeffery's equation) [9], [12], while the constitutive model is given as:

$$\boldsymbol{\sigma} = \mathrm{dev}\big(2\eta_{23}\{\mathbf{D} + 2\big(R_\eta - 1\big)\mathbb{A}\colon \mathrm{dev}(\mathbf{D})\big) + K\{\det \mathbf{F} - 1\}\mathbf{I}$$

where $\mathbf{F}$ is the deformation gradient, $\mathbf{D}$ is the rate of deformation tensor, η_{23}, and R_η are the shearing viscosity and anisotropy ratio (i.e., ratio of the extensional viscosity in the fiber direction to the extension viscosity transverse to fibers), respectively, K is a penalizing bulk modulus to enforce near incompressibility, and $\mathbb{A}$ is the fourth order orientation tensor [13]. This model is leveraged herein to study the effect of charge design on the resulting fiber orientation state and, later, mechanical performance of a double dome geometry.

Specifically, the charge orientations shown in Figure 7 were used with one charge initially oriented transverse to the long direction of the double dome geometry (transverse charge) and one charge initially oriented coaxial to the long direction of the geometry (axial charge). Due to the resulting flow upon compression molding, the transverse charge experiences flow conditions similar to planar extension, while the axial charge experiences biaxial extension. The resulting flow patterns as compared to experimental short shots are shown in Figure 8.

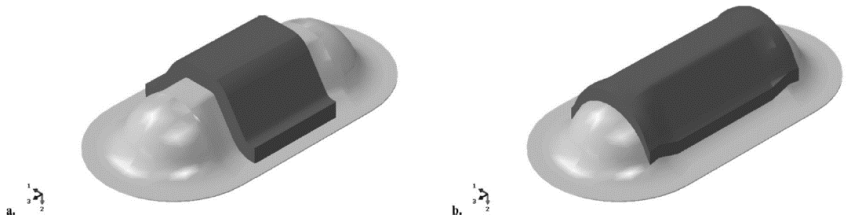

The resulting orientation states from the two different flow conditions experienced can be seen in general by observing Figure 9(c). Here, the second order orientation tensor [13], $\mathbf{A}_{aa}$, component along the axial direction of the double dome is shown from a top view. This component indicates the degree of alignment in this direction.

To compare with the microscopy results of the next section, path plots are generated by averaging the orientation state in 150-mm-length regions similar to that of a tensile bar. The resulting degrees of alignment along the axial direction, $\mathbf{A}_{aa}$, and transverse direction along the surface, $\mathbf{A}_{tt}$, (i.e., transverse to the axial direction and the normal direction) are shown in Figure 9(a) for the transverse charge and Figure 9(b) for the axial charge with Figure 9(d) showing the coordinate system and averaging region used for these plots with $x = x_1/W$ where W is the half-width. The cross-hatched regions of the figures are regions where the dome is curvilinear, making experimental investigation difficult.

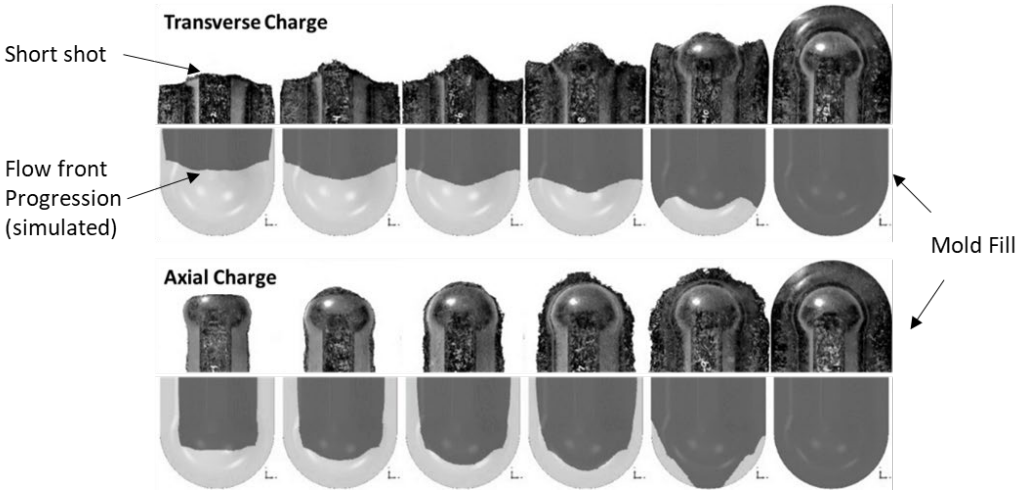
Transverse Charge
Short shot
Flow front
Progression
(simulated)
Mold Fill
Axial Charge

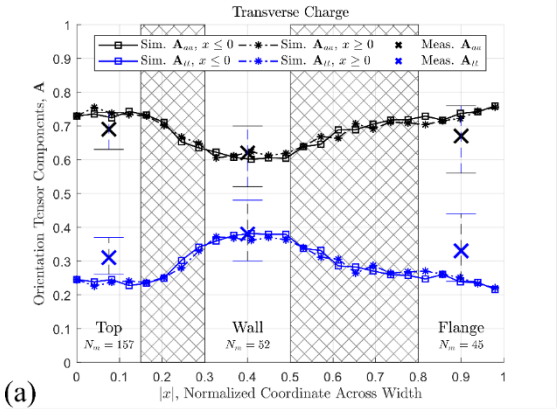
Transverse Charge
Orientation Tensor Components, A
|x|, Normalized Coordinate Across Width
Top
Wall
Flange
(a)

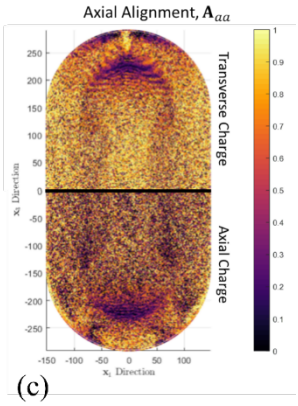
Axial Alignment, $\mathbf{A}_{aa}$
Transverse Charge
Axial Charge
(c)

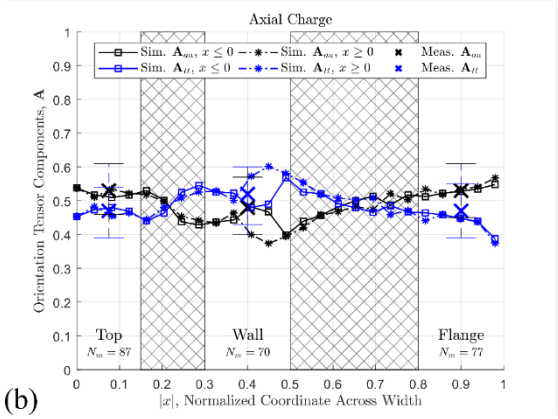
Axial Charge
Orientation Tensor Components, A
|x|, Normalized Coordinate Across Width
Top
Wall
Flange
(b)

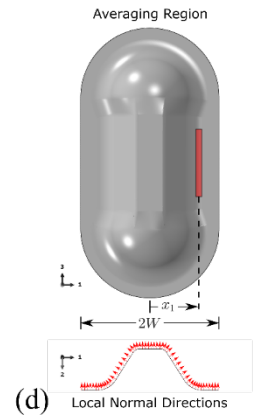
Averaging Region
2W
Local Normal Directions
(d)

Validation with Microscopy

Microscopy at 100x or 200x magnification was used to investigate the double dome geometry at the same six locations for each initial charge shape. For each location, a 25mm-wide section was excised from the part, mounted in epoxy, and polished. Within each 25mm-wide section, two or three individual subregions as wide as the local part thickness were isolated for orientation analysis. These subregions were not immediately adjacent, since that would essentially duplicate measurement of many of the same platelets; instead they were taken from the ends and middle of the 25mm-wide polished section. In order to determine fiber and platelet orientation for the fibers, which have a kidney-bean-shaped cross section, the work of Sharp, Goodsell, and Favaloro [11] was implemented via Matlab script, as shown in Figure 10.

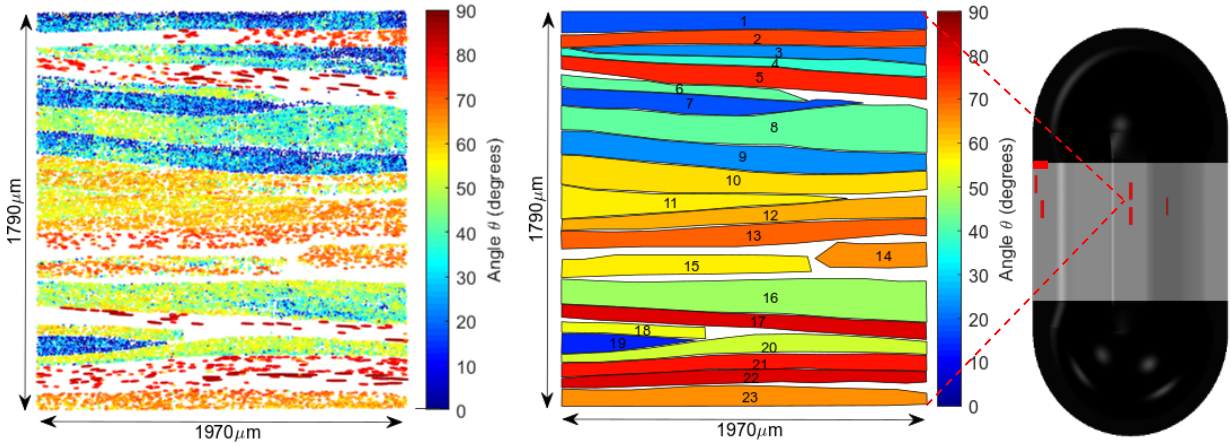

Figure 10. Individual fiber (left) and median platelet angle, θ, (center), for example micrograph sub-region of axial charge double dome (microscopy locations shown as red lines on model to right), enables validation of platelet orientation predictions from flow SI.

For each subregion, the Matlab script isolated the fiber cross sections into platelets (fiber bundles), performed preprocessing to binarize and watershed these fiber cross sections as individual particles, rejected particles that were extreme outliers within the given platelet, then fitted ellipses to the remaining fiber cross sections. The geometric descriptors of the fitted cross-section ellipse sets and known major and minor axis dimensions for zero-degree fibers were then used as input for the algorithm of Sharp et al., yielding the results seen in Figure 10.

As a result, the microscopy results for 40 or more platelets per region are available to validate local orientation state at the top, wall, and flange locations for simulation of the flow of both the axial and transverse charge types. The average axial and transverse orientation tensor terms, $\mathbf{A}_{aa}$ and $\mathbf{A}_{tt}$, for the region indicated in red on the model in Figure 9 (d) as swept along the x_1 direction are shown for each charge type in Figure 9(a) and (b). The microscopy-measured axial and transverse terms are also plotted at their measured locations, including error bars to represent sampling from a natural closure-based distribution measured using the number of platelets included in each **A** component measurement.

The reorientation trends of platelets, and their aligned constituent fibers, is clearly observed in both the simulation and microscopy results for the transverse charge. The axial charge has much subtler reorientation that is nonetheless captured by simulation and confirmed by microscopy if observing the measured values. The error bars on the microscopy are a helpful reminder that the measurements taken are from a limited set of local platelets. The simulation results are taken from a larger set of simulation particle orientations but could also be represented with a form of error bars, if desired. This is all to say that the CF-SMC system is still significantly heterogeneous at the scales being observed. In each case, the comparison is quite favorable.

CF-SMC Static Performance Modeling

Virtual tensile coupons were created in Abaqus/Standard using a stochastically generated set of platelets with orientations based on the regional flow simulation results for each charge, similar to the previous work of Kravchenko [14]. The tensile bar models were generated to have the same 152.4-by-25.4-mm gage area as excised experimental samples, where the thicknesses were 1.6 mm, 1.76 mm, and 1.72 mm to match the wall, top, or flange measured specimen thicknesses, respectively. Each "platelet" in the tensile bars was given the same, nominal 25.4-by-4.75--0.08-mm size as the actual molded platelets and placed at a randomly generated center point in the bar geometry with an in-plane orientation angle randomly selected from an orientation distribution. The orientation distribution was made using the natural closure method from an orientation tensor of the sampled flow-simulation results for the given wall, top, or flange region. The C3D8 solid elements where each "platelet" domain was defined, were given the platelet orientation as their local material coordinate system. In short, the flow simulation results for each region were sampled and a set of five bars were generated with platelet-like domains based on each region's orientation.

For validation of mechanical properties, tensile coupons were excised from two double dome geometries. For each material charge type, one double dome yielded two top, four wall, and two flange coupons. Using failure criteria reported in [1] – [4], five virtual bars were created for each region of each charge type. On average, the dome that had an initially transverse oriented material charge had higher stiffness and strength in its axial direction as seen in Figure 11. This is not surprising as the material flow causes bulk stretching along the part long axis and reorientation of platelets along the same direction. Each region does, however, experience this reorientation to different degrees such that the regional (top, wall, and flange) mechanical properties have different averages and variability.

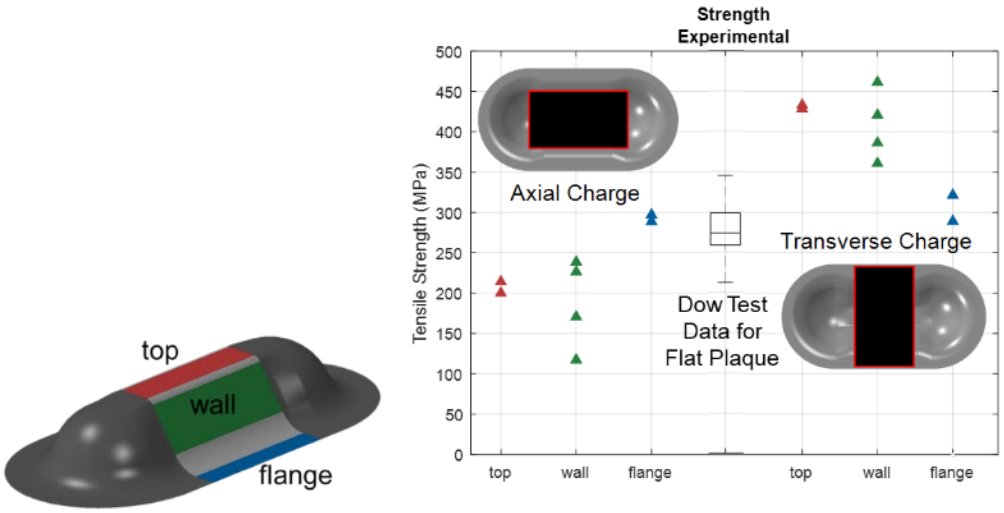

.

The finite element models of tensile bars of the same size and containing orientation informed meso-structures from the corresponding regions in flow simulation results show the same overall strength and stiffness trends, as shown in Figure 12.

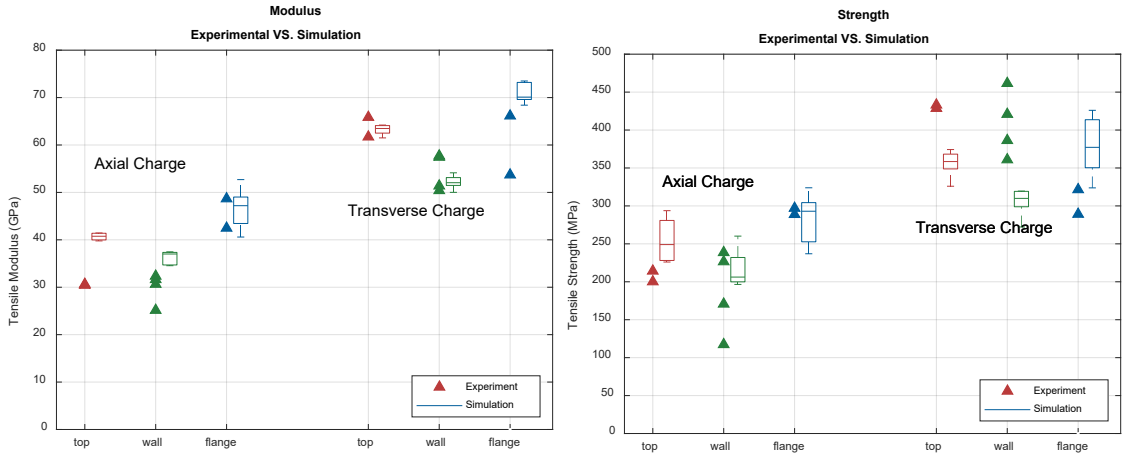

The simulated, or virtual, coupons capture the macro performance trends caused by different initial material charge shapes and some of the subtler trends between regions within each charge. There are some morphological realities present in the experimental bars that are not currently captured in the virtually generated bars, such as matrix-rich regions near platelet ends or substantial platelet distortion near tooling lateral boundaries, which may explain some missed

comparisons, but for a limited data set the comparison is very informative. This proves for the studied material system that if sufficient platelet morphology is captured in a model, it will at worst represent the qualitative effects on performance of different local material flow, and at best capture the mean behavior and its variability.

CF-SMC Crush Behavior

The crush behavior of CF-SMC was characterized experimentally using hollow crush tube component tests. The tubes had 50.8-mm outer diameters, 100-mm lengths, and average thicknesses of 2 mm. A bladder molding process with a composite additive manufactured tool that applied pressures up to 6.9 bar (100 psi) was used to manufacture the tubes [15], [16]. A 45° bevel was machined into one end of the samples to ensure progressive failure initiation. The tubes were crushed quasi-statically at a speed of 4mm/s.

In addition, a series of continuous fiber crush tubes with cross-ply laminates were manufactured with varying hoop to axial fiber ratios in stable and unstable layups. Consistent stable crushing of continuous fiber tubes was obtained when at least one ply of hoop fibers was on the external surface of the tube (stable layup). Unstable crushing was seen when axial fibers were on the external surface of the tube (unstable layup). Therefore, for each hoop-to-axial fiber ratio, stable and unstable laminates were made and tested. The continuous fiber tubes were manufactured with the same parent prepreg tape as the CF-SMC tubes. The specific energy absorption (SEA) of the crush tubes was calculated using the stable crushing load, the height, and the weight of the individual samples. The SEA of the continuous fiber and CF-SMC were plotted against the effective axial laminate stiffness of the layup in Figure 13. The laminate stiffness of the CF-SMC was approximated by a 2D random platelet orientation distribution with $\mathbf{A}_{11} = \mathbf{A}_{22} = 0.5$.

As the effective laminate stiffness increases, the SEA also increases for both the stable and unstable layups. It is clear that the stable layup consistently absorbed more energy than the unstable layup of the same effective laminate stiffness. The CF-SMC tubes compare well to tubes of similar laminate stiffness. However, there is significant SEA variation among the CF-SMC tubes tested. This could be due to variations in the platelet orientation distribution, as well as slight thickness and diameter differences from tube to tube.

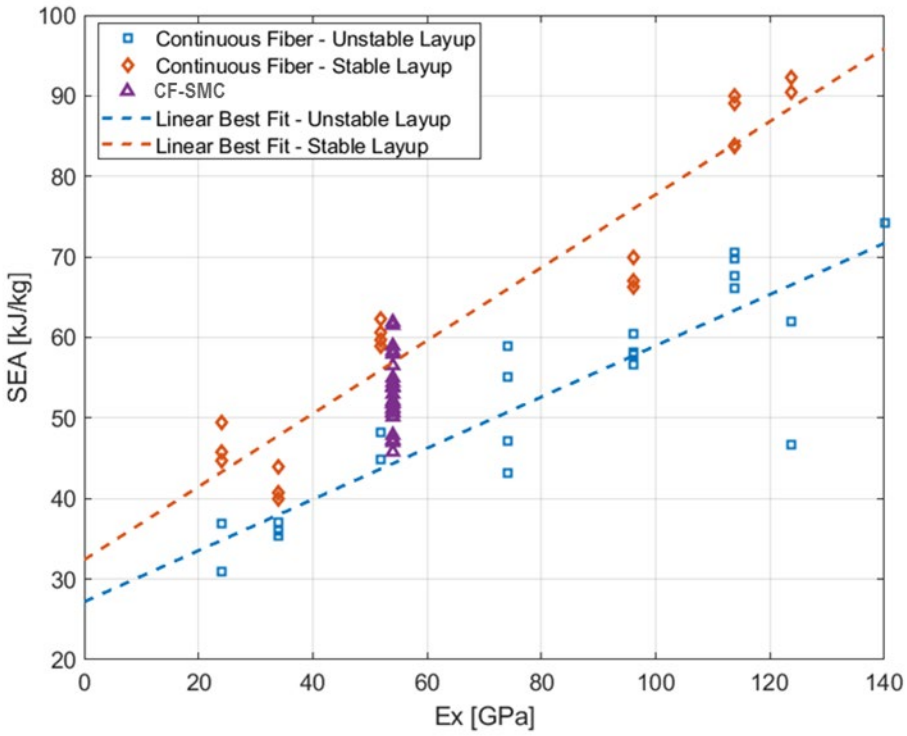

Figure 13. Specific energy absorption (SEA) of CF-SMC tubes is equivalent to that of continuous fiber tubes of equivalent laminate stiffness.

Crush Model Details and Setup

The CF-SMC tubes were recreated in LS Dyna with shell elements. The material model, *MAT_ENHANCED_COMPOSITE_DAMAGE (also known as MAT 54), was used in the models because it has the capability of capturing progressive failure within laminates. Laminate shell theory within LS Dyna was activated, and global damping as well as part stiffness damping were applied to the models. The unidirectional prepreg (UD) mechanical properties were implemented in the material model, and the individual platelet orientations were applied using in-plane orientations assignments on integration points in the shells. The bevel was modeled at the end of the tube by decreasing local element thickness to act as a failure initiator to ensure progressive failure within the model. A constant velocity rigid wall impacted the tube at a speed of 0.32 m/s. The load and displacement results were recorded at increments of 1e-8s to avoid aliasing of the signal. That is, the crush tubes in the simulation display a periodic failure that is dependent upon the velocity of the impacting wall and the mesh density. The simulation provides time histories of the load and displacement associated with these failures. If the output time step is too large for the simulation, aliasing can occur because of the periodic nature of the failure. In order to ensure we captured the full load displacement curve, a small output time step was used.

Simulation Results and Validation

Ten CF-SMC models were created for each of four separate platelet orientation distributions: $\mathbf{A}_{11} \in \{0.16, 0.3, 0.66, 0.8\}$. As the $\mathbf{A}_{11}$ component increased, the global stiffness of the tubes increased. This resulted in increasing stable crushing load values for the simulations, see Figure 14. However, for $\mathbf{A}_{11} \geq 0.8$, the simulation results are unstable. From unidirectional material experiments, we know that the presence of fibers aligned in the hoop direction specifically near the outer diameter is required for stable behavior. This behavior occurs because the stable time increment needs to be reduced. A parameter in LS Dyna defined as TSSFAC allows the user to adjust the stable time increment and reduce it further than the estimated value from LS Dyna. However, TSSFAC was kept constant in all of the models to ensure consistency, resulting in unstable results for several of the $\mathbf{A}_{11} = 0.8$ cases.

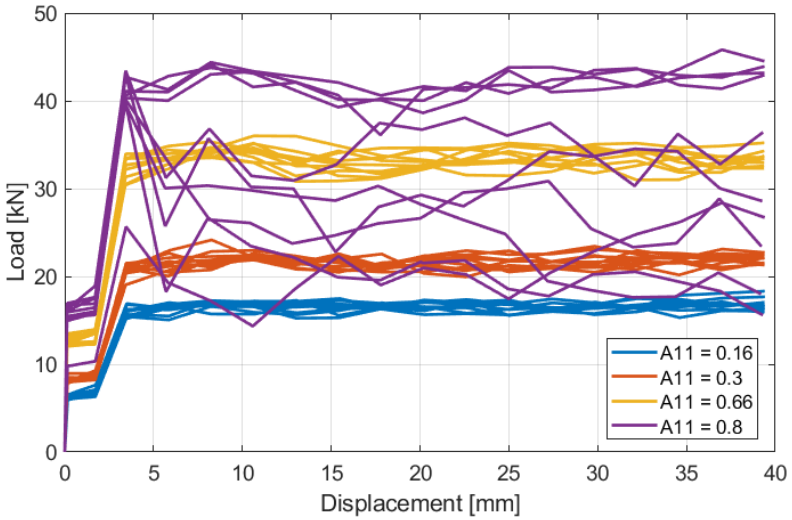

Figure 14. Increasing platelet alignment increases stable crush load and specific energy absorption.

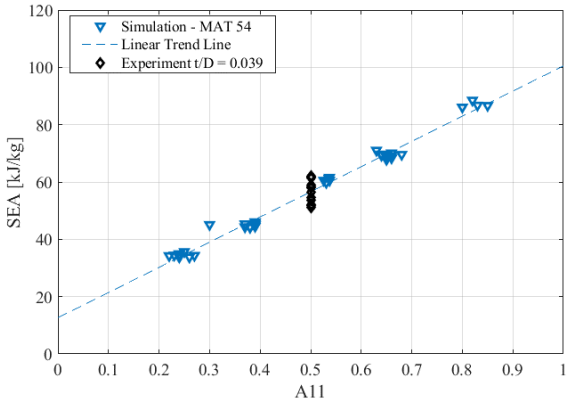

Figure 15. The specific energy absorption of CF-SMC tubes increases linearly with platelet alignment. The experiments agree reasonably well with the simulation predictions for the orientation state investigated.

When the SEA of the simulations are compared to those from experiment (Figure 15), it is clear that the simulations are capturing a reasonable trend with increasing alignment as the experimental results for crush tubes without flow alignment (nominally $\mathbf{A}_{11} = 0.5$), are nicely bounded between simulation results for slightly lower and higher alignment.

Lift Gate Flow and Stiffness Prediction

Manufacturing-informed performance predictions of the static stiffness were demonstrated on the liftgate inner. The stiffness of the liftgate inner was analyzed to reduce modeling complexity and investigate relative changes without modeling the entire liftgate assembly. The structural analysis was performed using layered shell elements. The stacking sequence of each shell element was created from the nearest orientations predicted in the molding simulation. The translation of processing information to the structural performance simulation requires mapping the orientation state from the flow simulation to the structural performance simulation (Figure 16). The example load case used to examine the static stiffness of the liftgate inner is representative of a closing load on the decklid (Figure 17).

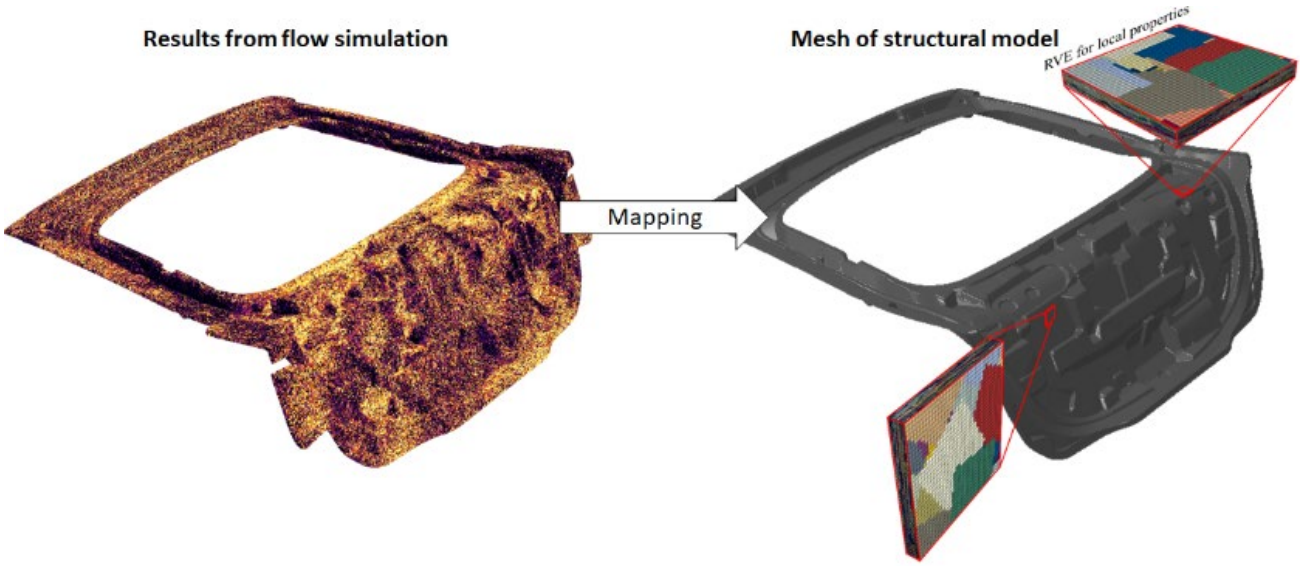

Figure 16. Prediction of manufacturing informed performance requires mapping the predicted spatial orientation state using a representative volume element from the molding simulation to the structural model.

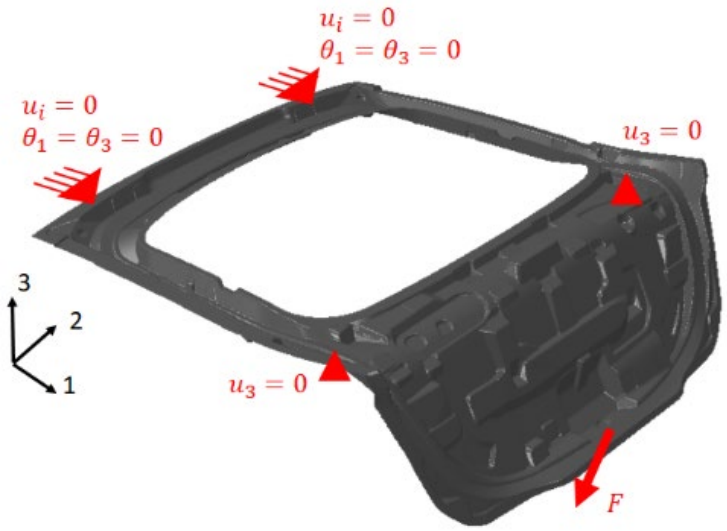

Figure 17. An example load case allows comparison of the static stiffness of a liftgate inner by varying material choice.

The results of the structural analysis of the liftgate inner are shown in Figure 18. A contour plot of the displacement is shown. The manufacturing-informed stress analysis of the CF-SMC composite liftgate inner was compared with an aluminum inner of equal mass (i.e., reduced thickness). The superior stiffness-to-weight ratio of the CF-SMC was realized in this example. Under equivalent loads, the maximum deflection of the CF-SMC inner was 1.8mm, while the aluminum inner of equal mass deflected 2.3mm, which indicates a ~20% increase in the apparent stiffness.

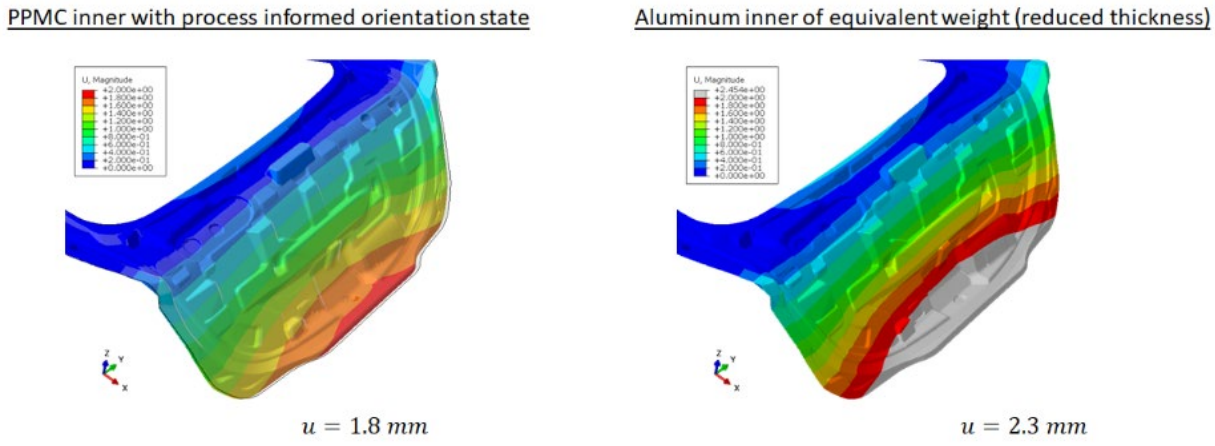

Figure 18. Comparison between the manufacturing-performed static stiffness of the CF-SMC inner and an aluminum inner of equivalent mass shows that the CF-SMC liftgate exhibits superior stiffness to the aluminum liftgate.

4.2.4 Conclusions from Simulation and Modeling Activities

An integrated series of models has been developed, demonstrated, and validated for the purpose of modeling the structural performance of Ford's automotive structures fabricated from Dow's CF-SMC material. Capturing the anisotropic flow behavior and transferring sufficient meso-scale information of CF-SMC material systems from molding simulation through to failure modeling is key to proper modeling of this unique material system. Providing a framework for design and analysis that realistically represents performance variability can help to move CF-SMCs from niche applications into the broader repertoire of composites engineers. This workflow has been successfully demonstrated to predict the compression molding filling of the Ford lift gate inner and the resulting structural performance, specifically the static stiffness.

In addition, the workflow has been validated through molding short shots, microscopy, and static coupon testing. Molding short shots confirmed the flow patterns predicted for both the transverse and axial charge patterns. The resulting platelet orientation spatial distributions were validated through microscopic examination of selected regions of the dome. Finally, strength and stiffness results from tensile coupons excised from specific regions of the dome geometry from both transverse and axial charges confirm the trends anticipated from the molding simulation, namely that flow alignment tends to increase the strength and stiffness of a local region. The strength and stiffness predicted for these specimens was in reasonable agreement with the experimentally observed strength and stiffness values.

There are a few limitations in current implementations of these tools that will be addressed with future development. It is computationally expensive to include enough SPH particles to represent all platelets present in the thru-thickness direction in a large geometry, such as the (future) target of an automotive liftgate. Instead, enough particles are included to approximate the actual number of platelet orientations present at any specific local volume. This simplification step is one of the reasons the flow simulation results are not directly mapped to create a virtual twin. Furthermore, correlation of model results for complex geometric features is not feasible as practical constraints require most test samples to be excised from flat, bar-like features on molded components. In addition, none of the performance models created for this paper contain resin-rich regions at platelet ends or platelet shearing that are observed in microscopy. For the crush tube shell models, there was no out-of-plane platelet orientation caused by platelet overlapping, and model instability was experienced above $\mathbf{A}_{11} = 0.8$. Addressing these limitations, including the mentioned meso-structural features in future models, and streamlining the workflow into a cohesive analysis suite are all planned as future work.

While there is more validation required to confirm the need for increased modeling detail in future iterations, the work presented here demonstrates the individual components that combine for a workflow for future CF-SMC design and analysis, including:

- Prediction of molded orientation state from various charge patterns with molding simulation via Abaqus SPH modeling with microscopy for validation.
- Mapping of local orientation states from molding simulation into solid and shell FE models.

- Prediction of mechanical performance for static stiffness and strength with orientation-informed virtual coupons, validated with mechanical testing.
- Prediction of crash energy absorption with LS-Dyna shell models validated with crush tube experiments.

The flow and crash models that were exercised allow the designer to understand and thereby engineer the material system and molding charge pattern and predict the resulting mechanical and crash performance of the part.

4.3 X-ray Tomography and Thermal Digital Image Correlation

The mechanical performance and failure mechanisms of chopped fiber, platelet SMC, or ROS (random orientated strand) systems has been investigated previously. Ferabolli et. al. looked at the effect of platelet geometry and corresponding failure mechanisms from length/thickness aspect ratios of 1.5 to12.5 for aerospace grade carbon fiber/epoxy systems [17]. After molding simple 10-by-10-in. flat plaques under minimal flow conditions, coupon samples were prepared for mechanical testing. It was found that failure progresses primarily in the resin system between and through chips with little or no fiber failure. Resin rich areas and voids were found not to be critical to failure, suggesting that platelet orientations and the complex load transfer interactions between platelets are the predominant failure locus. Minimal modulus dependence was found for platelet aspect ratio and the reduction of modulus from the quasi-isotropic continuous baseline was nominal compared to that for strength. Lastly, large improvements in modulus and strength (25% and 100%, respectively) were documented for increased part thicknesses from 0.08 in to 0.24 in. This highlights the stochastic, heterogeneous nature of these materials and the statistical dependency of their failure processes, such that increasing part thickness increased the probability of a reinforcing region of appropriate orientation to arrest an advancing crack. Selezneva et al. found similar patterns in performance relative to platelet aspect ratio as Feraboli using a PEEK/carbon fiber system, suggesting that failure modes between thermoplastic and thermoset are similar [18]. Since matrix failure dominates crack propagation, it was suggested that higher resistance to cracking in thermoplastic systems improves the mechanical performance by inhibiting crack propagation to ultimate failure.

A common challenge associated with heterogeneity of these materials is correctly assessing the internal micro and macro structures controlling mechanical performance. Thus, Feraboli has explored extensively using DIC (Digital Image Correlation) to assess total surface strains during mechanical deformation and ultrasonic C-scan to probe for internal defects potentially leading to failure, including non-platelet like structures (i.e., kinking), voids, and resin pockets [19, 20]. Such material defects were identifiable using ultrasonic approach, but did not correlate well with failure, as the primary failure mechanism is dominated by platelet orientation. Furthermore, this effect is also observed by the lack of notch sensitivity when stress risers were artificially introduced into the material. Thus, inherent stress concentrations from platelet orientations and interactions are the primary mechanism leading to failure [21]. Surface strain patterns from DIC were shown to be superior to either extensometers or strain gages as a way to accurately measure strain incorporating all structural spatial variations from structural heterogeneity.

It stands to reason, then, that platelet orientation, specifically in the local sense, is the dominant factor contributing to the failure of ROS composite systems. The ideal orientation state

sufficiently arranges platelets such that cracks must traverse long paths and change directions often to find the most energetically efficient route [18]. Consistent with this failure mechanism, it has been suggested that platelet length to thickness ratio is a controlling attribute for strength and modulus [22]. Thus, zones where similar layers of platelet orientations exist, are likely regions for crack propagation and ultimately sample failure. However, locating or predicting the regions of dominate orientation is a challenging problem, particularly in large parts like those being considered for transportation applications. Currently, fiber orientation measurement is confined to either destructive optical orientation techniques or semi-destructive X-ray tomography coupled with image processing. The former is severely limited by inspection window, such that the understanding of spatial variation of heterogeneous structures is not easily captured and would not be sufficient to provide information for part performance prediction. The latter requires expensive equipment and software, long data acquisition times, and is best suited for sample sizes where the largest dimension is approximately 1in. However, tomography does allow for the acquisition of sufficient data for performance prediction and thus, modeling performance from the platelet structure, specifically the spatial orientation states [23]. Thus, lacking in the current analysis tools and literature is a rapid, robust method for assessing part performance and quality for large domains and the development of orientation and part performance at the part scale opposed flat plaque or lab scale. Ultimately, if the appeal of manufacturability is to be harnessed over that of conventional UD, complex part shapes must be fabricated, which implies material flow will be necessary to fill mold cavities. Thus, the effect of material flow on mechanical performance and orientation is investigated.

4.3.1 Materials and Methods

Mechanical testing was performed on coupon specimens extracted from flat plaques and double domes. Flat plaques provide a source of test specimens for initial material property evaluation, while the double domes account for more complex molding filling and fiber reorientation. An example flat plaque and double dome is given in Figure 19. Flat plaque samples were prepared from four 250-by-250-mm charges stacked and placed symmetrically inside the mold as shown in Figure 20. Coupons for tensile, shear, and compression testing were extracted for testing. Compression and shear tests were performed according to ASTM D6641 and ASTM D5379 using the fixtures documented in Figure 20. Special care was taken during machining sample specimens to avoid fiber tear-out that could compromise sample integrity on the exposed and unsupported edges. Specifically, straight cuts were performed with a Tensilkut high speed diamond saw and edge cleanup was done with milling tools for composite applications. A common issue with these materials is the exposure of failure sites by machining in essence creating weakness that would not exist in the continuous part. As such, for the purposes of this report, the test data presented serves as a relative measure rather than absolute properties of the CF-SMC. All strains presented for shear, tensile and compression tests were obtained by Digital Image Correlation (DIC) from the part surface. For discontinuous systems, this has been documented as the optimal tool to study their performance due to the heterogeneous strain profiles developed during mechanical testing [20]. As has been shown previously for flat plaques, no orientation or regional dependence for performance has been found [17]. Thus, it is acknowledged that variation seen in testing metrics from flat plaques with samples extracted at different locations would be inherent in the material. The more complex structure of the double dome was produced from eight charges. Five locations were identified in Figure 20 where appropriate geometries existed for mechanical characterization; top, wall (x2), and flange (x2).

As demonstrated in Figure 21, the dome was labeled with four sides; A, B, C, and D, which is incorporated into the naming convention demonstrated in 22.

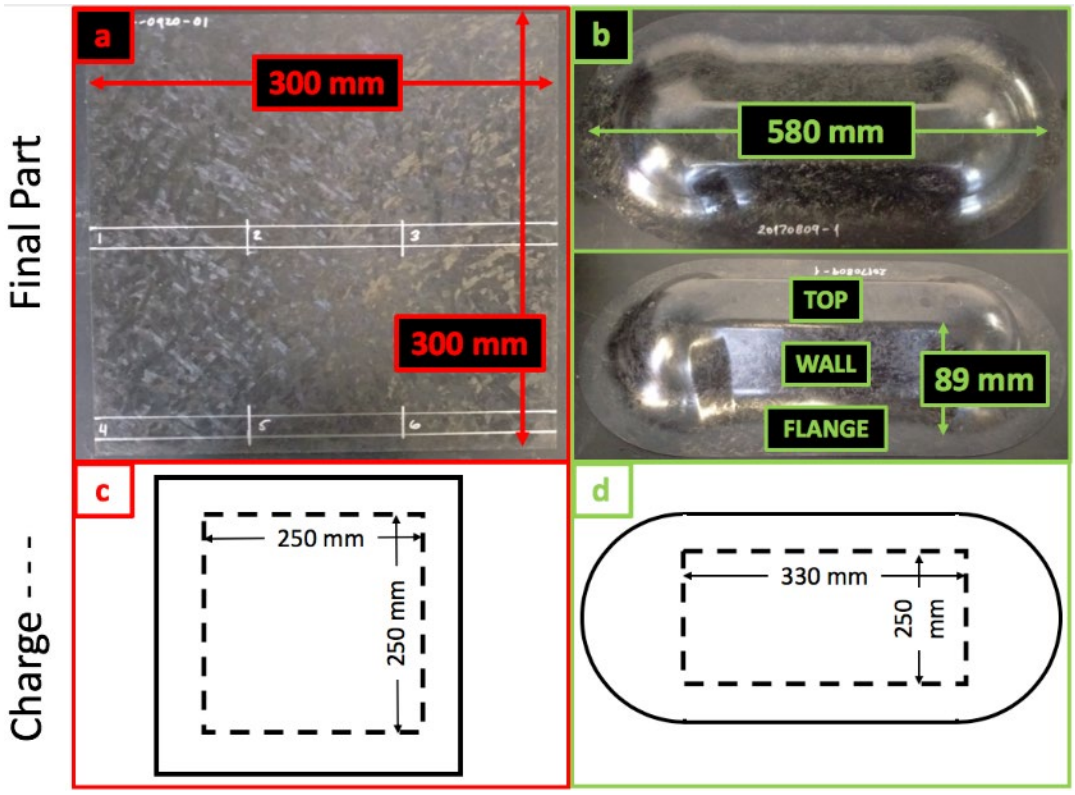

Figure 19. Example of a) flat plaque and b) double dome parts interrogated in this work.

.

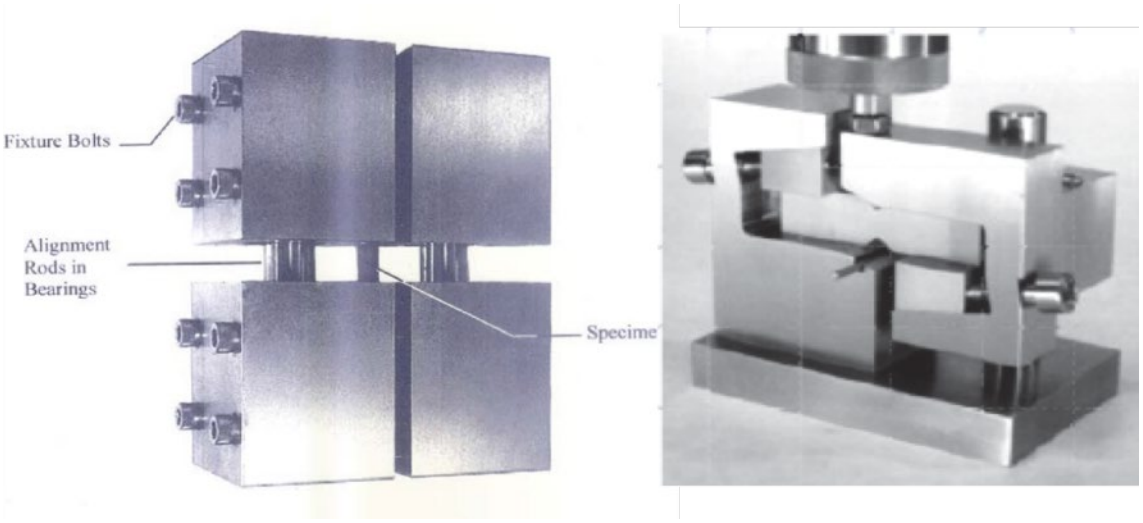

Figure 20. Standardized compression (ASTMD 6641) and shear (ASTM 5379) fixtures used in this work.

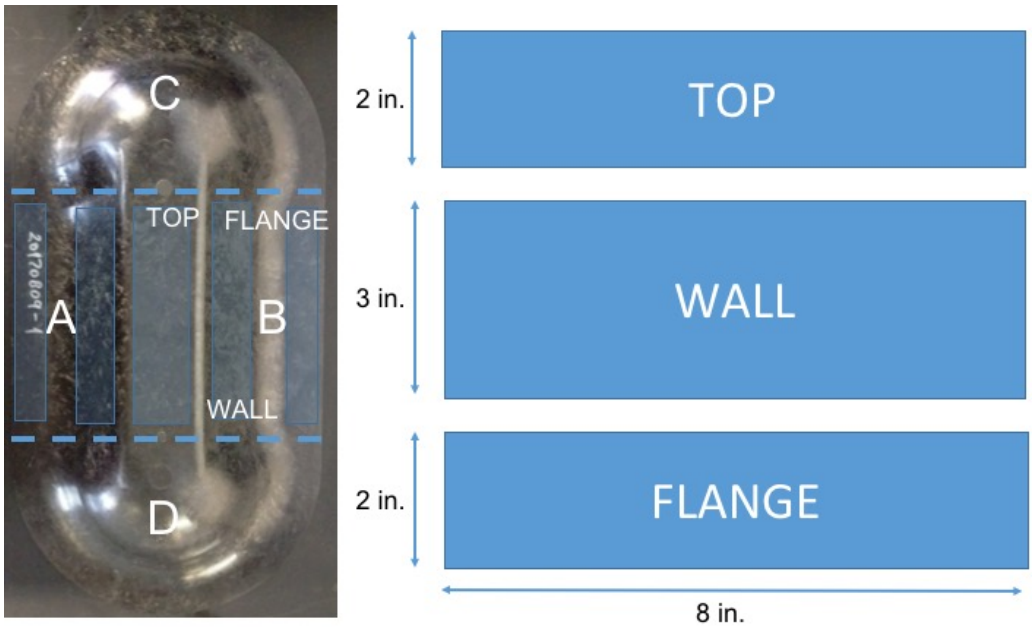

Figure 21. Example naming convention of large area coupons for standardized testing sample extractions. Due to molding and flow conditions during sample manufacturing, it is expected that large property variation will exist between these regions.

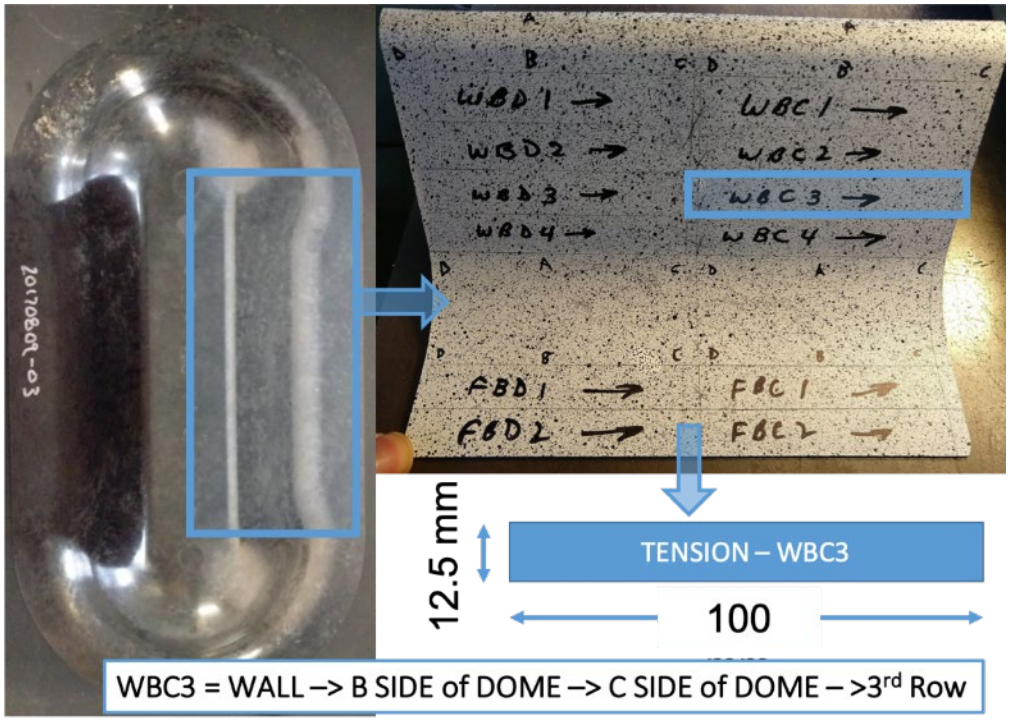

Figure 22. Description of naming convention used for extracted double dome coupons.

The work presented herein is set to advance the understanding of these materials in the following areas;

1. The comparison of performance for DA42 carbon fiber/epoxy ROS system molded in flat plaques and double dome (i.e., part scale).
2. The fiber orientations by Xray tomography of molded flat plaques and double dome (i.e., part scale).
3. The development of a novel tool, TDIC (Thermal Digital Image Correlation), for assessing part performance rapidly over large domains.
4. Using TDIC to quantify the residual stresses developed during molding.

4.3.2 Results and Discussion

4.3.2.1 Tensile Performance

The tensile behavior of carbon fiber/epoxy ROS composite was determined for 300--by-300-mm flat plaque, compression molded geometries shown in Figure 19. Tabs with lengths of 50 mm were glued on the 25.4mm-wide and 254.0-mm-long specimen for gripping, such that the gage region was allowed to be 25.4-by-152.4mm. Although tabbing is optional according to ASTM D3039, it provided protection should the failure stress be exceptional [24]. The configuration of the extracted flat plaque coupons is demonstrated in Figure 23. It is important to note that this geometry and configuration has been tested by multiple labs (specifically IACMI partners at Dow and Purdue) and will serve as the basis of comparison and establish performance benchmarks going forward for this material system. Following the standardized tensile testing, the stress/strain relationships are plotted in Figure24. The average modulus and failure stress were found to be 42.0 GPa and 320 MPa, respectively. The strain map in Figure 24 from test 4 demonstrates the significant strain variations throughout the sample typical of these materials, suggesting that strain concentrations are common as a result of the heterogeneous platelet structure. It was found that strain concentrations, which developed at low stress magnitudes at the sample edges and propagated through the sample with increasing stress amplitude, ultimately led to sample failure. This suggests that the material morphology that leads to failure is localized platelet orientation transverse to the loading axis, which has also been observed by other investigators of similar material systems.

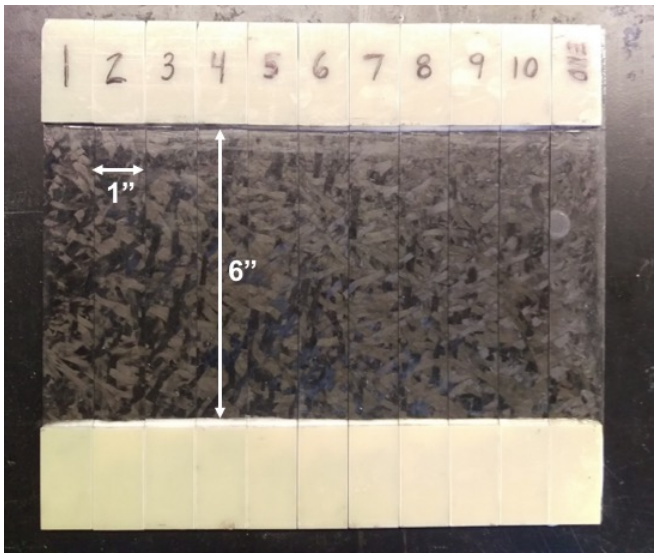

Figure 23. Example of 300-by-300mm molded flat plaque with tensile specimens cut 25.4-by-254.0mm and tabbed for tensile testing.

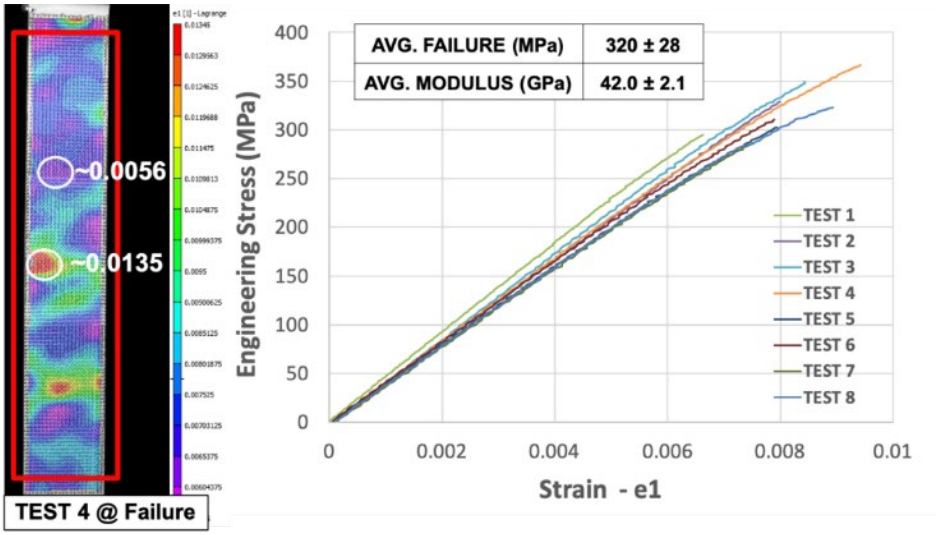

Figure 24. (Right) Stress/strain behavior of material in flat plaque mold prepared with 150mm-by-25mm gage region. (Left) A typical surface strain pattern near failure, demonstrating significant strain concentration as a result of random regions of high platelet mis-orientation.

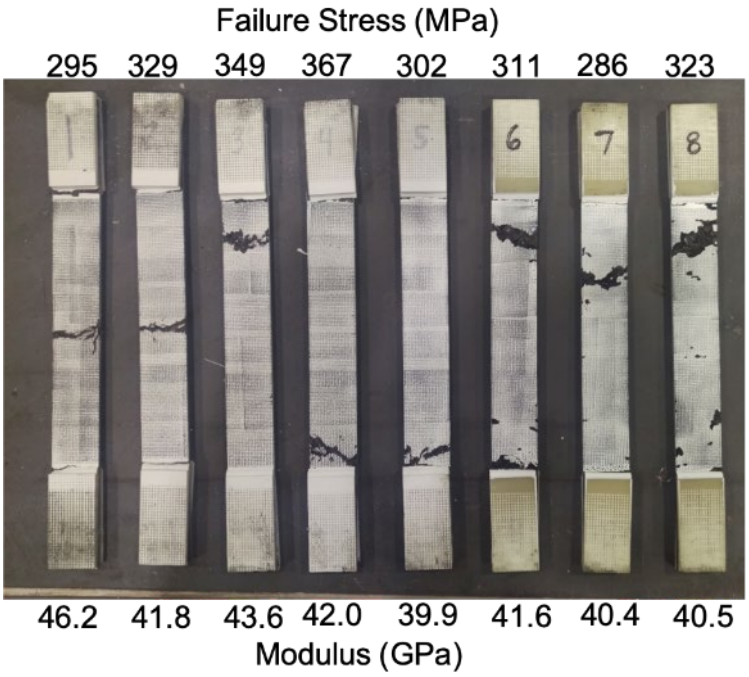

Figure 25. Failure of tensile specimens (Figures 23, 24), demonstrating acceptable breaks within the gage region.

To observe the manufacturing effect on material performance, parts were molded into a geometry exemplary of an end application, specifically the double dome mold. The double dome mold presents challenging geometrical features which tests the formability in ways the simple flat plaque does not. Thus, new microstructures as a result of flow could dictate new performance specifications. Ultimately, the goal was to simultaneously document both material performance coupled with internal microstructure via X-Ray tomography. Due to the resolution necessary to discern internal structure, a reduction in sample size made efficient X-Ray tomography more feasible. Thus, samples were reduced in size from the ASTM suggested 150x25mm to 50x12.5mm gage region. Figure 26 shows sample extraction of the reduced sized coupons from both the flat plaque and the double dome. The 4 flat plaque samples extracted from plate LMG072117-30 (Figure 26) in the 100x12.5mm geometry gave an average failure stress of 301 MPa and young's modulus of 39.0 GPa, demonstrating a small reduction in performance, 6% in failure stress, due to small sample size effect. Hence, the expected size effect was minimal. A good comparison of the knock-down of mechanical performance observed in the samples extracted from the wall portion of the double dome is shown in Figure 27. Here, clearly both dome tensile coupons demonstrated decreased modulus and decreased failure stress, despite using identical charge material. This suggests the orientation of the wall section was more transverse to the axis of the extracted coupons, resulting in the reduced stiffness, and that due to the flow of the material, the ability of the material to resist crack propagation and ultimately failure strength was also reduced.

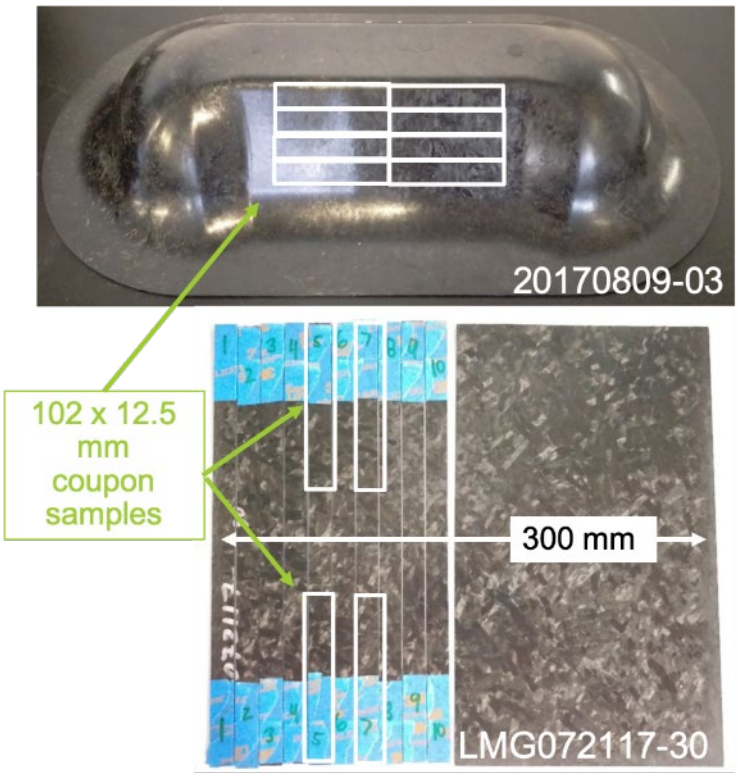

Figure 26. Example of extraction of 100-by-12.5-mm (50-by-12.5-mm gage) tensile sample from double dome (top) and flat plaque (bottom) molded part.

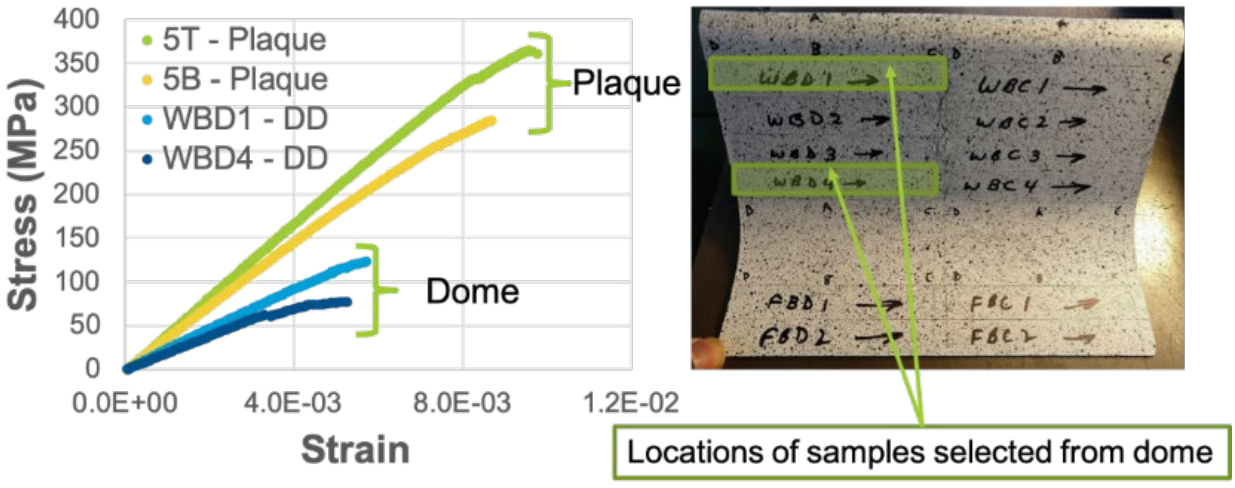

Figure 27. Comparison of tensile stress/strain behavior from different locations.

Figure 27 documents a clear reduction in mechanical performance switching from the flat plaque to the double dome (all but for an isolated location). The reduction in performance suggests the manufacturing process affects the microstructure. This creates a location dependency for performance that varies throughout the part. Figure 28 describes the general behavior of spatial performance observed from the three dome regions delineated in Figure 19. The samples extracted from these regions showed that the modulus followed this order: Flange > Plaque > Top > Wall, while the order for failure stress was Plaque > Flange > Top > Wall. Hence, the wall was the weakest and least stiff of all regions tested. An example fracture surface from the coupon and side plane is given in Figure 28 for both the wall and plaque samples, which demonstrates that the wall cleaved almost in a single line transverse to the axis of the coupon. This contrasts starkly to the jagged like fracture of the flat plaque, which suggests greater energy absorption and therefore a larger failure strength. This is attributed to reorientation of the platelets during fabrication, resulting in a predominance of fibers that are perpendicular to the coupon tensile axis.

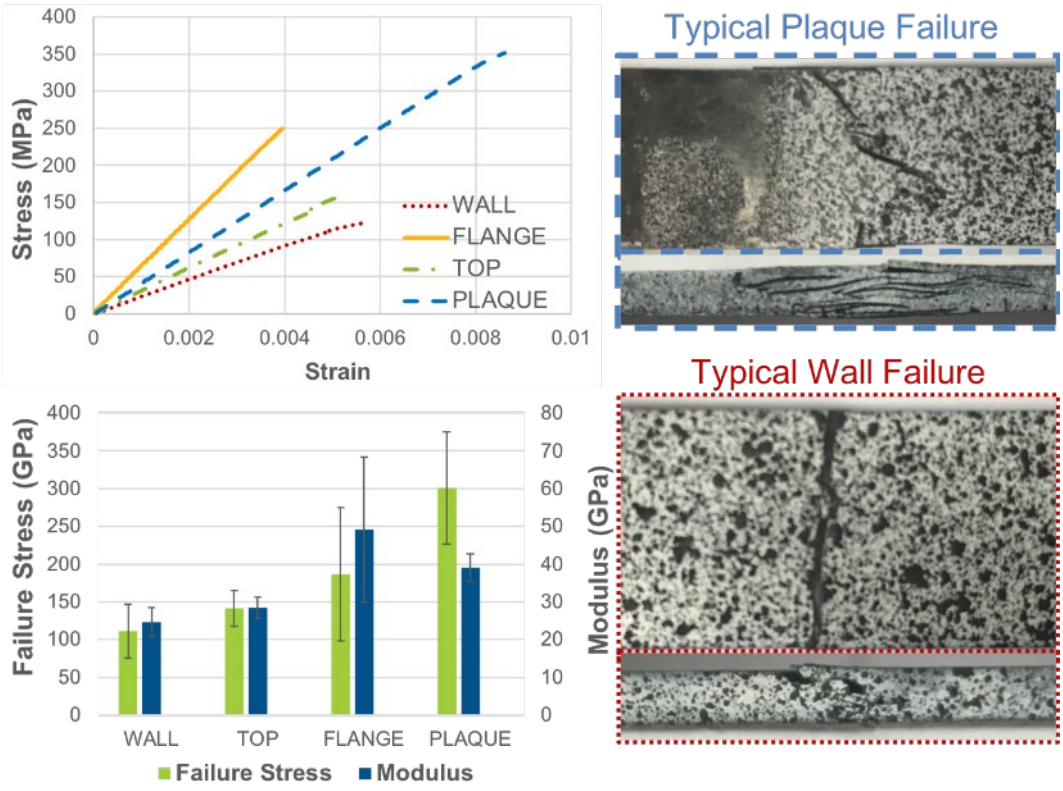

Figure 28. Stress/strain response of tensile coupons extracted from molded flat plaques and double domes, demonstrating typical, regional mechanical performance observed for these parts.

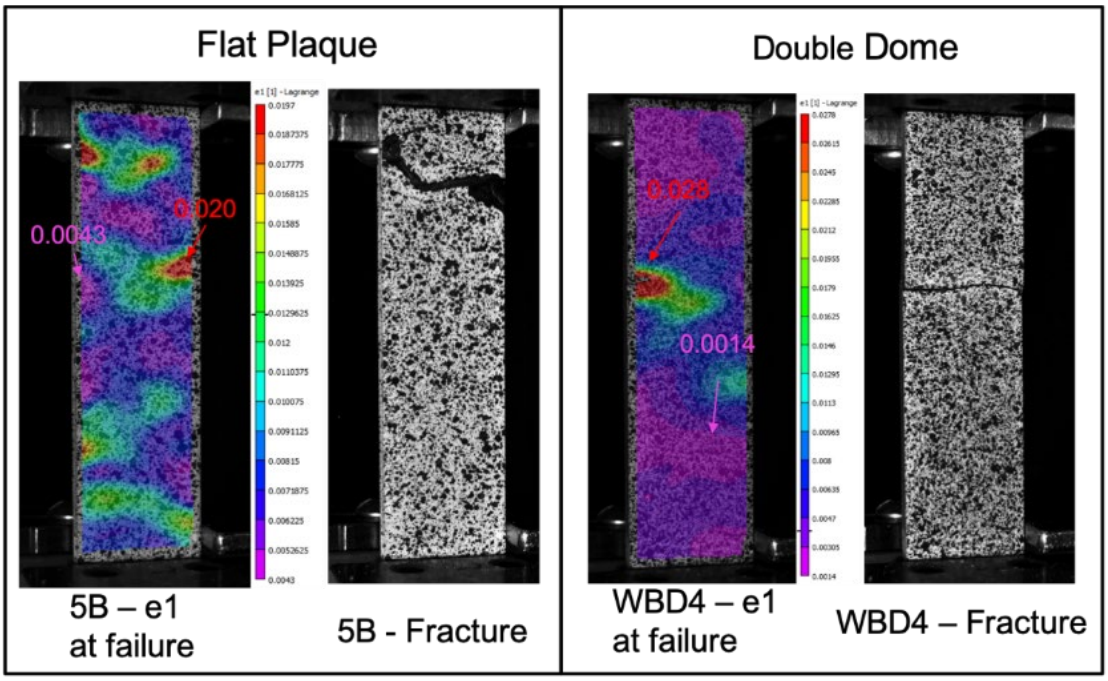

Figure 29. DIC strain maps of test samples.

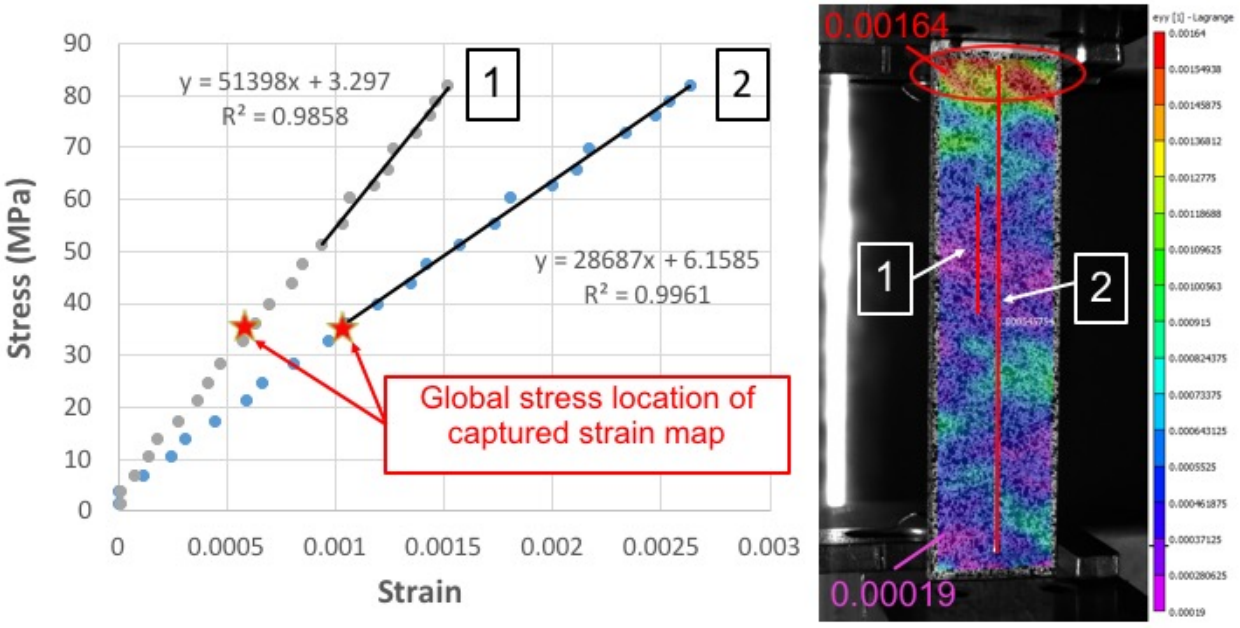

Figure 30. Stress/strain behavior of a tensile coupon from the flange section (sample FBD1) of the double dome with the strain map at the starred stress position. A significant strain concentration where the sample ultimately failed is observed at the top.

It was put forth that these regions of significant fiber reorientation result in a reduction of natural crack arrest sites, which effectively lowers the local strength. These regions are observable in the DIC strain maps shown in Figure 29.

Comparing the DIC strain map when approaching part failure, the variation of spatial strains from flat plaque to double dome part is shown to decrease in frequency. This suggests the agglomeration of like fiber orientations. Ultimately, this allows cracks to propagate unmitigated. Another example of strain variation from DIC strain mapping is observed in Figure 30, where at relatively low stress magnitudes, significant large strain concentrations are already developed. The two stress/strain relationships in Figure 30 come from the digital extensometers defined in the coupon image, showing that modulus can nearly double, 51.4 against 28.7 GPa, by changing the definition of the extensometer. This highlights the performance impact of localized changes fiber orientation and volume fraction. That is, the smaller the gage length, the greater the variation in mechanical properties. The region of strain concentration at the top did predict the ultimate failure location of this part, even at low stress magnitude. Additionally, because the spatial strain maps correlate with underlying microstructure, DIC is an indispensable tool for assessing the performance to microstructure relationship of these discontinuous materials.

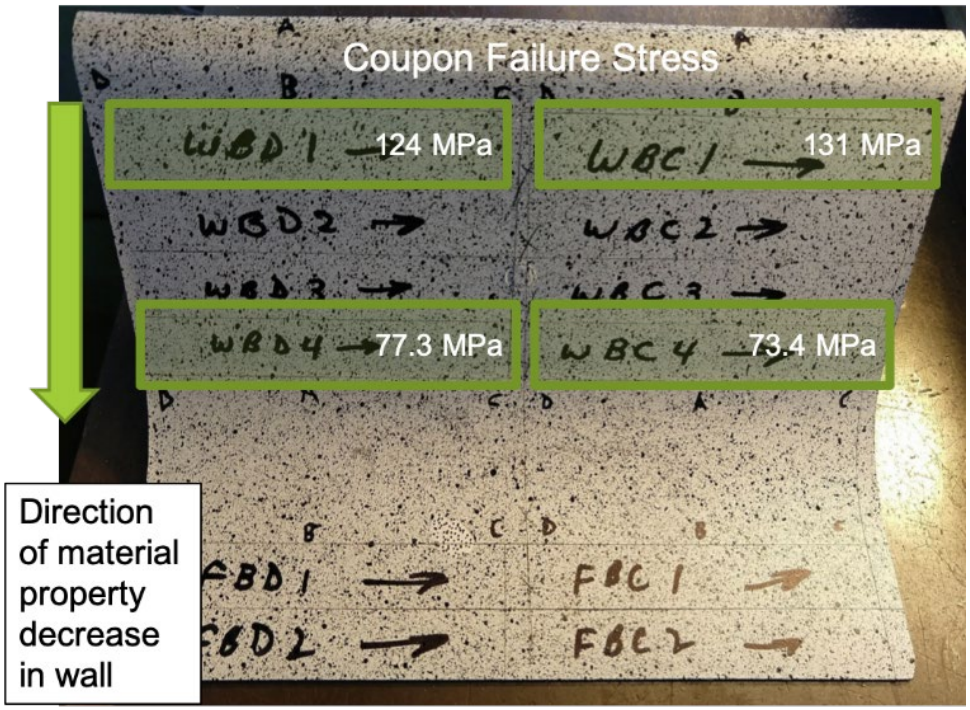

Figure 31. Part view of tensile performance relative to coupon extraction location. For the wall specimen it was observed that failure stress dropped further from the center of the double dome.

Figure 31 documents the failure stress spatially of tensile coupons extracted from the wall portion of the double dome. Because the charge pattern was centered in the mold (Figure 19), the material flowed outward from the center toward the flange regions of part. Thus, material located further out from the center of the double dome is susceptible to more flow-based conditioning of its final microstructure. That is, greater fiber alignment was observed resulting in more fibers perpendicular to the axis of the test coupons. Thus, a reduction in failure stress was observed for

coupons when moving away from the center double dome toward the wall section.

4.3.2.2 Shear Behavior

Shear samples extracted from flat plaque and double dome parts were tested using the V-notch beam method from ASTM D5379. Stress/strain relationships are plotted in Figure 32 for both double dome and flat plaque parts. In contrast to tensile performance, little difference was observed between different regions of extracted specimens within the double dome (i.e., top, wall, or flange), but a small reduction in performance is documented in Figure 32 between the flat plaque and double dome, albeit much smaller than that noticed for tensile performance. Thus it follows that orientation plays a smaller role in the failure of these specimens, as the tensile dome specimens were found to match to orientation trends from fabrication. It should also be noted that this test may not be appropriately suited for discontinuous materials like these, since it was rare that fractures or peak strains actually occurred where designed. This issue has been previously observed by Feraboli, who observed general notch insensitivities for similar material systems and found that stress concentrations arising from the heterogeneous microstructure dominate specimen failure [21]. Typical shear failures shown in Figure 33 for multiple parts demonstrates the ambiguous nature of specimen fracture characterized by the inherent microstructure. Most importantly, Selezneva has shown that shear performance of ROS composites is the nearest to the quasi-isotropic continuous composite benchmark. This suggests that these materials are most suited to these corresponding applications.

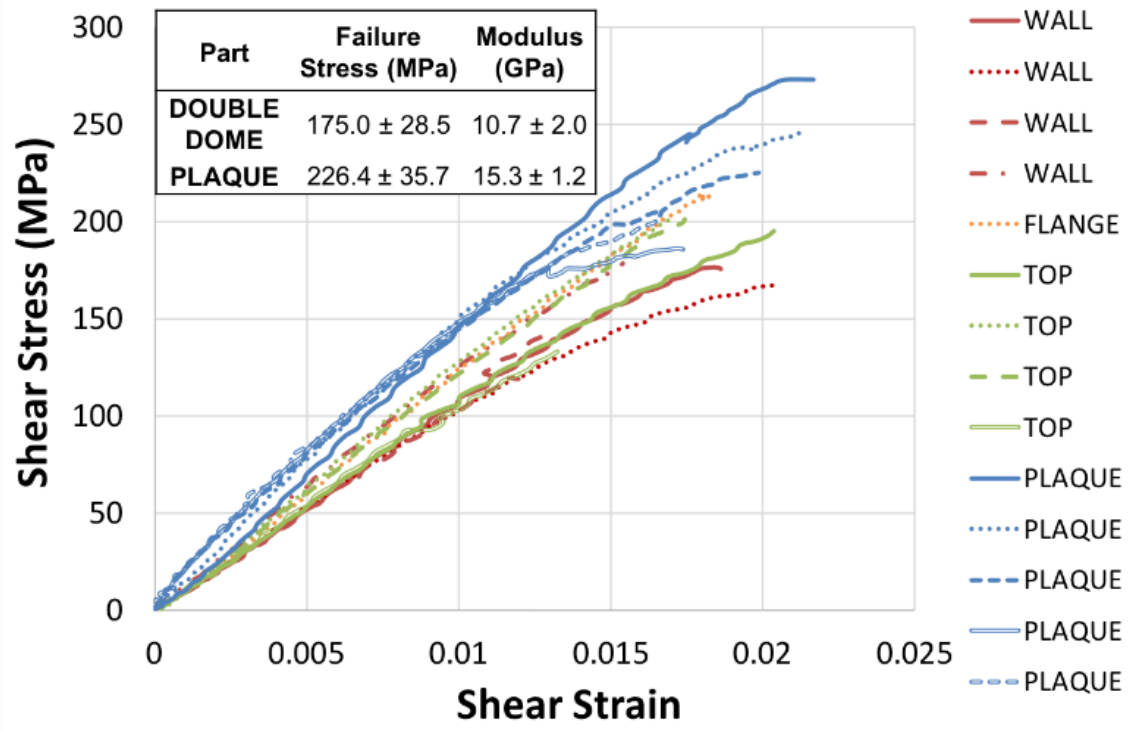

Figure 32. Shear stress/strain behavior for all samples tested in this work, demonstrating a small drop in mechanical performance from the flat plaque to double dome parts and no clear difference for parts extracted regionally (top, wall, or flange) from within the double dome.

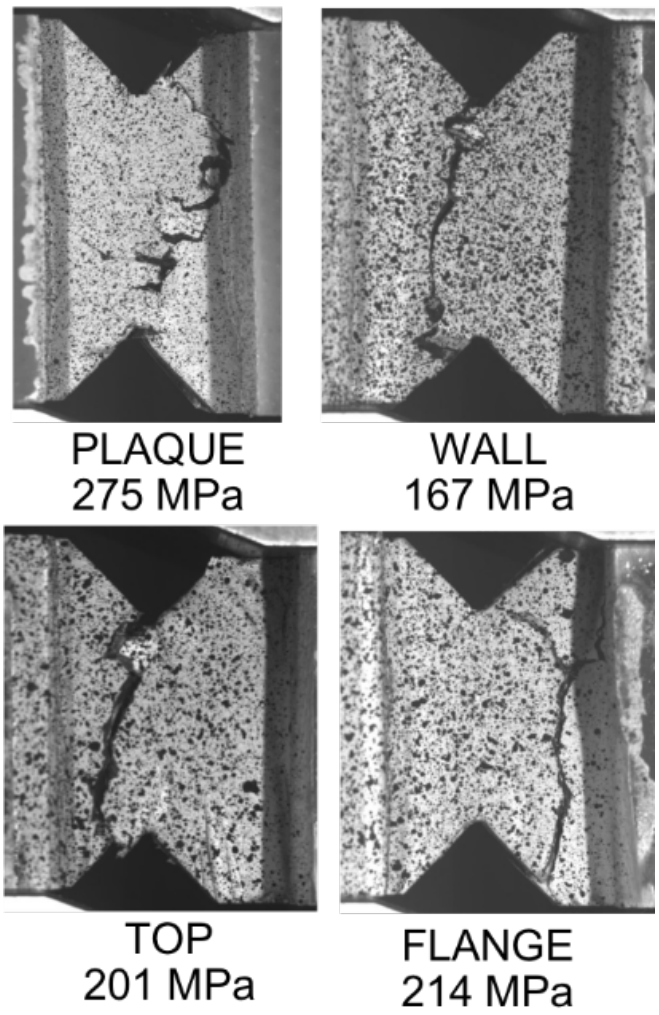

Figure 33. Examples of typical shear failures demonstrating sample fracture rarely occurs along the path of peak shear stress.

4.3.2.3 Compression Testing

Compressive properties were studied using the combined loading approach defined by ASTM D6641. The baseline of plaque performance is given in Figure 34, which shows a consistent failure with an average of 350.2 MPa, similar in magnitude to the tensile failure stress. However, the compressive stress/strain relationship is nonlinear up to failure, suggesting irreversible damage begins even at low stress magnitudes. Figure 35 compares flat plaque and double dome compressive performance with example stress/strain curves for each extracted sample location. Although nonlinear, the stress/strain relationships mimic the pattern observed from tensile behavior, indicating stiffness is dominated by internal fiber orientation. Due to the small material volumes used for this test, sufficient evidence for a compressive stress performance comparison within the double dome given the highly heterogeneous and random microstructures with each sample extraction is difficult. The observed post-failure specimen images in Figure 35 document clearly that large, unfragmented cracks develop for the lower failure stresses, while the higher failure stress flange and plaque regions demonstrate more crack surfaces created. In general, the average plaque failure was greater than that from the double dome samples, indicating the

material processing reduces the ability of the material to redirect propagating cracks as was also shown for tensile specimens.

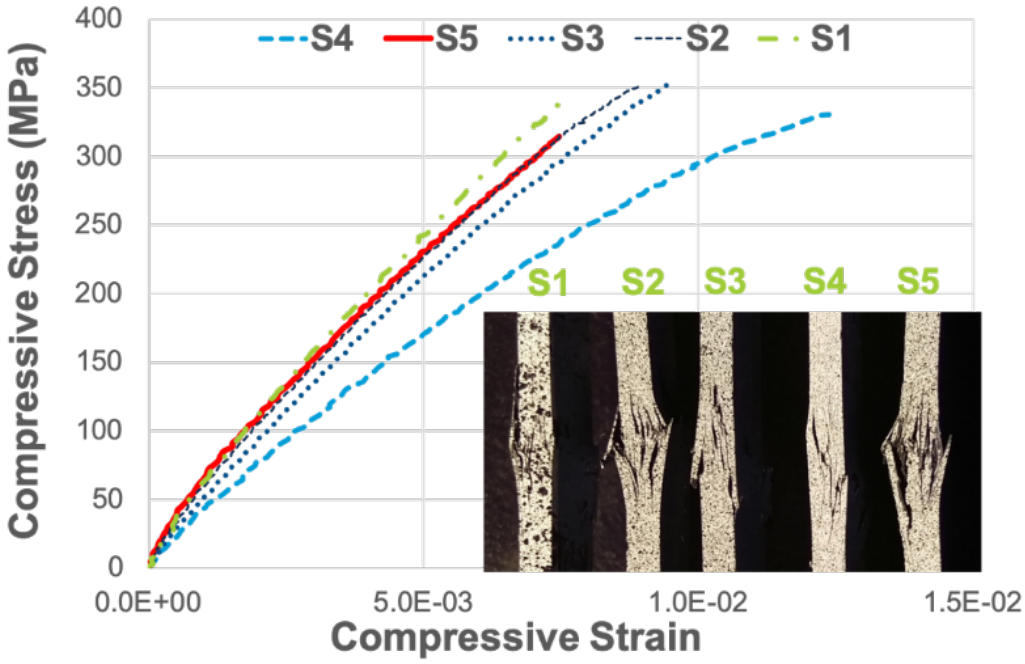

Figure 34. Compression stress/strain response for coupons extracted from flat plaques.

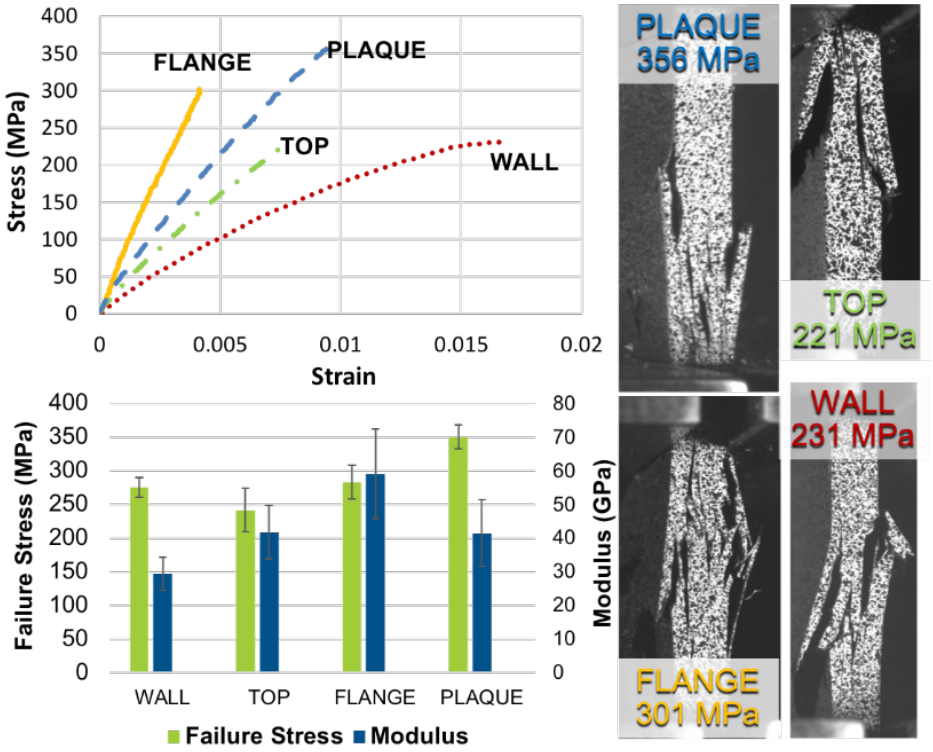

Figure 35. Stress/strain response of compression coupons extracted from molded flat plaques and double domes, demonstrating typical, regional mechanical performance observed for these arts. A similar pattern in modulus was observed as that seen in the tensile coupons, with the greates modulus in the flange and smallest in the wall.

4.3.2.4 X-ray Tomography

To determine the internal orientation of these platelet-based SMC carbon composites, XCT scans were captured over ~25 mm sample windows at 15-micron voxel resolution. To cover the entire 50-mm gage region of the small tensile coupons tested here, two scans were stitched together. The typical fiber size is on the order of ~8 microns and, thus, a single voxel is approximately 2x larger than the 'average' fiber diameter. Hence, the tomographic reconstructions are dependent on depicting the spatial arrangements of the macroscopic platelet structure and are not dependent on mapping single fiber orientations [22]. This approach provides desired information of microstructure at suitable length scales and represents statically significant region of volume for the related analysis. Typical tomographic reconstruction is demonstrated in Figure 36, which is in essence a 3D spatial map of X-ray attenuations. Clearly, the platelet structure can be resolved visually, which indicates that further computation for orientation states will be possible. Hence, the acquired tomographic data is then processed in the Fiber Composite Analysis Module in VGStudio, which uses a gradient analysis approach to determine the orientation tensor. A 3D mesh of size 0.7-by-0.7-by-0.1 mm is created over the entire part on which an average orientation tensor is calculated for each mesh element. The 0.1 mm element depth produced approximately 20 spatial orientation maps through the ~2.0 mm thickness and allowed for the capture of orientation changes in this dimension. An example mesh and corresponding fiber orientation map for a single slice is given in Figure 36. It also is easy to discern the correspondence of fiber orientation from the color-coded orientation map and the tomographic

reconstruction, giving firsthand confidence that the orientation algorithm is working acceptably.

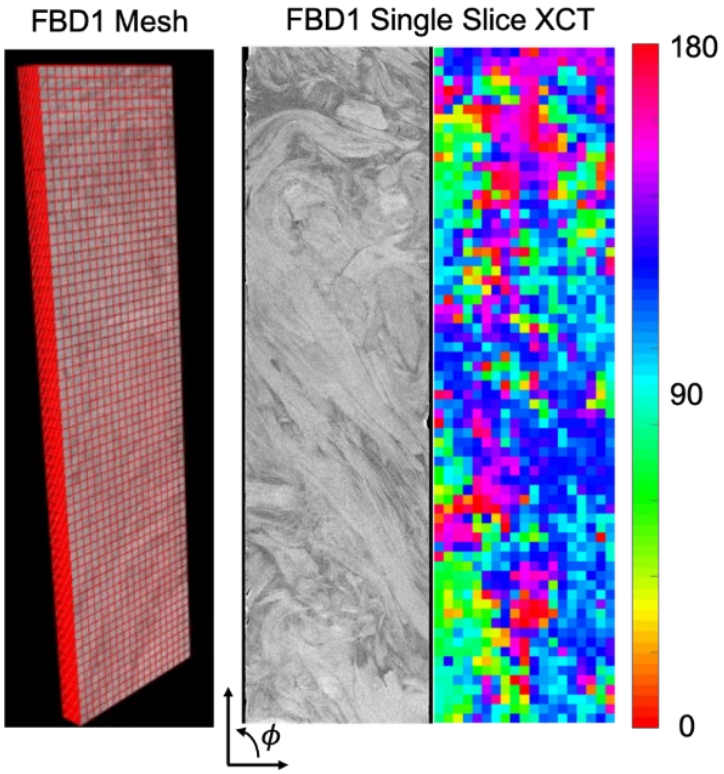

Figure 36. An example work flow and result of tomography acquisition and processing. Tomographic reconstructions are meshed (0.7-x-0.7-x-0.1 mm) and then analyzed for orientation. The color-coded fiber orientation is projected to the coupon plane, which gives excellent insight into part performance.

A useful way to quickly understand the entirety of the sample's orientation is to construct a histogram of all projected fiber orientations to the coupon plane for all mesh elements in a given tomography. The fiber direction corresponds to the Eigen vector associated with the maximum Eigen value of the orientation tensor [25]. Since these materials are essentially laminates, the projected orientation is a reasonable approximation and tends to correlate well with the mechanical performance. Histograms summarizing the orientation states from the flat plaque and two double dome locations (WBC2 and FBD1) are given in Figure 37. Here is an excellent demonstration of the effect of material flow during part formation. Notice the histogram for the flat plaque coupon is flat, indicating that the coupon plane orientation states are randomly distributed, but the double dome histograms have significant peaks associated with specific in-plane directions. These peaks indicate that fiber orientation throughout the volume of these coupons is preferred. For the wall specimen, WBC2, preferential orientations toward 0 (or 180) degrees were found, which would be transverse to the axis of the coupon. This correlates well with the reduced mechanical performance observed (Figure 28) for extracted tensile coupons from the wall region. Similarly, the preferred orientation in the flange region resulted in coupons with higher tensile modulus. Due to the boundary condition along the mold edge, the flange

coupons tended to have fiber orientations more aligned to their tensile axes, as material flowed parallel to edge of the mold.

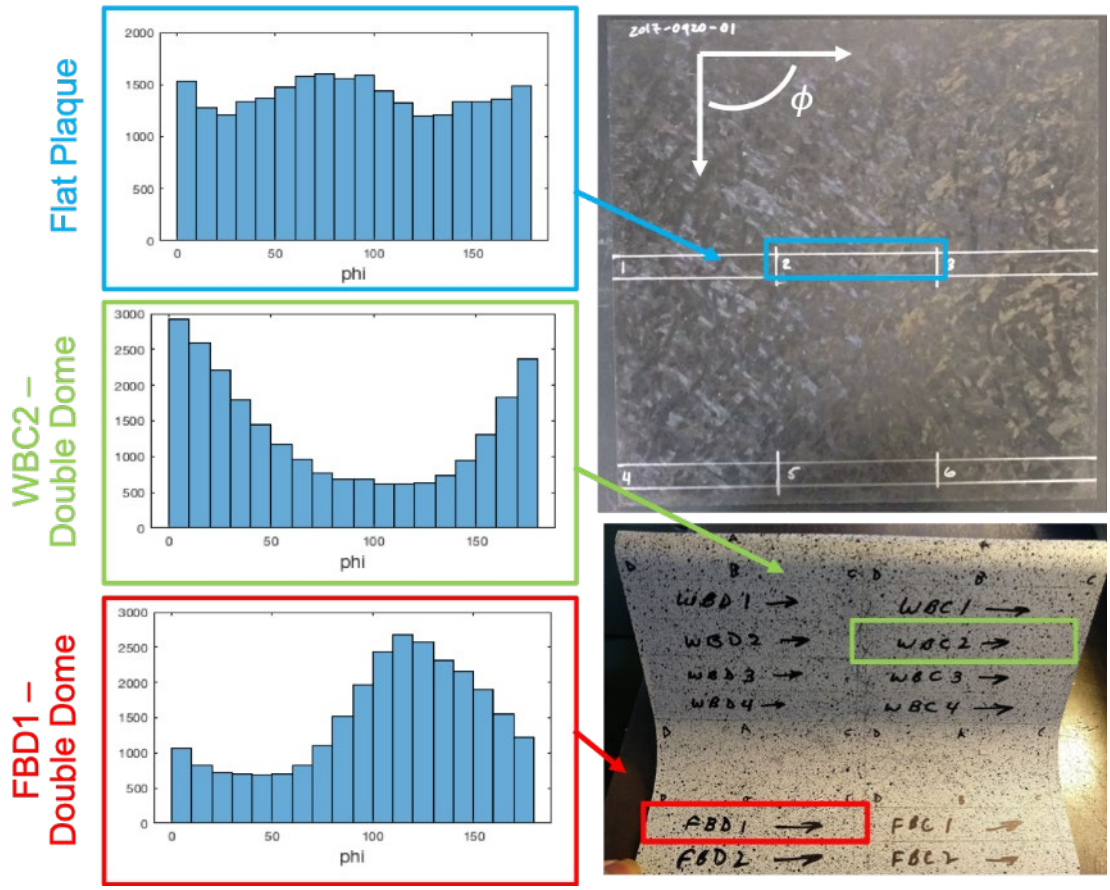

Figure 37. Histograms of all mesh elements from the analyzed tomography data for flat plaque and double dome extracted coupons, demonstrating the development of preferred fiber orientation during compression molding in the double dome due to material flow.

4.2.2.5 Thermal Digital Image Correlation

Thermal Digital Image Correlation (TDIC) provides a rapid way to spatially interrogate the performance of parts fabricated from discontinuous fiber. It is postulated that for relatively thin parts a dominant fiber orientation can be extracted by first observing the local thermal strain anisotropy and then comparing the magnitude of anisotropic thermal expansion to that of random and highly orientated composites. As the magnitude of the anisotropic thermal expansion approaches unidirectional, the higher the preferred local orientation in the part. On the contrary, an insignificant amount of anisotropic thermal expansion would be expected in more randomly oriented samples. Figure 38 demonstrates application of the TDIC technique on a 2-x-2-in. unidirectional, pultruded carbon fiber composite. The part was imaged at room temperature then heated in an oven at 84°C. to isothermal conditions. Strain measurements using DIC were made on the thermally expanded part. Figure 38 demonstrates the spatial mapping of the first and second principle strains for the UD composite. Despite variation in strain amplitudes spatially, a uniform fiber orientation is shown that aligns well with the known pultrusion direction. This confirms that the large contrast between fiber axis and matrix thermal expansion can be detected quite readily and hence, by knowing the anisotropic local thermal expansion states an assessment of the fiber direction in the composite can be determined.

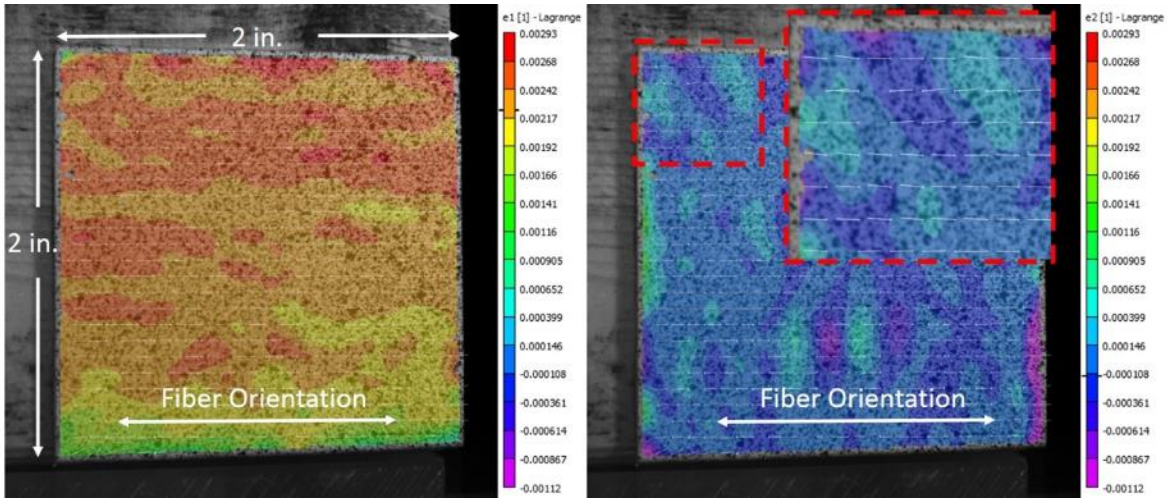

Figure 38. The thermal expansion at 90°C of a pultruded UD plate with the fiber orientation designated. The plotted vectors represent the orientation of the minor principle strain.

A map of thermal expansion over a component can be tracked using digital image correlation (DIC). Deviation from an isotropic thermal expansion behavior ($\epsilon_1 = \epsilon_2$) suggests anisotropic fiber orientation is present. This behavior becomes more evident as the sample is heated further beyond room temperature conditions. This can be observed in Figure 39, where the spatially extracted thermal strain states were plotted on principle axes. The strain points in Figure 39 move along the horizontal axis as temperature increases. This is due to the thermal expansion of the epoxy dominating the response. Because the coefficient of thermal expansion (CTE) of carbon fiber is much smaller along its axis than that of epoxy, the direction of the fiber will always be the orientation of the minor principle strain when fiber alignment in the composite exists [26]. A threshold criterion can then be applied to reliably discern any anisotropic fiber orientation in sample under test. Graphically, this threshold can be mathematically defined as the

geometric distance of the strain points from the line y=x (or isotropic case) shown in Figure 39. For example, the UD sample, temperatures exceeding 65C show significant departure from the line x=y. This would indicate significant fiber alignment in these regions of the part. For more complex parts with many orientations present, this parameter will be used to assess the reliability of the methodology. To improve confidence in the TDIC analysis conclusions, 90°C was selected for sample observations as this was deemed sufficient to observe any anisotropic thermal expansion using DIC without inducing irreversible sample damage.

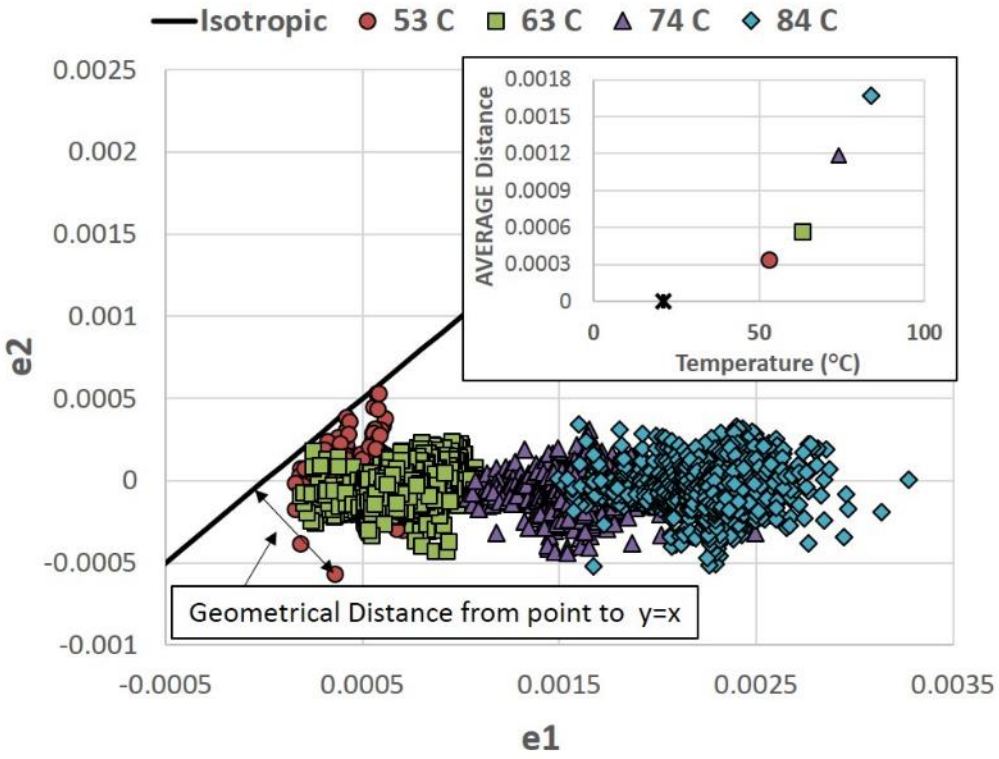

Figure 39. The distribution of spatial principle strain states as determined by DIC for the UD plate in Figure 38, demonstrating the development of anisotropic thermal expansion with increasing temperature, which is a result of the highly anisotropic CTE from highly oriented fibers. This suggests in temperature ranges well below TG of the matrix material, ansiotropic mechanical behavior is easly captured by DIC

To demonstrate the potential application of using TDIC to study composite mechanical performance, several composite parts with different manufacturing techniques and microstructures were imaged at 22°C and 90°C. Figure 40 compares the "variation of spatial thermal expansion states" at 90°C for a chopped, wet-laid PPS SMC, a unidirectional, pultruded carbon, and epoxy part, and the compression molded chopped fiber SMC system being studied here from both the flat plaque and double dome parts. Despite different resin systems, the negative thermal expansion of carbon fiber provides the necessary contrasting feature used to obtain fiber orientation via the TDIC approach. While the pultruded UD represents the most anisotropic, the wet laid mat represents the most isotropic part, as seen by the congregation of their data points furthest and nearest to isotropic line, respectively. The platelet SMCs lie between these extremes, with the part scale double dome showing more anisotropic expansion.

The double dome part experienced more material flow compared to the flat plaque and thus, developed regions of higher orientation. Figure 41 used the geometric distance criteria to extract the intensity of anisotropic expansion from Figure 40 as a histogram. Each sample in Figure 41 correlates ideally with the expected relationship for anisotropic thermal expansion and the expected magnitude of anisotropic behavior. Furthermore, Figure 41 suggests that spatial thermal expansion states can vary significantly for the same material depending on the processing conditions, and similarly, the variation of mechanical performance observed is confirmed with this testing approach.

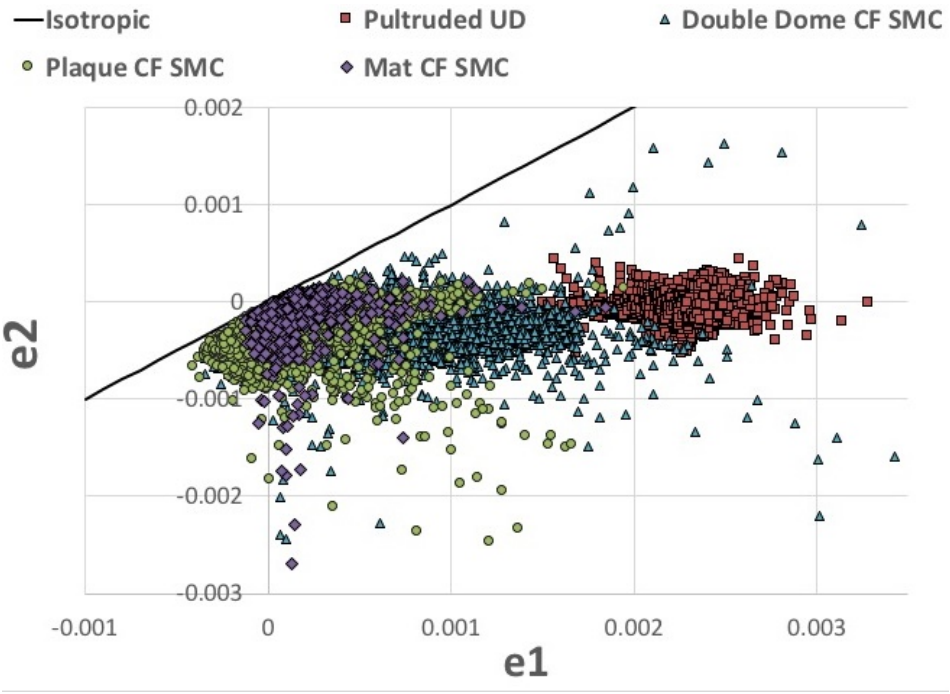

Figure 40. Plot of spatial principle strain states over the surface of three molded carbon fiber SMC samples and a pultruded UD carbon fiber sample. The larger the distance from the isotropic line a point is, the stronger orientation at that point.

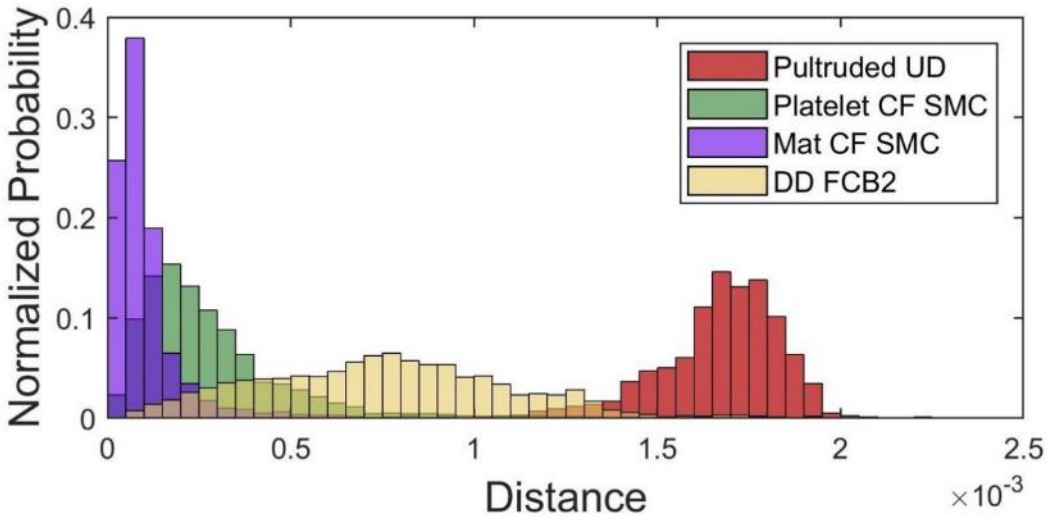

Figure 41. The distribution of the geometric distances from isotropic of the spatial strain states present in Figure 40. It is hypothesized that a distance > 0.5e-3 will represent regions of high orientation.

The TDIC technique gives information of spatial regions that have thermal expansion signatures of highly orientated structure and also, the associated fiber orientation. Hence, validation of TDIC orientations was done with X-ray tomography coupled with gradient based orientation analysis. This technique gives the full orientation tensor [23, 25]. To prepare X-ray tomography orientations for comparison with TDIC, the fiber orientation was taken as the first eigen vector of the orientation tensor, which was projected on to the coupon plane of the sample. This process is demonstrated in Figure 37 to obtain orientation histograms for two regions of the double dome part. For TDIC similar histograms were compiled using the surface orientations from the front and back obtained from local thermal expansions. Figure 42 documents the summary of planar orientations from X-ray tomography and TDIC for two double dome parts. A strong correlation regarding the probability density of orientation states can be noticed between X-ray tomography and TDIC orientation histograms for both double dome parts. Furthermore, the front and back TDIC orientations for each dome location correlate strongly, suggesting the development of macrostructure as the result of compression molding induced flows local to that part region. The matching orientations histograms between the two modalities indicates that TDIC can be used as a first level approximation for the rapid determination of part performance. Additionally, despite the superficial nature of the surface measurement approach, previous research on these materials has suggested that surface strain patterns have reasonable subsurface information content and as such are useful for part performance prediction [20]. Thus, while a sacrifice is made in depth and specificity of information, the TDIC method offers advantages in speed of measurement and

field of view. Furthermore, TDIC still captures much of the general and most distinctive features critically relevant to part performance.

In practice, TDIC could be used as a quality control technique to validate parts as a final step in fabrication by monitoring strains developed simultaneously during the final part cooling step to probe for highly anisotropic regions. This information could be used to determine if parts meet specification and reduce the burden of destructive testing, making light-weight composite materials more attainable. To this end, an example small-scale throughput of the analysis procedure is presented in Figure 43. The procedure here consists of 4 steps:

1. Identifying part regions that have anisotropic thermal expansion.
2. Calculating the fiber orientations from principle strain orientations.
3. Determining the location of part weaknesses by comparing fiber orientations and local anisotropic intensities.
4. Testing part to failure and comparing fracture with predicted TDIC performance.

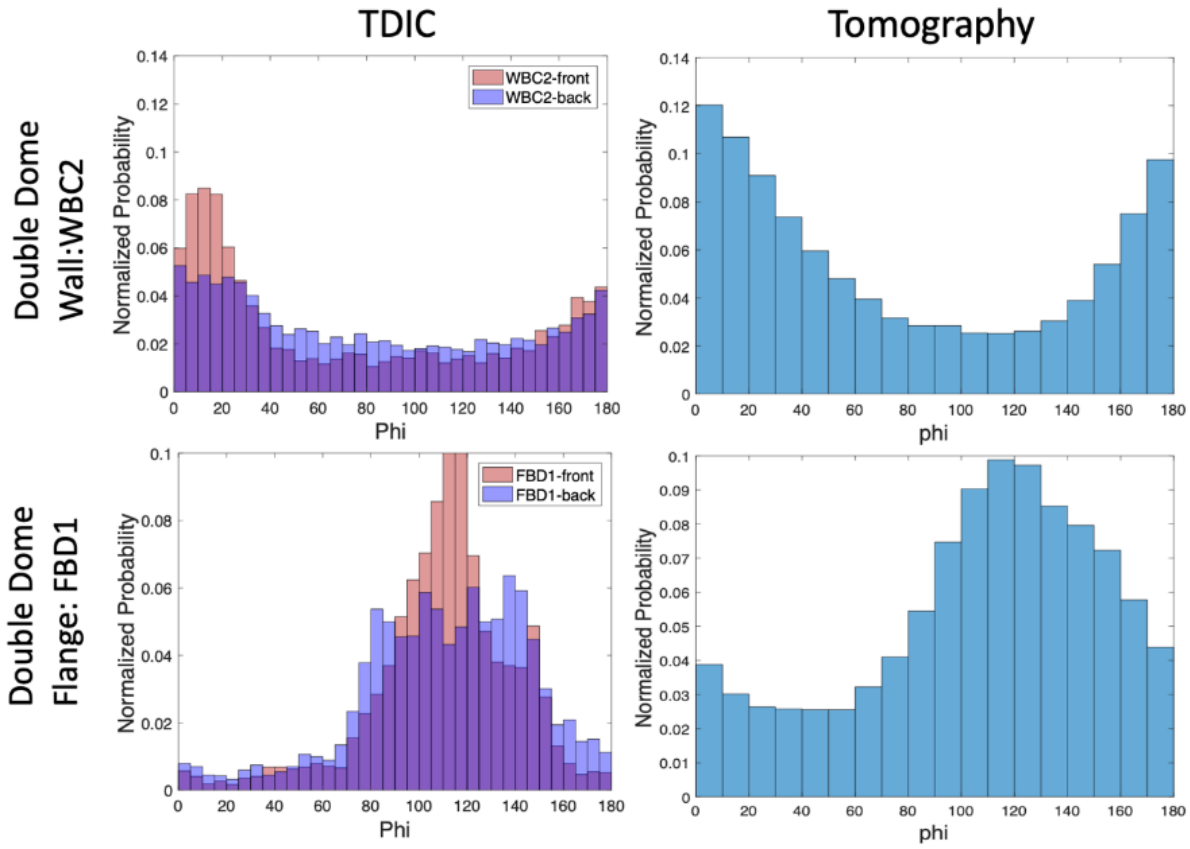

Figure 42. Comparison of in-plane orientation states obtained from projected fiber orientations from X-Ray tomography and TDIC approach, demonstrating excellent correlation between the two modalities.

For double dome coupon WBC3 in Figure 43, the overlapping combination of transverse orientation to the tensile axis with highly anisotropic thermal expansion occurred near the center, as outlined by the box in sequential images. Thus, when performing tensile testing with on-

specimen DIC surface strain tracking, high strains were observed in the same regions TDIC suggested [17].

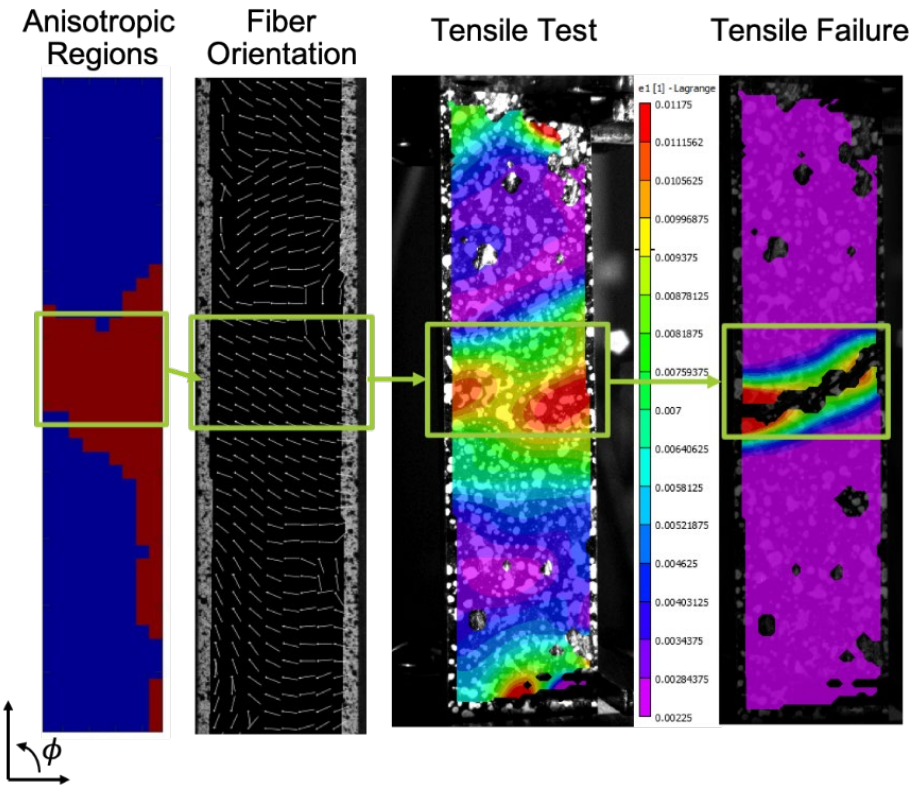

Figure 43. Example execution of TDIC to determine failure regions nondestructively for double dome sample WBC3. Regions that have highly anisotropic behavior are mapped in red against blue (isotropic regions). Overlap of vectors closer to 0 or 180 with red regions, correlates with areas of high tensile strain from DIC strain maps and ultimately location of part failure .

4.3.3 Conclusions from X-ray and Thermal DIC Analysis

The novel carbon fiber platelet-based SMC system, which favorably competes with aluminum as an alternative light weight engineering material, demonstrates strong potential for automotive parts. This composite material system is capable of achieving superb mechanical performance, 300 MPa failure stress, and 40 GPa modulus for flat plaques. Furthermore, complex geometry parts can be fabricated rapidly, at very competitive cycle times, using largely existing infrastructure of automotive manufacturing employing a compression molding approach. The effect of molding complexity on part performance was studied using a cradle-to-grave approach, including fabrication, extraction, nondestructive inspection, and destructive evaluation. It was found that performance hinged on maintaining a random orientation state during manufacturing, which is also supported by authors interrogating similar material systems. Highly oriented regions of platelets can develop during material flow. Platelet orientation has been identified as a critical parameter in predicting the performance of these SMC material systems, in particular

elastic response. These can create weakness in transverse direction mechanical properties unless layers above and below this location can compensate. The detection of these locations typically requires the destruction of the part using conventional microscopy-based methods with very small field of view and extremely laborious effort. Thus, the mechanical characterization of large parts for quality control and performance benchmarks can be challenging. To this end, a new technique, thermal digital image correlation (TDIC), demonstrated here has been presented as a viable solution to understand the orientation behavior of the carbon/epoxy-based platelets in a molded part. This technique is extremely fast, is easily scalable for large part size, and can be implemented in a manufacturer's assembly line without significant disruption of the manufacturing process. A strong correlation between X-ray tomography and TDIC orientations was found for parts that exhibited fiber alignment during the manufacturing process.

4.4 Surface Analysis and Adhesive Bond Durability

4.4.1 Background

The presence of an internal mold release (IMR) as an additive to the epoxy matrix resin of a CF-composite was investigated for its role in affecting surface and interfacial properties and performance. The concern is that the presence of the IMR would decrease the surface energy of the epoxy, changing it from a wettable to a non-wettable surface. As a result, adhesion between the CF and the epoxy would be reduced, and it would be expected that the effectiveness of adhesives for part-joining and the durability of paint applied to the cured composite surface could also be impacted.

The utilization of Dow's VORAFUSE M6400 molding compound will depend not only on the ability to process the composite prepreg platelets in less than 180 seconds, but also on several related steps in the manufacturing process. These include short cycle time for insertion of the charge into the mold, short cycle time removal of the compression molded composite part from the mold, treatment of the composite surface to prepare it for adhesive bonding and/or painting that provides an acceptable level of adhesion, and long-term durability of the composite in its designed application.

In order to achieve the desired production rate using the VORAFUSE M6400 epoxy composite system, parts need to be manufactured and demolded in less than 180 seconds. Quick release of the cured composite without contamination of the mold surface is essential and is normally achieved by applying an external mold release to the mold surfaces between cycles. The Dow VORAFUSE™ epoxy system has incorporated an IMR, the purpose of which is to migrate to the molded part surface during processing to allow easy and fast removal from the mold.

The IMR compound is effective because it is not chemically bound into the cross-linked epoxy network. Therefore, it is free to migrate to internal and external surfaces of the composite at very small concentrations under free energy thermodynamic forces. The use of this internal mold release as an additive component to the epoxy resin formulation, is compatible with and does not have a deleterious effect on the cured epoxy mechanical properties. The composition of the IMR is proprietary but can be characterized as a small molecule of low surface energy soluble in the uncured epoxy and with a strong affinity for high-energy surfaces. While the IMR's primary function is to concentrate at the composite/mold interface, there are several other surfaces and interfaces in the CF/epoxy composite where it can also concentrate. At the surface of the carbon fiber filaments, the IMR could cause a reduction in carbon fiber–epoxy adhesion; at the surface of the epoxy platelet prepreg, it could reduce platelet adhesion and consolidation; at the external surface of the molded composite, it could affect the molded composite-paint interface and the molded composite-adhesive interface. As a result, it is possible that after manufacture, the composite could have reduced mechanical properties and reduced adhesion of a structural adhesive or paint, leading to possible reduction in the durability of adhesive or paint under long-term environmental exposure. The purpose of this task is to determine if the use of this IMR has deleterious effects on CF-epoxy adhesion, cured epoxy composite paintability, and adhesive bonding to the cured epoxy composite (Figure 44) at the nano, micro, meso, macro, and structural levels.

To investigate the effect of IMR on adhesion at the above interfaces, composite plaques up to 300-x-300-mm plaques were manufactured with the carbon fibers and epoxy matrix within the range of temperature, time, and pressure expected to be encountered in manufacturing. Samples from these plaques were tested in isolation and as assemblies bonded to aluminum substrates.

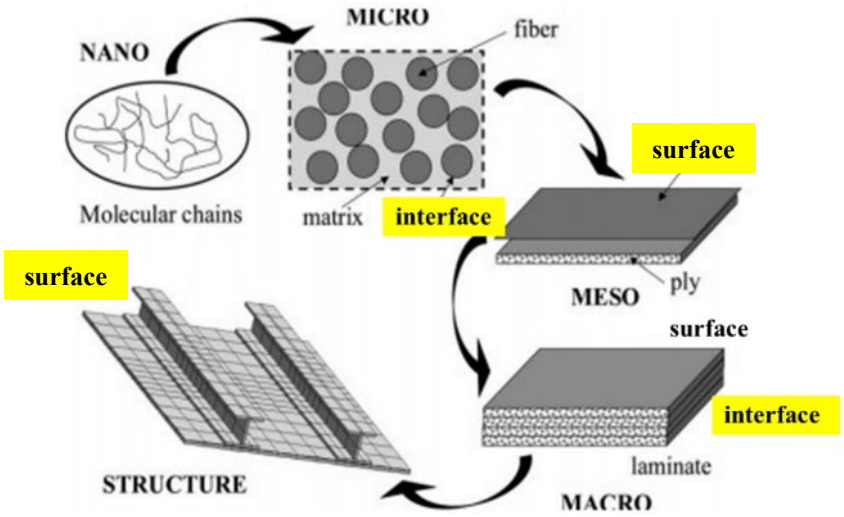

Figure 44. Structural levels of IMR / Composite interactions.

At the nano level, the adsorption of the IMR to the CF surface was investigated. Single CF coupons were fabricated to identify failure modes at the fiber-matrix interface under shear loading. Composite specimens were tested for modulus, strength, and fracture toughness. The surface of a portion of the cured compression molded CF-epoxy 30x-30cm plaques was examined with physical (contact angle), optical, surface microscopic and spectroscopic analytical methods to quantify the surface energy and the presence, amount, and distribution of the internal mold release. This was compared with the baseline CF-epoxy without IMR. A priming and painting protocol, based on industry practices, was implemented to paint the composite panels. Failure surfaces were examined with surface microscopic and spectroscopic analytical methods to identify the failure mode and constituent composition in the failed interphase, with attention directed at quantifying the presence, amount, and distribution of the IMR.

Multi-material adhesive joints (aluminum-to-polymer composite) and paint adhesion mechanical tests, as well as durability tests, were also conducted to assess the IMR role. Both adhesively bonded specimens and painted specimens were subjected to durability testing using Ford-defined protocols involving immersion in water at elevated temperature. After testing, a detailed failure analysis was conducted to determine the effect of IMR content and processing conditions on the mechanical properties and identification of the locus of failure. Studies were organized according to the following tasks:

- Investigation of the epoxy system with and without the presence of the IMR to determine if the IMR affects the surface and interfacial chemistry, surface energy, and adhesion to the carbon fiber; to the surface of the partially cured composite platelets, and to the fully

cured surface of the composites using X-ray photoelectron spectroscopic analysis and contact angle measurements.

- Manufacture of single-fiber fragmentation coupons using CF and epoxy with and without IMR to quantify differences between the CF adhesion and failure mode. Preparation of cured CF-epoxy with and without IMR for painting using a representative automotive procedure.
- Manufacturing of compression molded CF-epoxy plaques and testing according to ASTM standard tensile strength, tensile modulus, flexural strength, flexural modulus, short beam shear, transverse flexure, and end-notched flexure fracture methods.
- Scanning electron microscopic examination of the fracture surfaces to identify differences between the IMR epoxy system and the IMR-free epoxy system. X-ray photoelectron spectroscopic analysis of the plaque surface and internal fracture surface to identify the presence of and location of the internal mold release. Contact angle measurements on the cured plaque surfaces of the epoxy with and without IMR.
- Durability testing of both adhesive bonded specimens and painted specimens to Ford specifications for salt, wet, and elevated temperature 8-week conditioning. Testing of painted panels for inter-coat adhesion and morphological changes after water immersion according to Dow specifications.
- SEM examination and X-ray photoelectron spectroscopic analysis of the fracture surface to identify the presence or absence of IMR on the adhesive side of the fracture.
- Preparation of cured CF-epoxy with and without IMR for painting using representative automotive procedures to Ford contractor. Long-term environmental durability testing according to Ford internal protocol to evaluate role of the IMR.
- In collaboration with the Purdue University simulation team, manufacture of bonded specimens with VORAFUSE™ M6400 and GFRP/aluminum adherends for correlation of predicted and measured deflection after thermal cycling.
- Determination of the curing kinetics of the candidate adhesives using differential scanning calorimetry (DSC): i) Degree of cure as a function of temperature and time; ii) Rheology as a function of temperature and time; and iii) Dynamic mechanical analysis (DMA) to measure modulus as a function of temperature and time. Identify minimum time and temperature conditions to produce ‘green’ strength. Transfer measurement results to the Purdue team in support of the modeling and simulation effort.

4.4.2 Materials

Note: All composites and their constituents investigated in this study were supplied by Dow Chemical and Ford Motor Company.

4.4.2.1 Resins

The resins (Vorafuse™ M6400 with and without IMR) were supplied by Dow as cured plaques and as bulk components. The formulations are listed in Table 4.

Table 4. Vorafuse™ formulations

	VORAFUSE™ M6400 with Licolub® WE4	VORAFUSE™ M6400 without Licolub® WE4	VORAFUSE™ M6400 / no IMRs
Component	wt. (g)	wt. (g)	wt. (g)
M6400 Resin Blend with IMR	20.00		
P6300 Resin Blend without IMR		20.00	20.00
P6020 Curative paste (Dicy)	4.30	4.50	4.50
Accelerator Paste	3.12	3.27	3.27
IMR #2	0.70	0.74	0.00

Storage, handling and curing of these resins followed the instructions and procedures provided by Dow.

4.4.2.2 Adhesives

Three adhesives were supplied by Dow for investigation and characterization. All materials were stored at room temperature.

1. Betamate 73326M/73327M was a two-component adhesive supplied in a dual cartridge dispenser. It was kept at room temperature during dispensing, mixing and application. The cure cycle used was 30 min @ 190°C.

2. The second adhesive, identified as 1K-Flex, was supplied in a single cartridge and was kept at room temperature during dispensing, mixing, and application. It was cured for 20 min @ 190°C.

3. The third adhesive, identified as 2K-Flex was a two-component system, supplied in bulk. It was formulated at an A:B ratio of 10:0.8 (weight). It was held at 60 °C during handling to allow dispensing, mixing, and application. Two cure cycles were used for the 2K-Flex: 8 hr @ 60°C or 8 hr @ 60°C followed by a heat cycle of 10 min @ 190°C.

Glass beads of 355 to 425 microns were added at 1% w/w as bond line spacers to the adhesives

that were compounded in a Speed-Mixer® (FlackTek, Landrum, SC) using two cycles of 30 sec at 3000 rpm.

4.4.2.3 Aluminum

Aluminum sheet, 6111, was supplied by Ford, nominally 18-x-18-in x 0.039 in. The as-received material had a visible, oily coating on its surface.

4.4.2.4 Primer

The samples were individually wrapped in ultraclean aluminum foil immediately after surface treatment and sent by next-day air for priming at Red Spot (Evansville, IN). The samples were primed with Grey 2K SMKC primer (UBP9762JANG).

4.4.3 Methods

4.4.3.1 Contact Angle

Contact angle is a method for measuring the wettability of the surface of a solid material by a liquid. Wetting is defined as the manifestation of the attractiveness of the liquid molecules to the solid surface. When a small drop of the liquid is placed on a surface, it will achieve an equilibrium droplet shape, and the contact angle is defined as the angle which the liquid makes with the surface at the droplet edge. For a given liquid, if the wetting attractiveness is larger, the smaller the contact angle. A wetting liquid has a contact angle on the solid of less than 90º. A nonwetting liquid has a contact angle between 90º and 180º. A water droplet is typically used to assess wetting changes in a surface. For example, the contact angle of water on a surface may be ~50º on a cured and clean polymer surface but increase significantly if that surface is subsequently contaminated with a mold release such as the IMR being studied here.

Water contact angles were measured using a Krüss model DSA 10 Mk2 Drop Shape Analysis System® equipped with a microliter dosing syringe. HPLC grade water was used to form 3 µl sessile drops on the surface of interest, and their contact angles were recorded after 15 seconds. The contact angles for five separate drops were measured for each surface.

4.4.3.2 Surface Analysis – X-ray Photoelectron Spectroscopy -XPS

X-ray photoelectron spectroscopy (XPS) is a surface-sensitive quantitative spectroscopic technique that measures the elemental and molecular composition of the first 0 to 10nm of a solid surface being analyzed. XPS spectra are obtained by irradiating a material with a beam of X-rays while simultaneously collecting and measuring the kinetic energy and number of photoelectrons that escape from the surface being analyzed. XPS can be used to analyze the surface chemistry of a material in its as-received state, after some treatment, after fracture, after cutting or polishing, or after exposure to thermal or chemical environments. XPS detects all elements with an atomic number of (Z) = 3 or higher at concentrations in the parts per thousand range in any solid material stable in a high-vacuum environment.

Both optical microscopy and XPS, analysis of the materials were used to characterize the surface morphology as well as the atomic and molecular composition of the various cured polymer and

polymer composite surfaces before and after treatment, after fracture resulting from testing, or after exposure to plasma and ultraviolet light.

4.4.3.3 Mechanical Testing

Aligned carbon fiber reinforced Vorafuse™ composites with and without IMR were supplied by Dow. Two panels each of the layups listed below (with and without IMR) were provided for the ASTM tests listed (Figure 45):

ASTM D3039 8-ply unidirectional 0° and 90° tensile
ASTM D790/D7264 8-ply unidirectional 0° and 90° Flexure
ASTM D2344 16-ply Unidirectional (ILSS)
ASTM D7905 Mode I interlaminar fracture toughness
ASTM D4541 8 ply [+/- 45]2s PATTI test.

Tensile testing (0° and 90°) was carried out following ASTM D3039 on five specimens at ambient laboratory conditions. The specimens were tabbed with glass-reinforced epoxy with tapering for the 0° tensile specimens. The strain was measured using a Class B-1 extensometer with a gage length of 25.4 mm. Modulus calculations were performed over the range of 0 to 2.5 mm extension.

Flexural testing was carried out following ASTM D790 at a span to depth ratio of 40:1 on five specimens for each condition. Modulus calculations were performed over the range of 0.00 inch to 0.05 inch deflection.

The interlaminar shear testing (short beam shear) was carried out following ASTM D2344 with a sample size of 10.

Chopped carbon fiber/Vorafuse™ composites with and without IMR were used for primer adhesion studies.

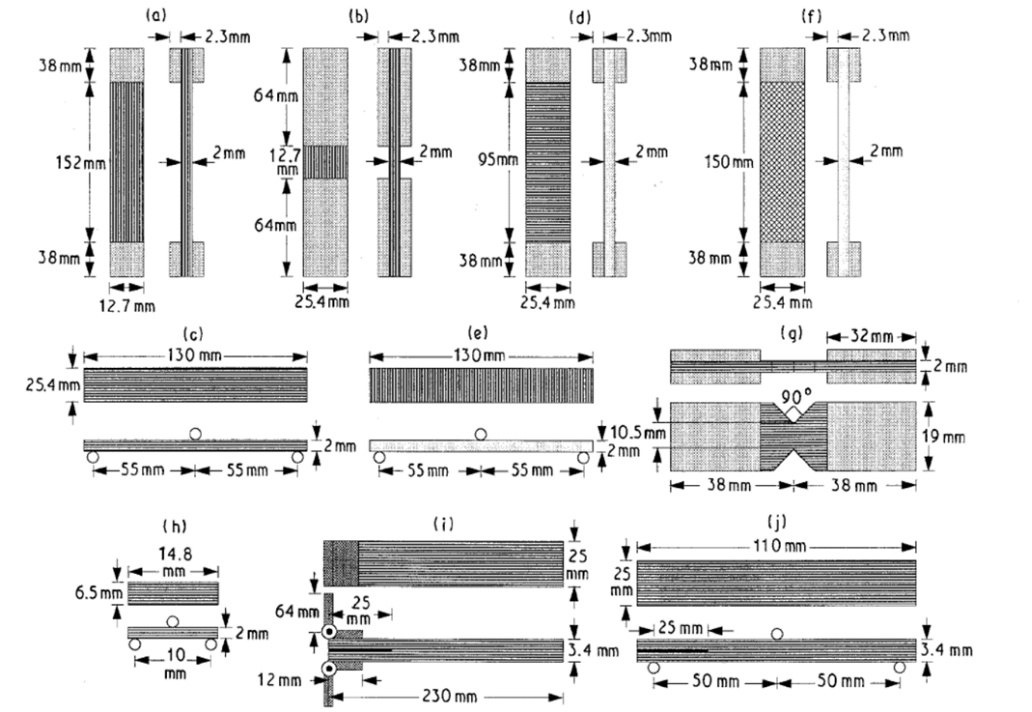

Geometries and dimensions of (a) [0] tension, (b) [0] compression, (c) [0] three-point flexure, (d) [90] tension, (e) [90] three-point flexure, (f) [+/- 45] tension, (g) Iosipescu shear, (h) short-beam shear, (i) [0] DCB, and (j) [0] ENF composite specimens.

Figure 45. Mechanical test specimen geometries.

4.4.3.4 Differential Scanning Calorimetry (DSC)

Differential scanning calorimetry, or DSC, is a thermoanalytical technique in which the difference in the amount of heat required to increase the temperature of a sample compared to a reference material is measured as a function of temperature. The result of a DSC measurement is a curve of heat flux versus temperature or versus time. Events which give off heat compared to the reference are exothermic, and those that absorb heat are endothermic. Differential scanning calorimetry can be used to measure fusion and crystallization events as well as glass transition temperatures (Tg). DSC can also be used to study chemical reactions. TA Instruments DSC 2000 was used to evaluate the calorimetric properties of the adhesives.

4.4.3.5 Dynamic Mechanical Analysis (DMA)

Dynamic mechanical analysis, or DMA, is a technique used to study the viscoelastic behavior of polymers. A sinusoidal stress is applied to a polymer sample and the strain in the material is measured, allowing one to determine the complex modulus. The temperature of the sample or the frequency of the stress can be varied, leading to variations in the complex modulus. This method can be used to locate the glass transition temperature of the material, as well as to identify transitions corresponding to other molecular motions. TA Instruments DMA Q800 operated at a frequency of 1 Hz was utilized for DMA measurements.

4.4.3.6 Rheology

Polymer rheology testing is the study of how the stress in a material or force applied is related to deformation and flow of the material. Rheology testing of polymers is used to determine the

rheological (flow) properties of polymers to optimize processing and properties. For a thermosetting polymer, rheology can provide information about the time-temperature conditions on the development of the cross-linked structure. Parallel plate rheology was conducted with a TA Instruments ARES rheometer.

4.4.3.7 Surface Treatments

The surfaces of the composites and the aluminum were used either as-received, which involved only careful handing to minimize contamination, or were 'surface treated' using isopropyl alcohol (IPA) cleaning, treating with a Plasmatreat Open-air system, or treated with ultraviolet light + ozone exposure.

Isopropyl Alcohol (IPA) Cleaning. A technician hand-operated solvent cleaning method that? involved swabbing the surface with an isopropanol-saturated Wipe-All®, allowing it to stand 10 sec wet, and then wiping dry.

Plasmatreat. An Open-air-Plasma® treatment unit was supplied by Plasmatreat North America (Elgin, IL). This technology supplies a plasma at atmospheric pressure to clean and chemically activate polymer surfaces by incorporating oxygen and nitrogen groups.

The plasma is formed in a stream of compressed air that is discharged from a rotating nozzle uniformly contacts the surface at a predetermined width and distance from the plasma nozzle to the surface being treated, as shown in Figure 46.

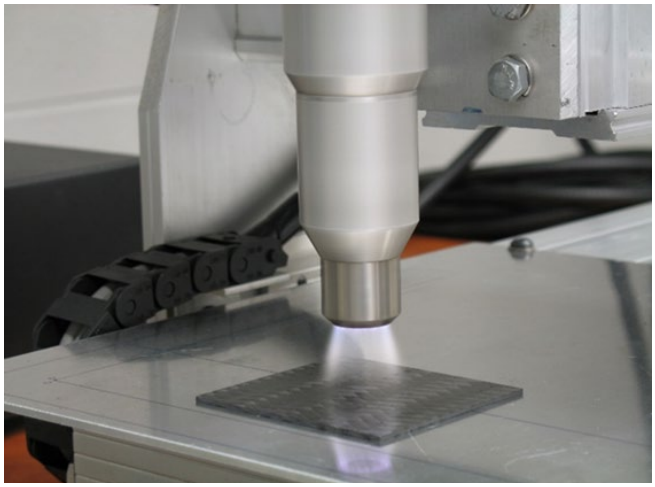

Figure 46. Open-air-Plasma® treatment jet nozzle.

The system used in this investigation consisted of a control unit (FG5001), a plasma jet with a rotating wide-area nozzle (RD1004, 22892). The nozzle determines the width of the treatment path, which in this case was 55 mm. The plasma jet was mounted on a CNC unit that allowed the plasma nozzle to be moved across the surface at speeds of up to 2.0 m/min.

Ultraviolet Light Ozone (UVO). The UVO surface treatment uses a combination of high-intensity-pulsed UV light that passes through an oxygen/ozone atmosphere, Figure 47. The UV light is generated by a Xenon® model RC-500 system (Wilmington, MA). The specimens were treated in a closed chamber with a quartz window. A continuous flow of oxygen was delivered to the

chamber, and ozone was delivered by a supplemental ozone generator. The specimens were placed 1in from the window of the lamp, and the treatment times ranged from 10 to 180 sec. The UV photon flux ranged in wavelength from 185 nm to more than 350 nm, which also formed additional ozone.

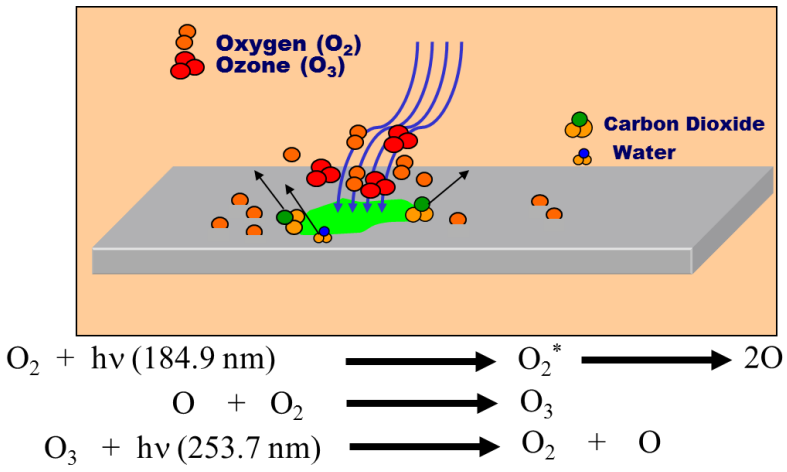

Figure 47. Schematic of the UVO treatment process.

4.4.4 Results

The following sections contain results for the adhesive, thermo-physical and tensile properties of adhesives used in this study.

4.4.4.1 Adhesive Characterization

4.4.4.1.1 Thermophysical Properties of Adhesives

Three adhesives were evaluated for their thermophysical properties by differential scanning calorimetry, parallel plate rheology, thermal mechanical analysis, and dynamic mechanical analysis, and for their tensile strength and stiffness.

1. Dow 2K-Flex is a two-part experimental adhesive that requires heat cure.
2. Dow 1K-Flex is a single-component experimental adhesive and requires heat activation to cure.
3. Betamate 73326M is a commercially available two-part structural adhesive that is room-temperature curable or heat curable.

The thermophysical properties were collected and provided to the Purdue team for incorporation into their kinetic, flow, and dimensional stability models. A summary of the thermal properties of the three adhesives is provided below, followed by the strength and modulus measurements.

<u>Dow 2K-Flex Differential Scanning Calorimetry (DSC)</u>

A TA Instruments DSC 2000 was used to evaluate the calorimetric properties of the adhesives.

For the 2K-Flex adhesive, the program protocol is an 8-hour isothermal hold at 60°C to allow the adhesive to set up while holding tolerances of the liftgate bonded structures. DSC did not detect an exothermic response when the 2K-Flex was cured isothermally for 8 hours at 60°C, 70°C, 80°C, or 90°C, as shown in Figure 48.

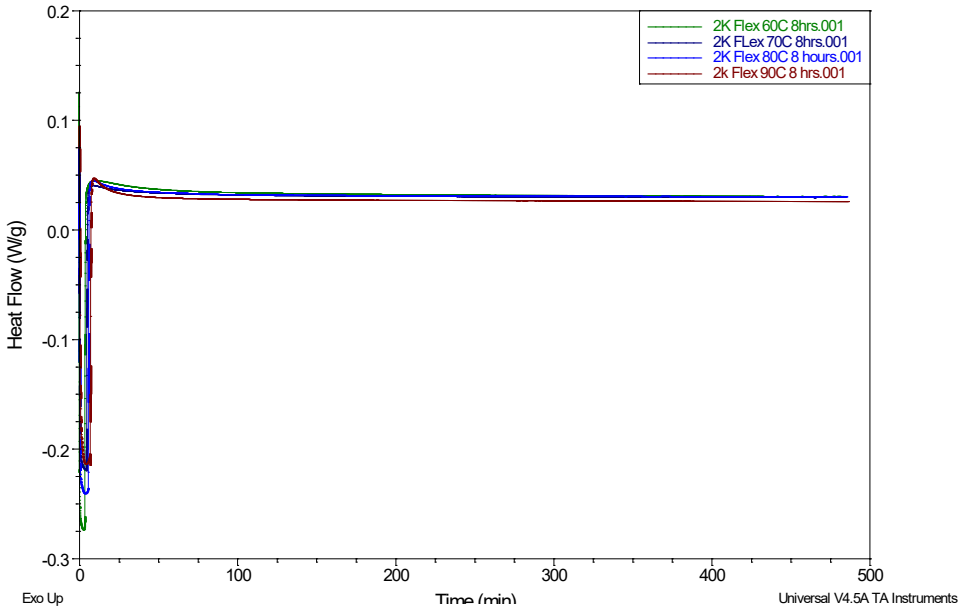

Figure 48. Isothermal thermograms of 2K-Flex.

The 2K-Flex was evaluated by DSC as a function of isothermal cure time at 60°C. Specimens were harvested following 1, 2, 3, and 8 hours at 60°C, Figure 49. Also included in Figure 49 is a temperature sweep of 2K-Flex immediately after mixing. As expected, the exothermic response diminishes with longer exposure periods at 60°C.

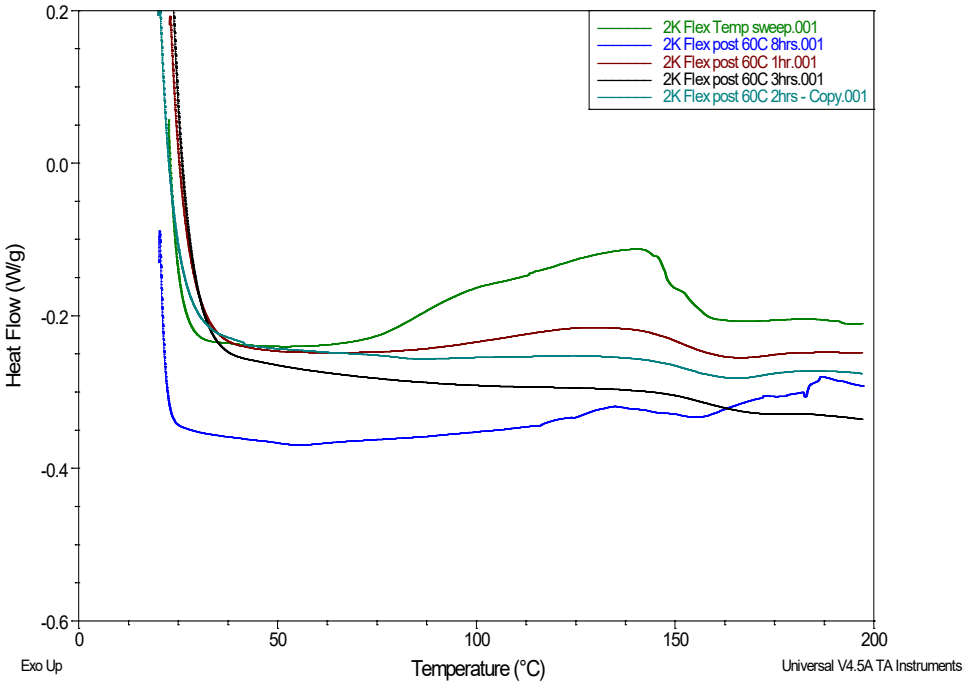

Figure 49. 2K-Flex temperature sweep as a function of isothermal soak time at 60°C.

2K-Flex was also characterized by DSC as a function of ramp rate. An overlay chart of DSC curves collected at ramp rates of 3°C/min to 40°C/min is shown in Figure 50.

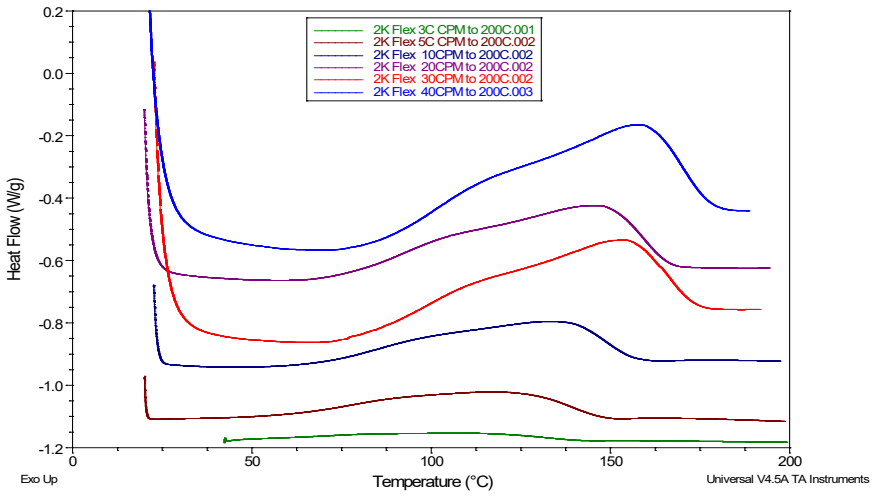

Figure 50. DSC overlay of 2K-Flex as a function of ramp rate.

Dow 2K-Flex Rheology

Parallel plate rheology was used to characterize 2K-Flex with a TA Instruments ARES rheometer. Figure 51 shows a temperature sweep at 3°C/min. The viscosity begins to build at 60°C and reaches a plateau at ~140°C, Figure 51. 2K-Flex was also evaluated under isothermal conditions at 60°C and 90°C, shown in Figure 52. As expected, the 2K-Flex viscosity reaches a plateau more quickly when processed at 90°C.

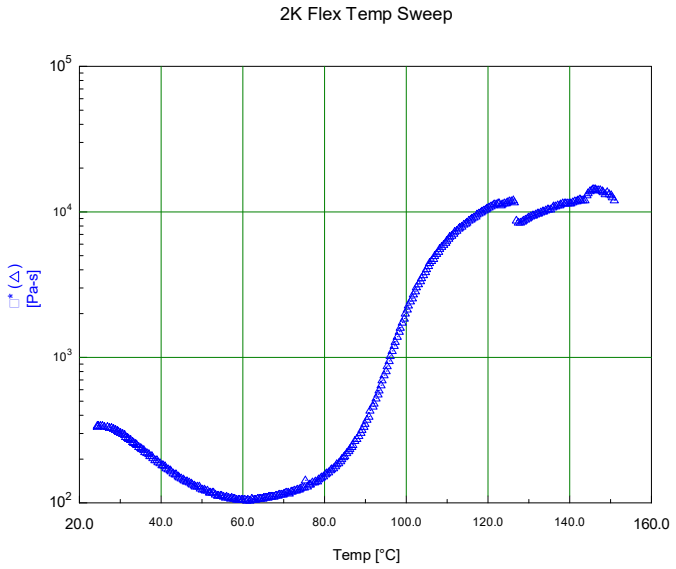

Figure 51. Parallel plate temperature sweep of 2K-Flex.

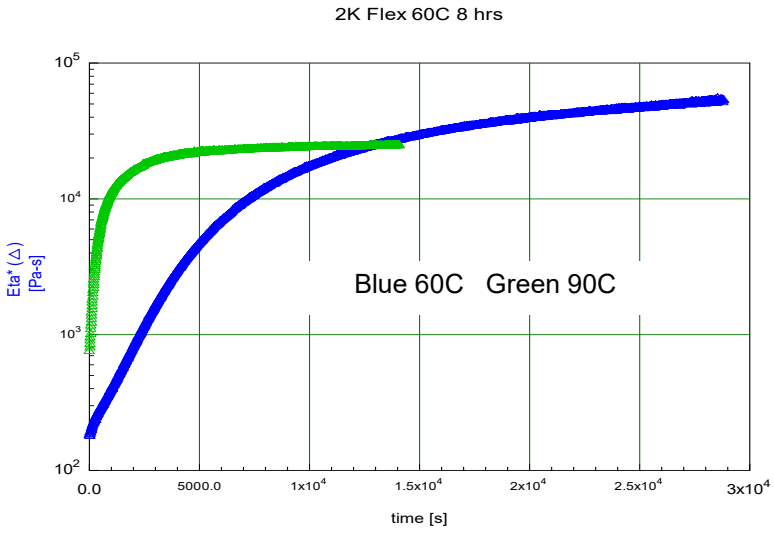

Figure 52. Isothermal rheological profiles of 2K-Flex at 60°C and 90°C.

Dow 2K- Flex Thermal Mechanical Analysis (TMA)

The thermal mechanical properties were collected on a TA Instruments Q400 TMA. Specimens were harvested following 1, 2, 3, and 8 hr at 60°C. TMA thermograms are presented in Figure 53, and the overlay chart in Figure 54.

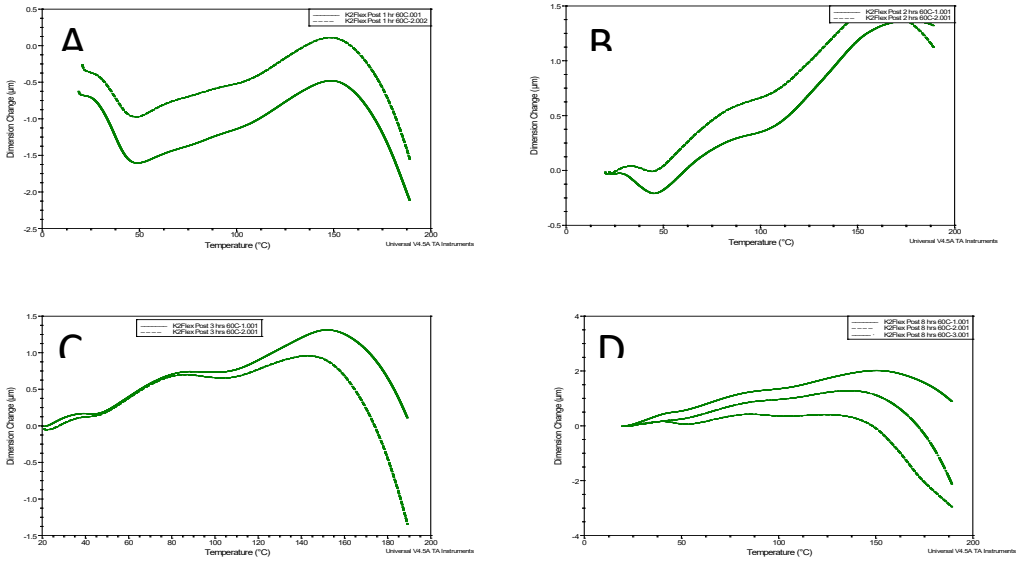

Figure 53. TMA response following isothermal hold at 60°C for (a) 1 hr, (b) 2 hr, (c) 5 hr, and (d) 8 hr.

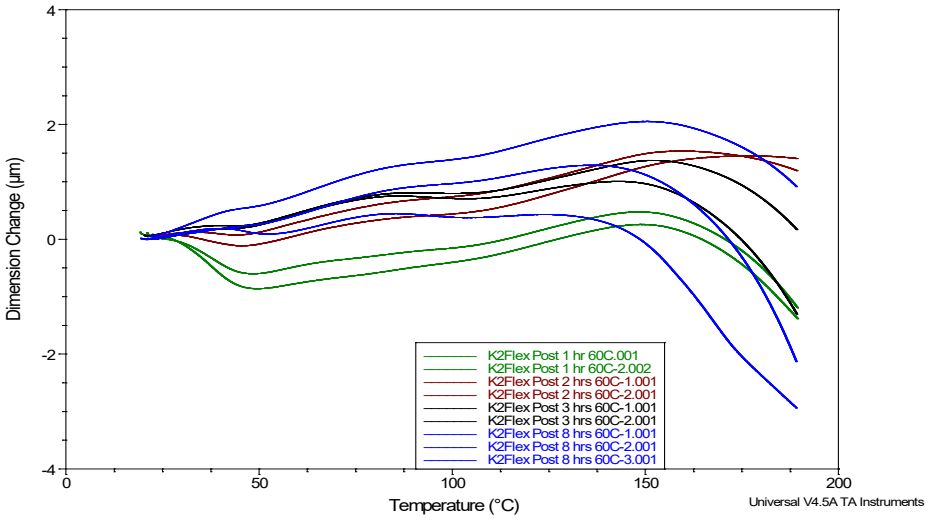

Figure 54. TMA Overlay chart of 2K-Flex versus cure time at 60°C.

Dow 2K- Flex Dynamic Mechanical Analysis (DMA)

The 2K-Flex material was tested using a TA Instruments DMA Q800 operated at a frequency of 1 Hz. The material was tested in four geometries, as shown in Figure 55.

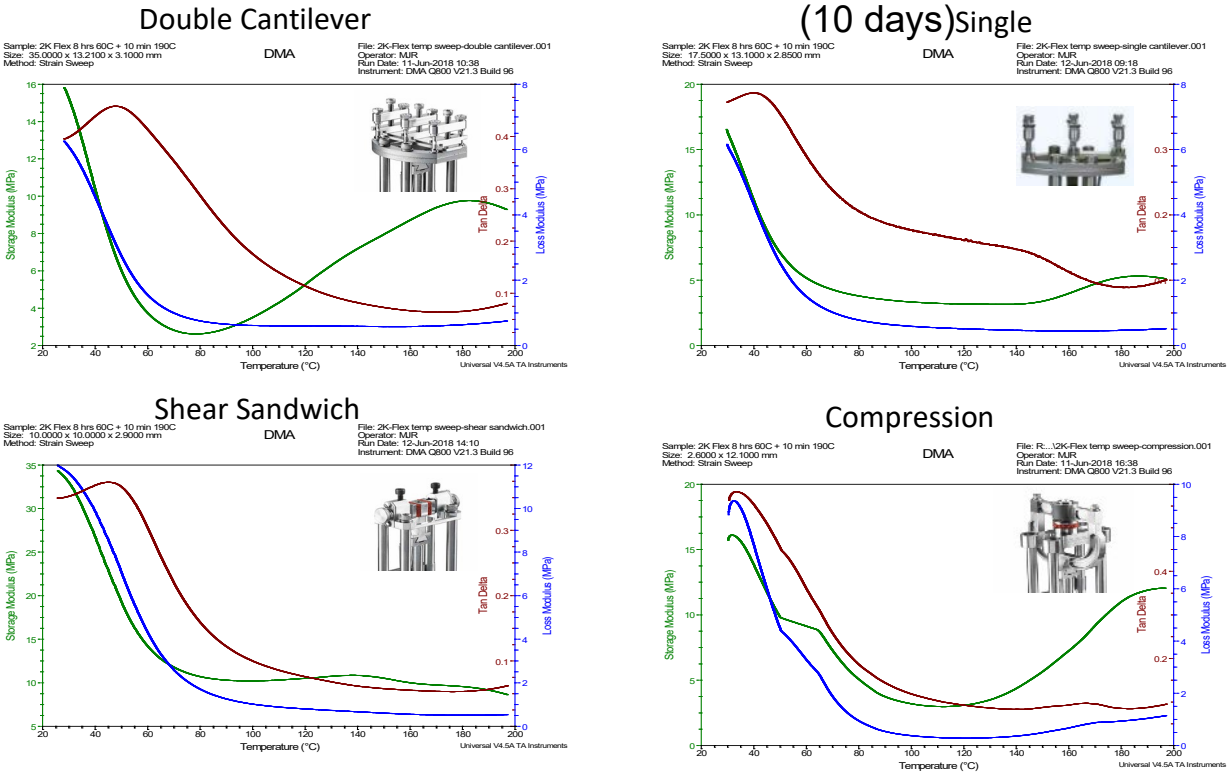

Figure 55. 2K-Flex DMA tested in four geometries.

Dow 1K-Flex Differential Scanning Calorimetry (DSC)

Figure 56 presents a DSC temperature sweep at 10°C/min of 1K-Flex material. The reaction onset is ~150 °C, with a heat of reaction of 95 J/g, and occurs at a significantly higher temperature than 2K-Flex. The DSC as a function of ramp rate for 1K-Flex is shown in Figure 56.

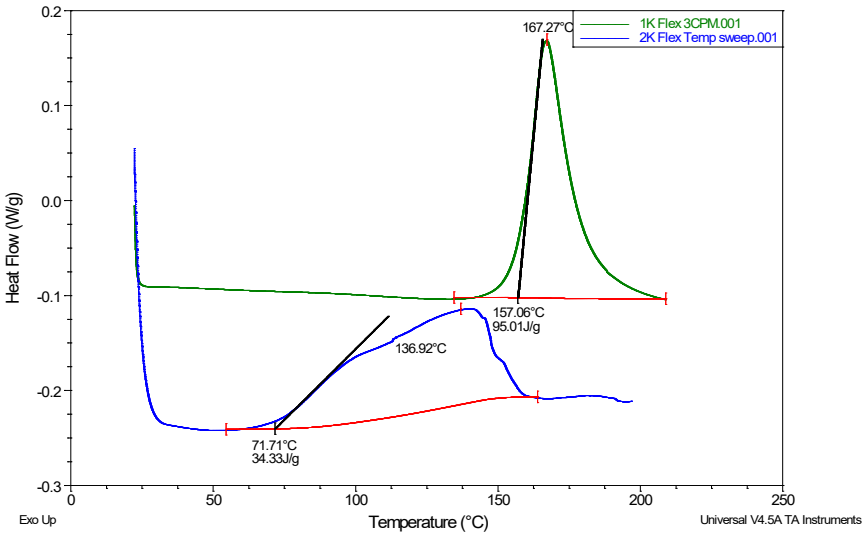

Figure 56. DSC of 1K-Flex (green) compared with 2K-Flex (blue).

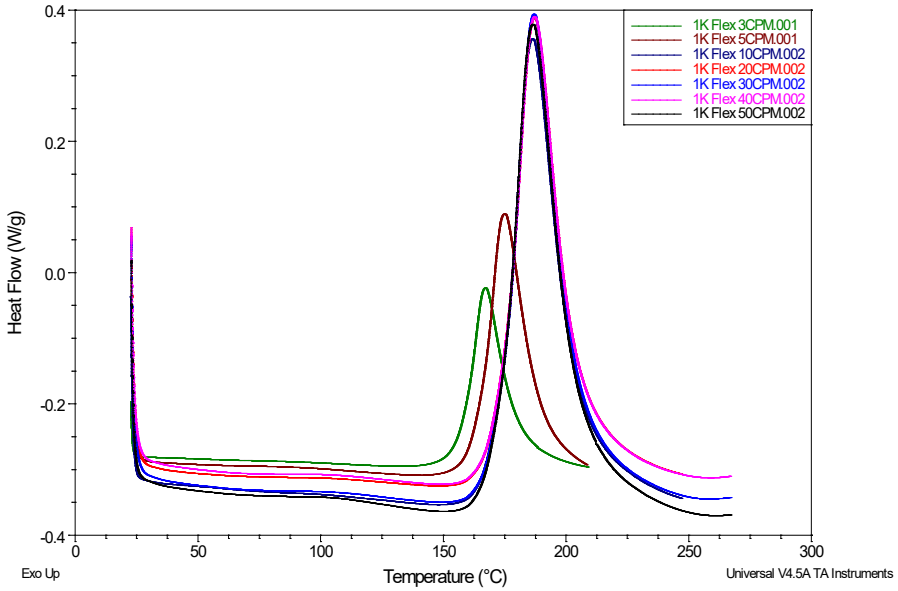

Figure 57. DSC of 1K-Flex as a function of ramp rate.

Dow 1K-Flex Rheology

The results of the parallel plate rheology are shown in Figure 58, including the 2K-Flex for comparison. The 1K-Flex requires higher temperature to polymerize and builds to a greater viscosity than 2K-Flex.

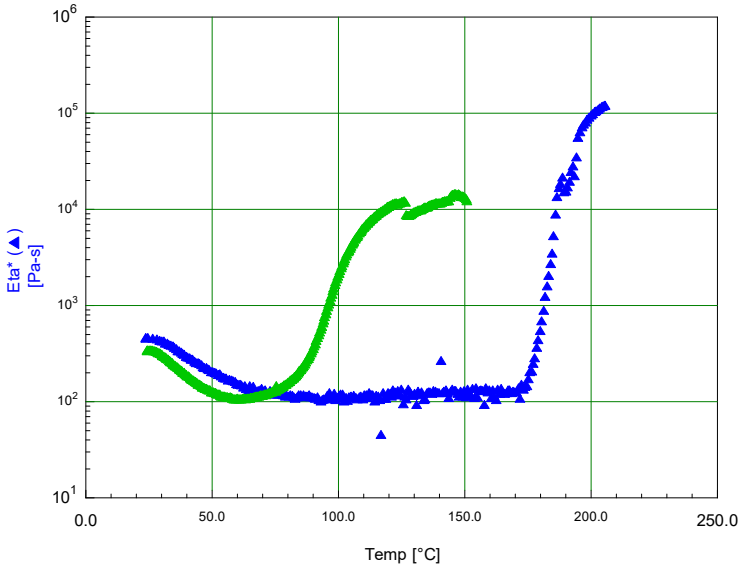

Figure 58. Viscosity profiles of 1K-Flex (blue) and 2K-Flex (green).

Dow 1K-Flex Thermal Mechanical Analysis (TMA)

Figure 59 presents the TMA thermogram of 1K-Flex following standard cure of 20 minutes at 190°C.

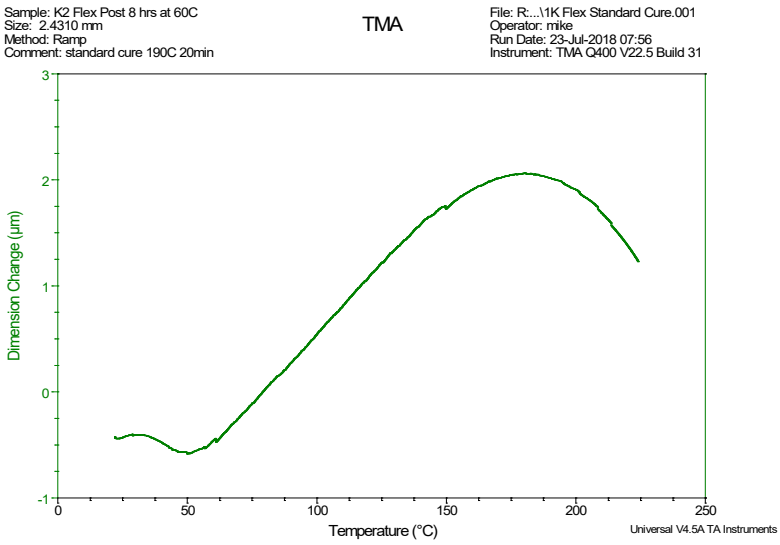

Figure 59. TMA thermogram of 1K-Flex following standard cure at 190°C.

Dow 1K-Flex Dynamic Mechanical Analysis (DMA)

Figure 60 shows the cured 1K-Flex dynamic mechanical analysis collected in the double cantilever mode. The apparent increase in storage modulus at increasing temperature is an artifact caused by thermal expansion exerting supplemental stresses on the DMA drive mechanism. When testing a film of the 1K-Flex in DMA tension geometry, the predicted decay of storage modulus with temperature is observed, Figure 61.

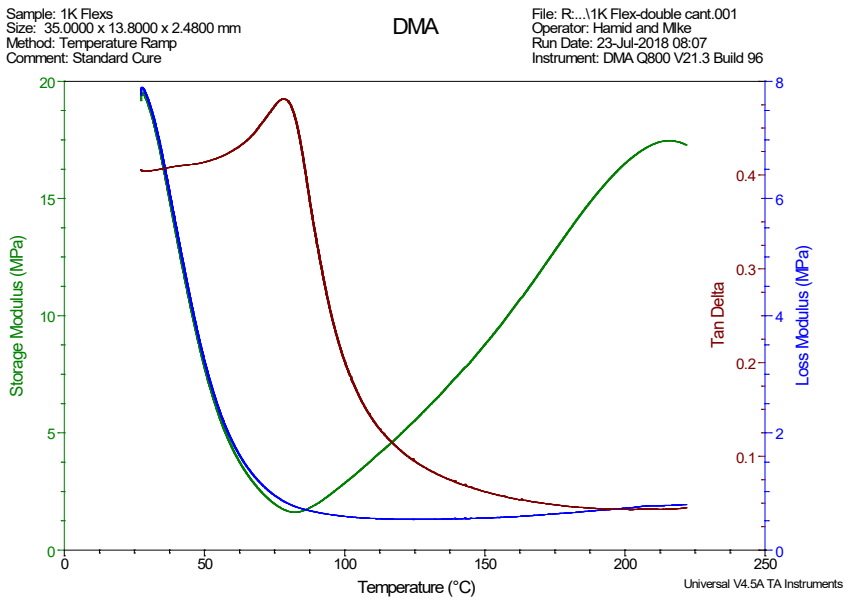

Figure 60. DMA of 1K-Flex in double cantilever geometry.

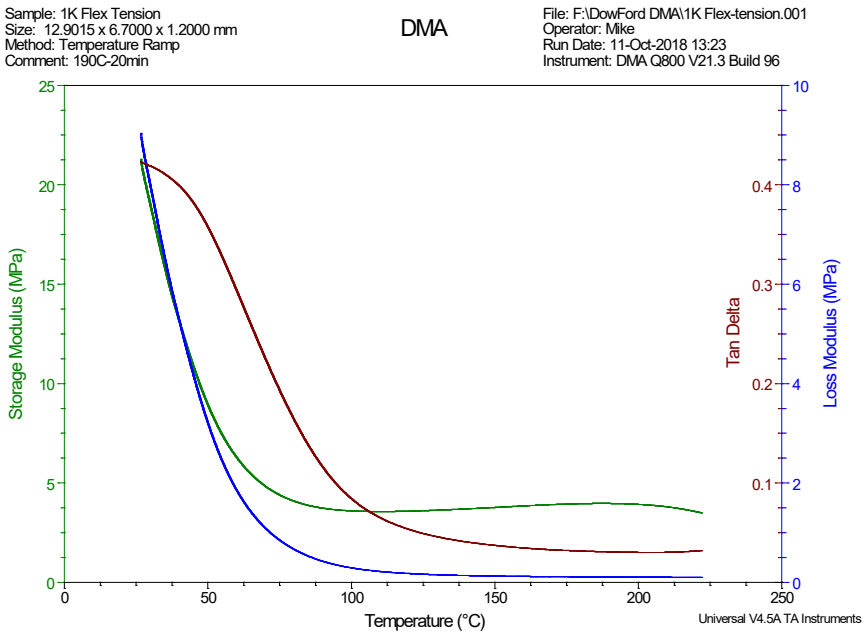

Figure 61. DMA of 1K-Flex film in tension mode.

Betamate 73326M Differential Scanning Calorimetry (DSC)

A DSC time sweep of the Betamate adhesive at ambient temperature of 23°C is provided in Figure 62 and is lacking any significant thermal feature. A temperature sweep at 10°C/min exhibited an exothermic event with heat of reaction of 78 J/g, as shown in Figure 63. DSC of the fully cured Betamate exhibits a glass transition at 37°C, Figure 64. An overlay DSC chart for the 1K-Flex, 2K-Flex, and Betamate systems is provided in Figure 65. DSC as a function of ramp rate from 5°C to 50°C is shown in Figure 66.

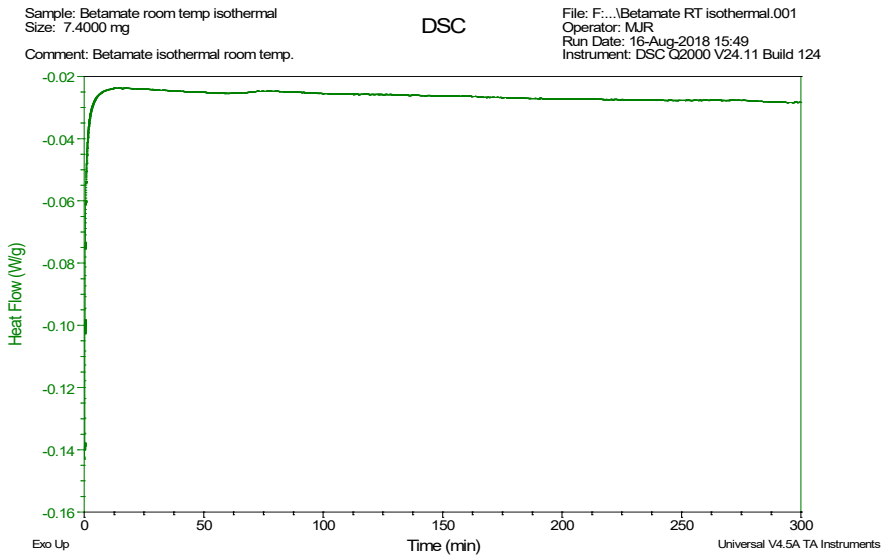

Figure 62. Betamate DSC time scan at room temperature.

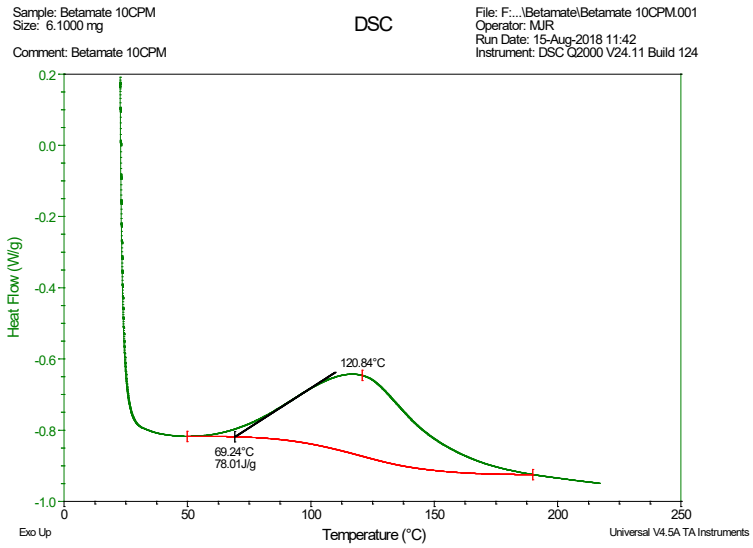

Figure 63. DSC thermogram of Betamate immediately after mixing, collected at 10°C/min.

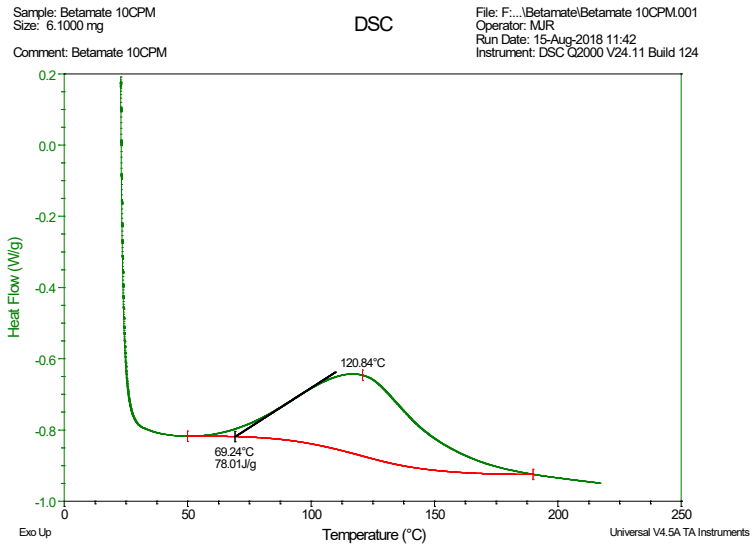

Figure 64. DSC thermogram of Betamate immediately after mixing, collected at 10°C/min.

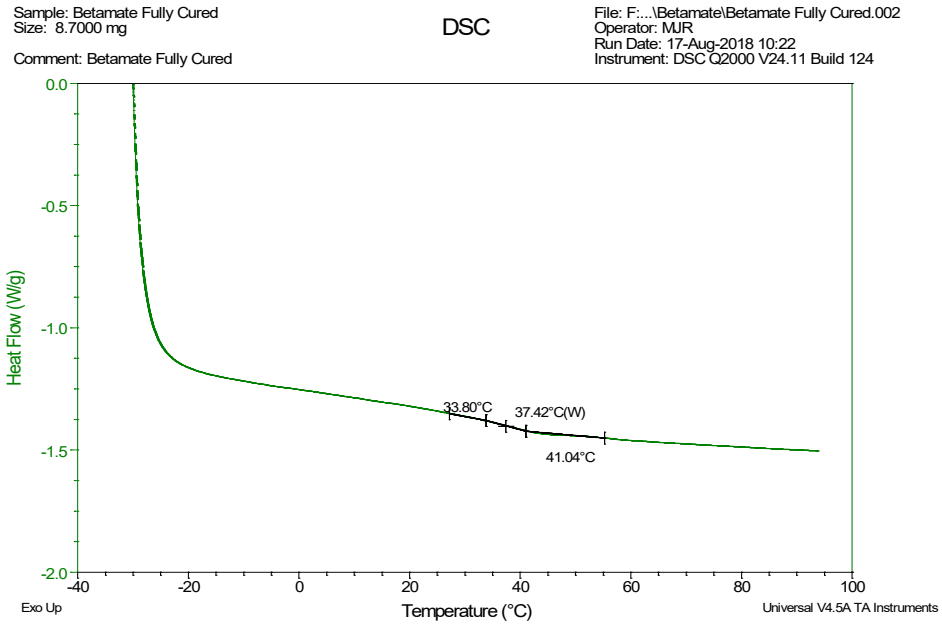

Figure 65. DSC thermogram of fully cured Betamate.

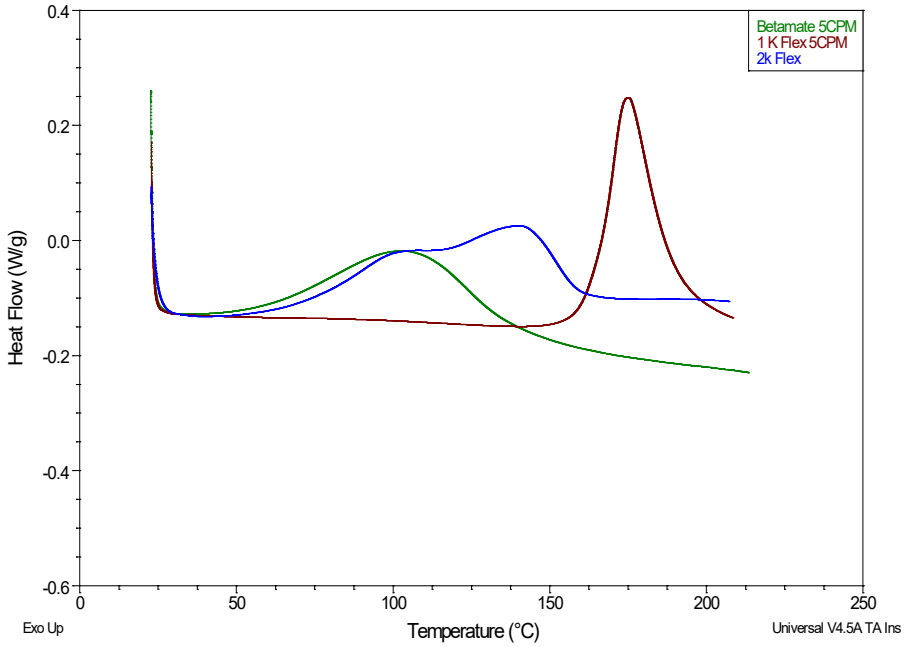

Figure 66. DSC overlay chart for 1K-Flex (red), 2K-Flex (blue), and Betamate (green).

Betamate 73326M Rheology

Parallel plate rheology identified the onset of cure for the Betamate system at ~65°C, and it is fully cured at ~160°C, (Figure 67), similar to the findings obtained by DSC in Figure 64. For comparative purposes, an overlay rheology chart is provided in Figure 68 for the 1K-Flex, 2K-Flex, and Betamate systems.

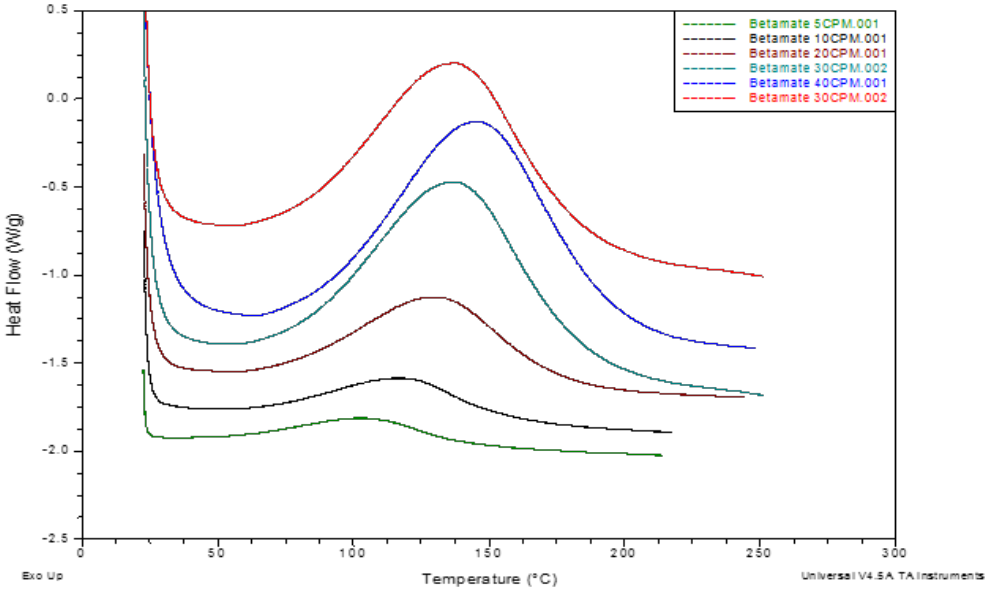

Figure 67. DSC thermograms of Betamate as a function of ramp rate.

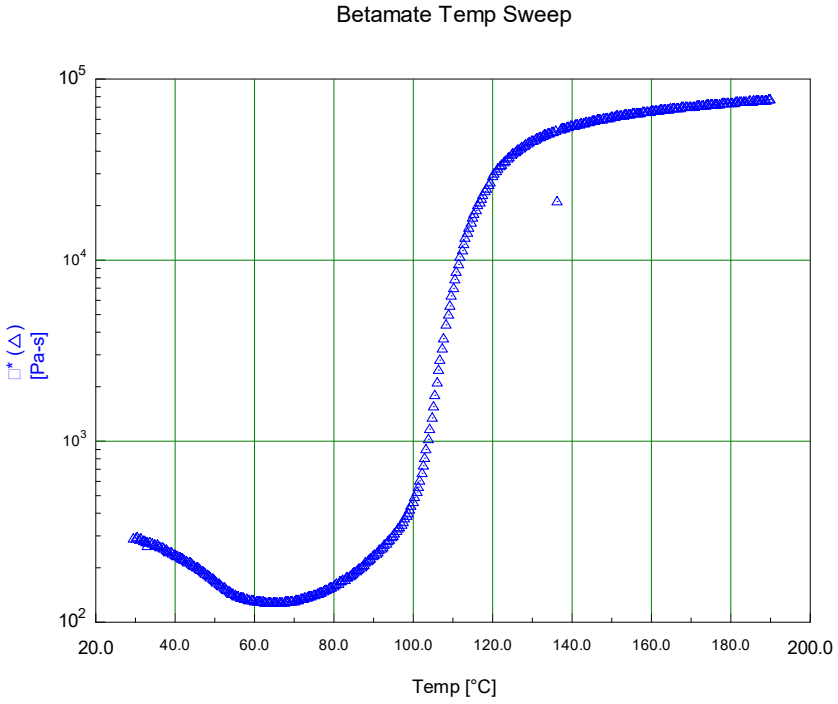

Figure 68. Betamate parallel plate viscosity profile.

Betamate 73326M Thermal Mechanical Analysis (TMA)

A plot of the dimension change versus temperature collected by TMA for Betamate cured for 20 minutes at 190°C is provided in Figure 69. The Tg determined by TMA is slightly higher than the Tg detected by DSC in Figure 64.

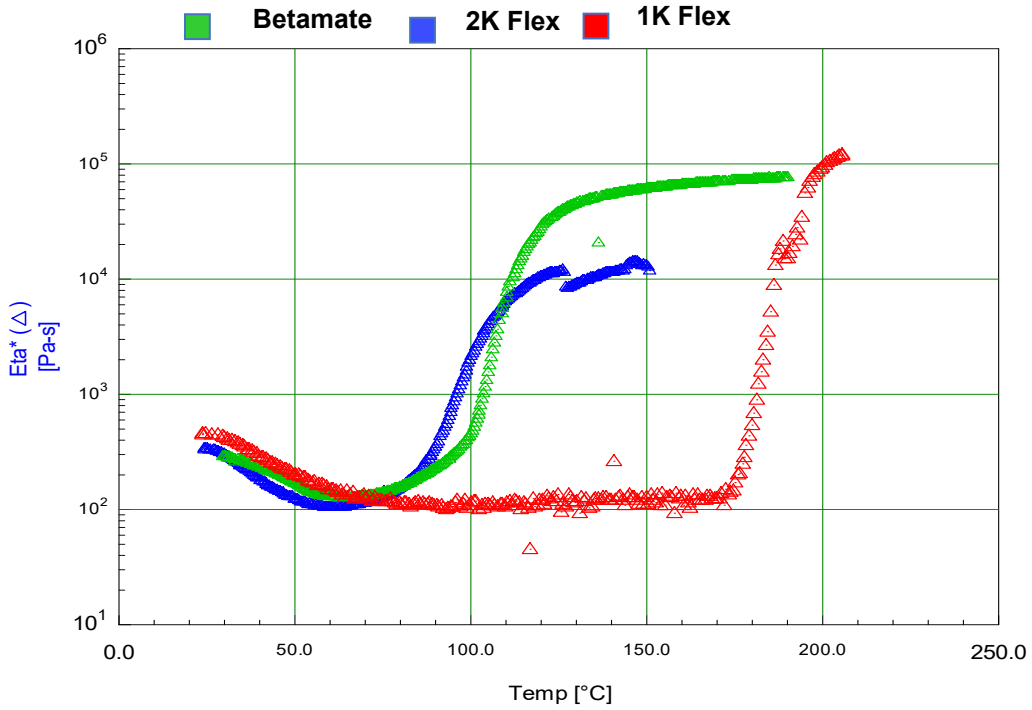

Figure 69. Viscosity overlay chart for 1K-Flex (red), 2K-Flex (blue), and Betamate (green).

Betamate 73326M Dynamic Mechanical Analysis (DMA)

DMA was conducted on Betamate cured at room temperate for 72 hours and after full cure of 190°C for 20 minutes. The storage modulus is greater for the heat-cured system, Figure 70. The glass transition temperature, defined as the peak maximum of tan delta, is also greater in the heat-cured system, shown in Figure 71.

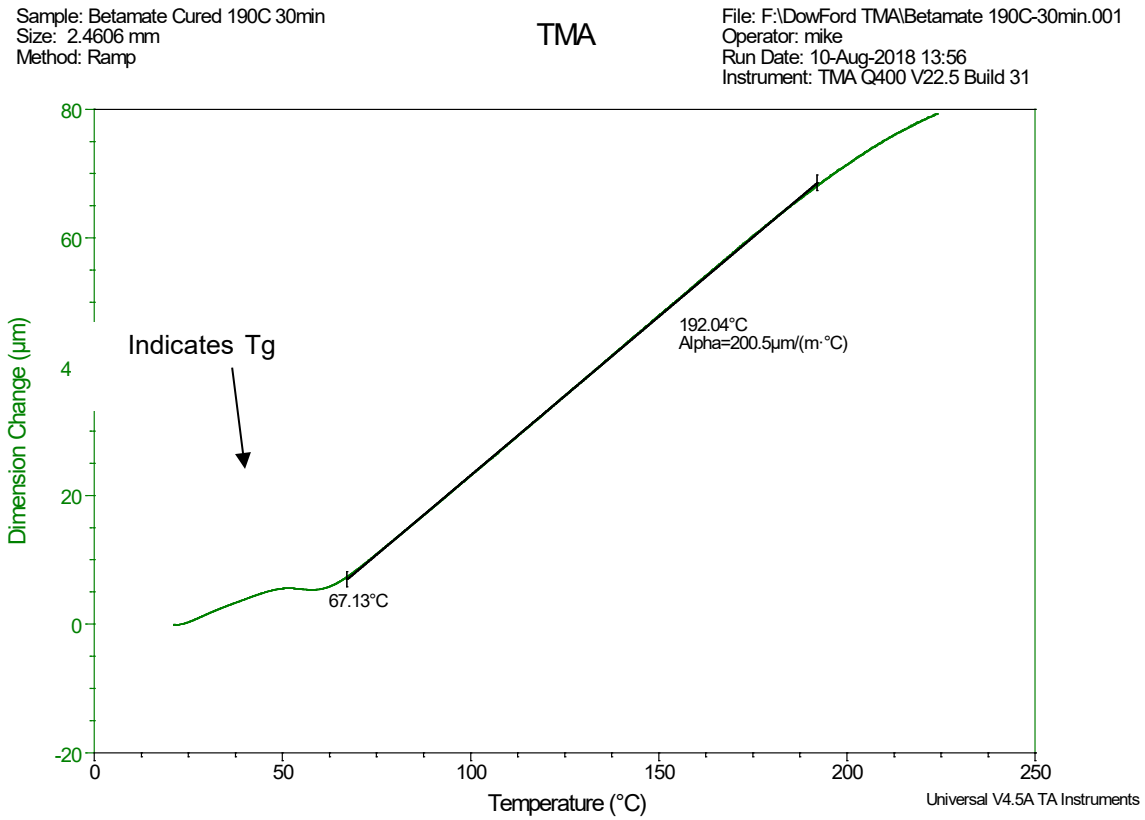

Figure 70. Betamate TMA thermogram.

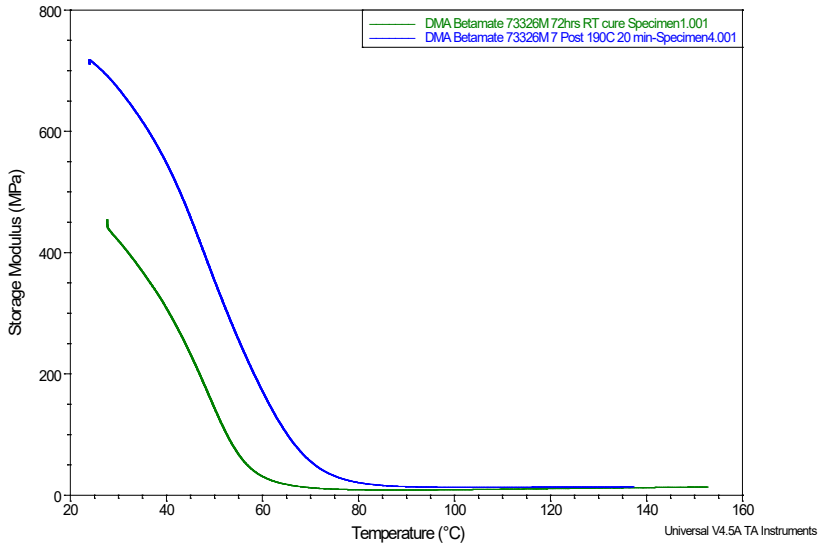

Figure 71. DMA thermogram of Betamate cured at RT and 190°C.

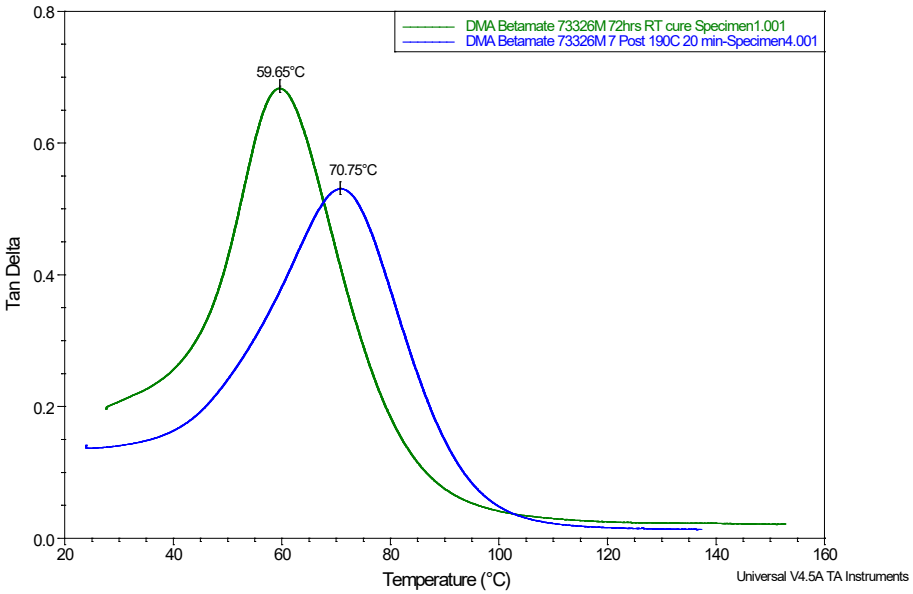

Figure 72. Betamate tan delta cured at RT (green) and 190°C (blue).

4.4.4.1.2 Tensile Properties of Adhesives

Tensile coupons were fabricated by troweling the Dow 1K-Flex, Dow 2K Flex, and Betamate 73326M viscous adhesives into a silicone mold having the requisite ASTM D638 Type 1 tensile coupons, then heated per each adhesive's cure schedule. The resultant coupons were imperfect, having surface flaws as wells as internal voids.

Tensile properties were evaluated on a United Test Systems model SFM20 electromechanical

screw drive machine. Specimen elongation was measured with an optical (laser) extensometer. Tests were conducted in general compliance with ASTM D638. Tensile strengths are reported in Figure 73, tensile modulus in Figure 74, and failure strain in Figure 75.

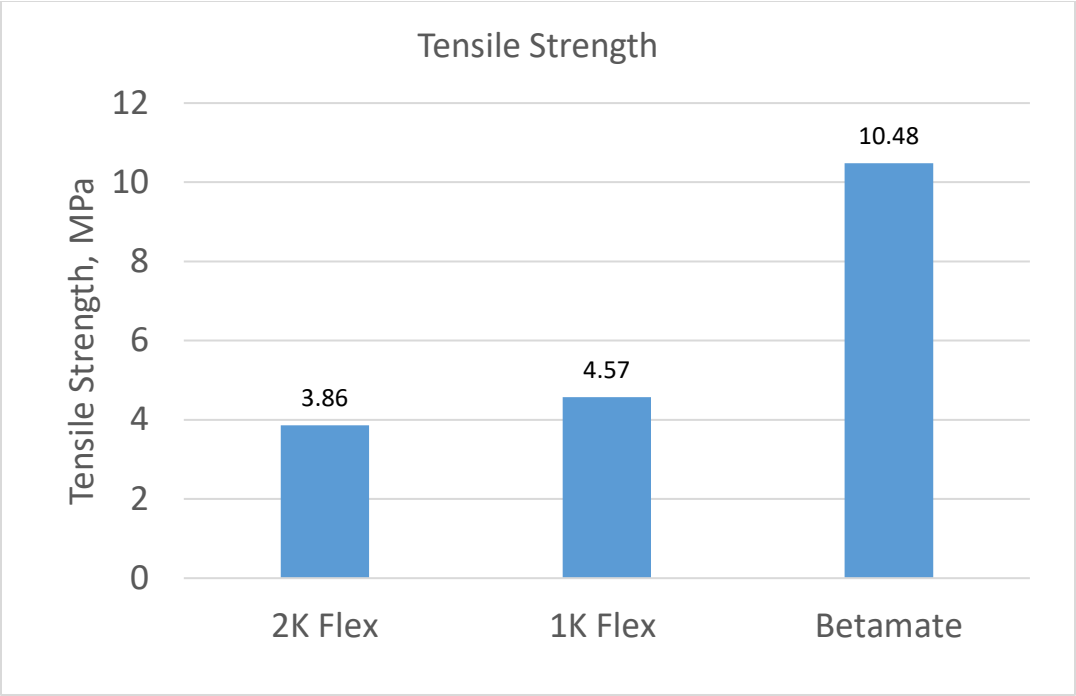

Figure 73. Adhesive tensile strength.

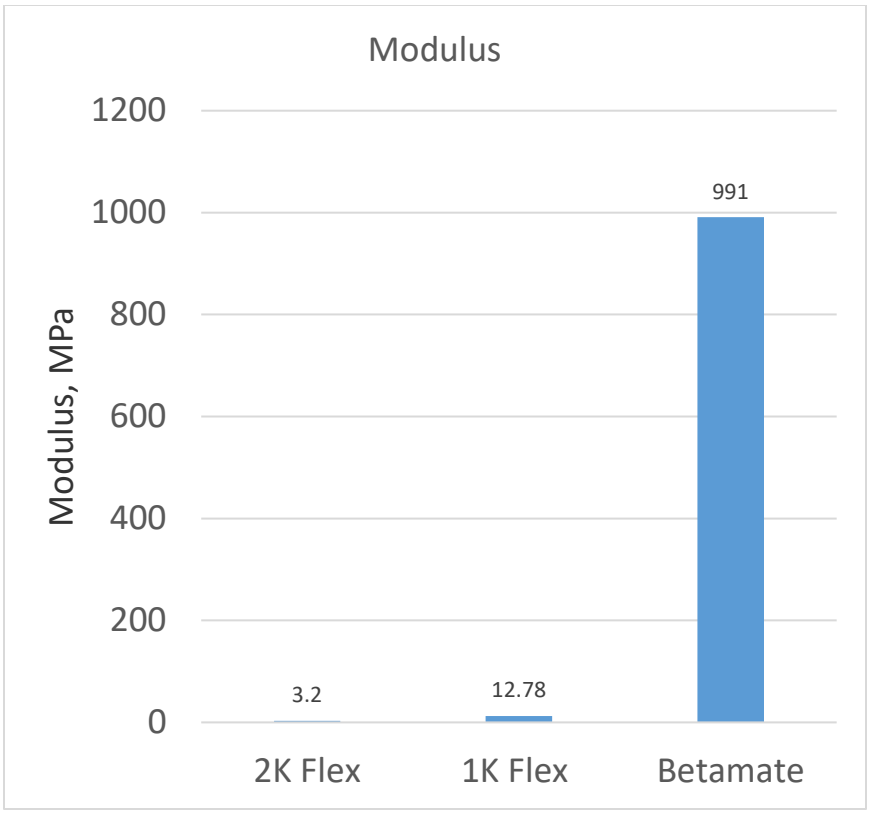

Figure 74. Adhesive tensile modulus.

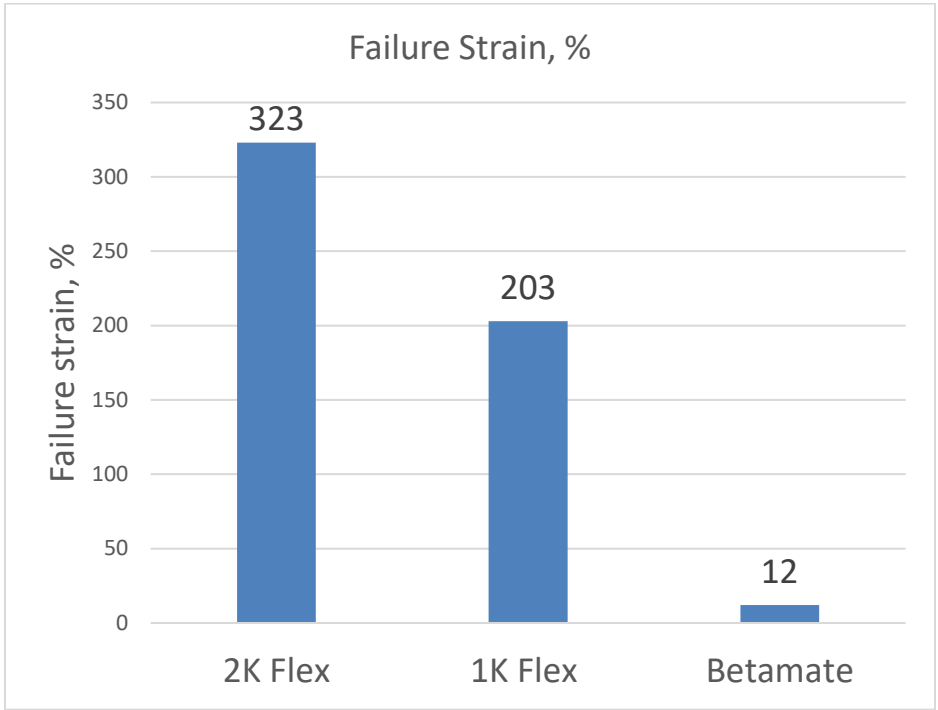

Figure 75. Adhesive failure strain.

4.4.4.2 Results: Composite Characterization

To evaluate the effect of the IMR on mechanical properties, unidirectional carbon fiber/Vorafuse™ epoxy composites were tested in the 0° and 90° directions. Tensile and flexural properties were measured on 8-ply laminates, while the short beam shear test used a 16-ply laminate. All four of the 8-ply panels exhibited some degree of warpage parallel and/or transverse to the fiber direction, Figure 76.

Figure 76. Edge view of panel LMG-061617-02, warpage approximately 8 mm.

To the extent possible, samples for testing were harvested away from the warpage. The panels were received with aluminum foil release plies on both surfaces. The composites containing the IMR released the foil cleanly. All panels without IMR retained strips of the foil embedded in their surfaces, Figure 77, along what appear to have been creases in the foil.

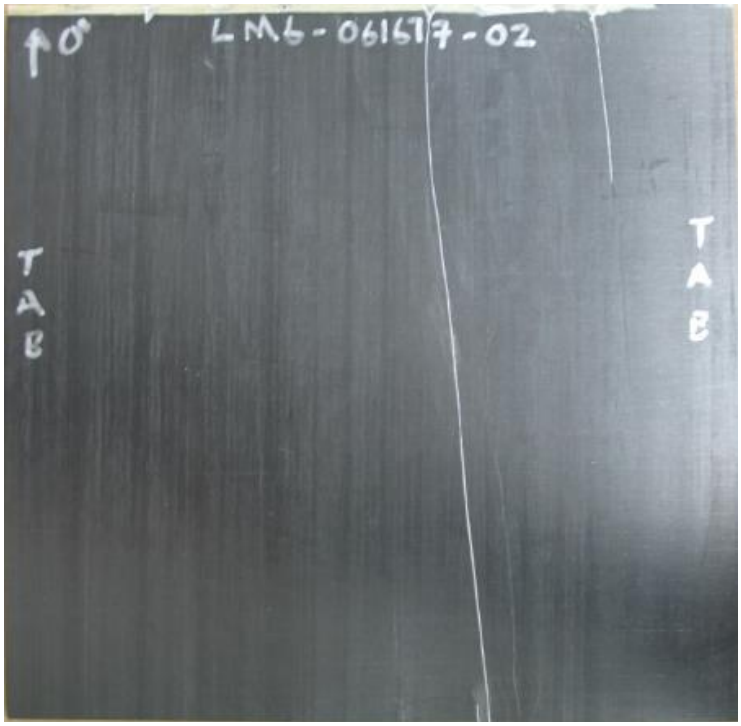

Figure 77. Aluminum foil embedded in the surface of panel LMG-061617-02.

It was unavoidable to completely exclude the strips from test samples, and they did cross the failure paths in the 90° tensile specimens. The packing slip enclosed with the samples listed the 8-ply plaques as having substantially the same part weight (226 g to 234.7 g). However, the average measured thickness of the plaques without IMR (1.58 mm, 1.53 mm) was greater than those with IMR (1.31 mm, 1.32 mm).

The 0° tensile strength and modulus of the composites are shown in Figures 78 and 79. The composite with IMR had increases of +37% and +21% in strength and modulus, respectively. Photographs of the failed specimens are shown in Figure 80.

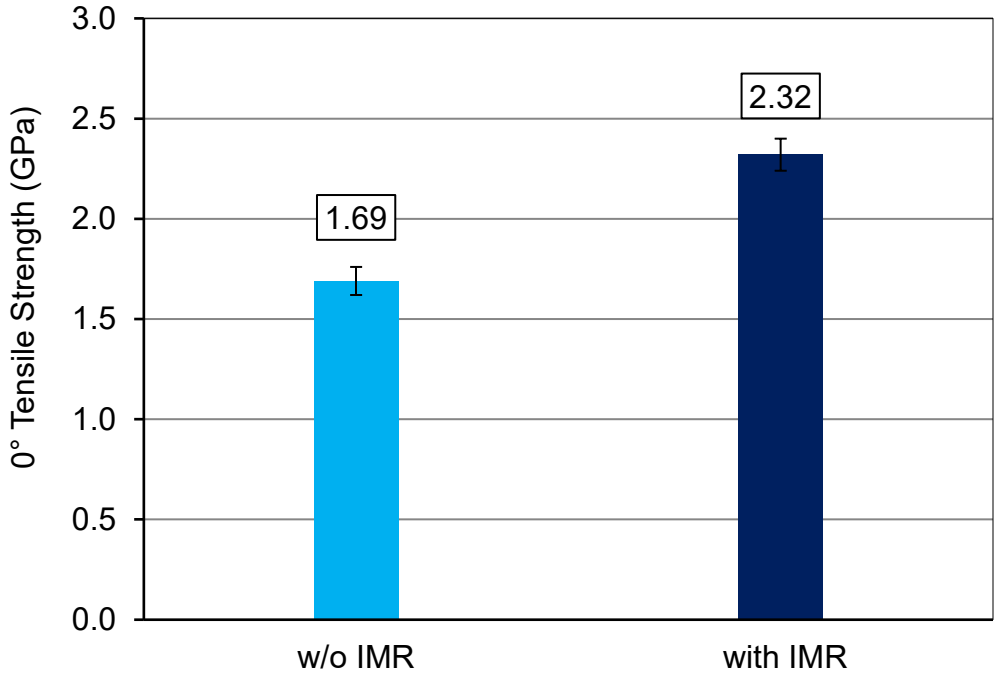

Figure 78. The 0° tensile strength of carbon fiber/Vorafuse™ composites.

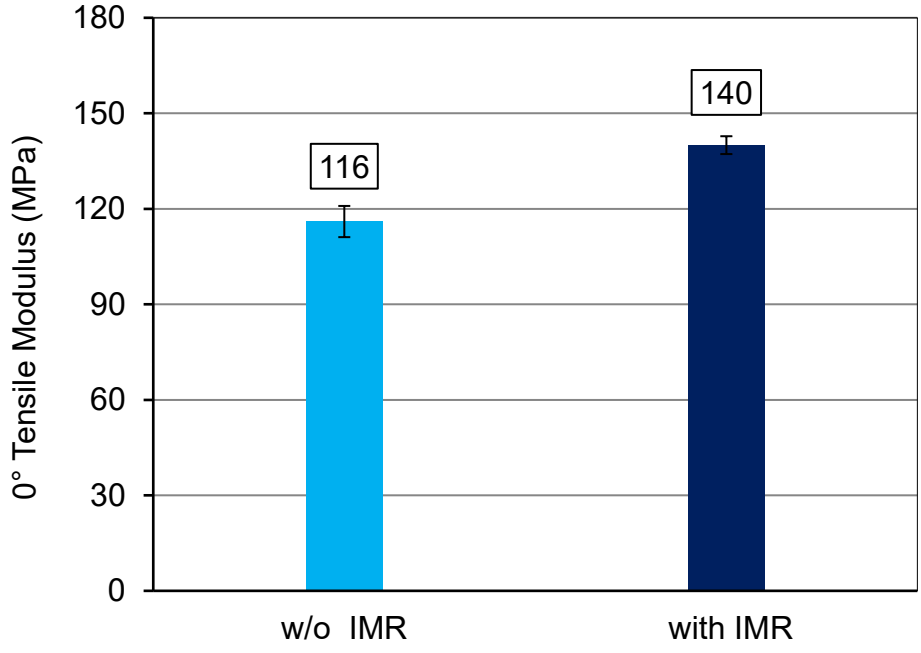

Figure 79. The 0° tensile modulus of carbon fiber/Vorafuse™ composites.

Figure 80. Composite failure modes, 0° tension.

The 90° tensile strength and modulus of the composites are show in Figures 81.. The composite with IMR had changes of -7.5% and +1.1% in strength and modulus, respectively.

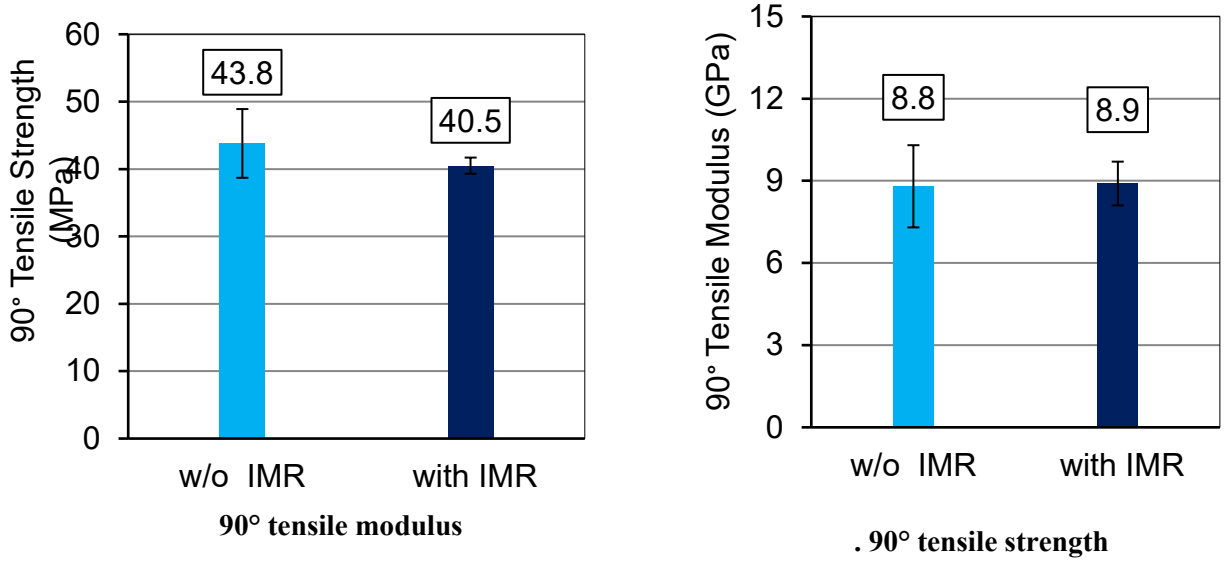

Figure 81 . The 90° tensile modulus and strength of carbon fiber / Vorafuse™ composites

.The 90° tensile specimens without IMR exhibited lateral failure. Three of the five specimens' failure areas were at the tab; the other two failed in the gage section (per ASTM D3039). All failures of the composite with IMR occurred inside the tabbed region, very close to the gage section. Figure 82 shows the specimens post-testing.

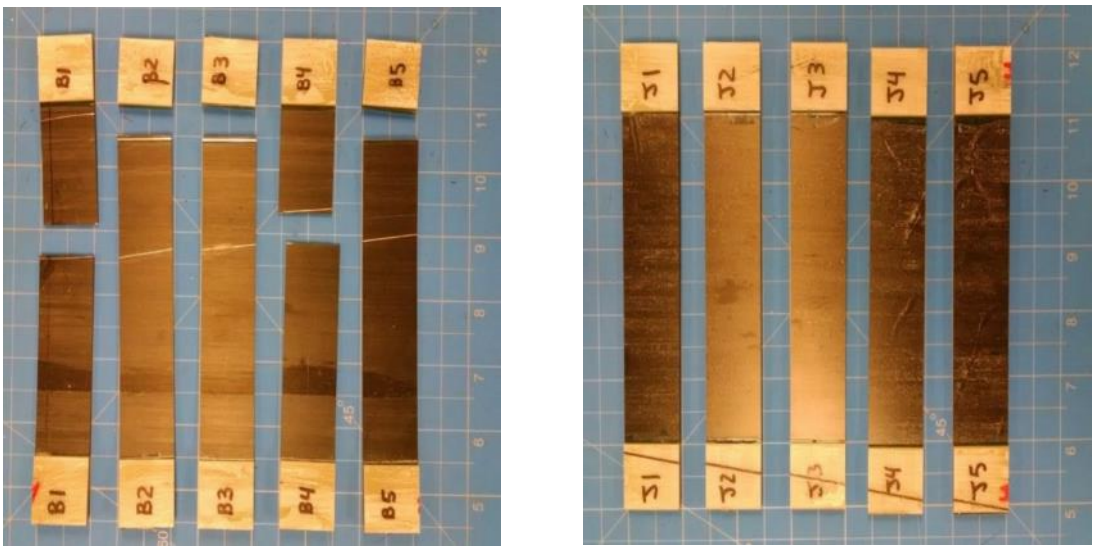

No IMR With IMR

Figure 82. Composite failure modes, 90° tension.

Polished cross sections of the trimmings from the 90° tension specimens revealed no preexisting defects in the composite with IMR, Figure 83.

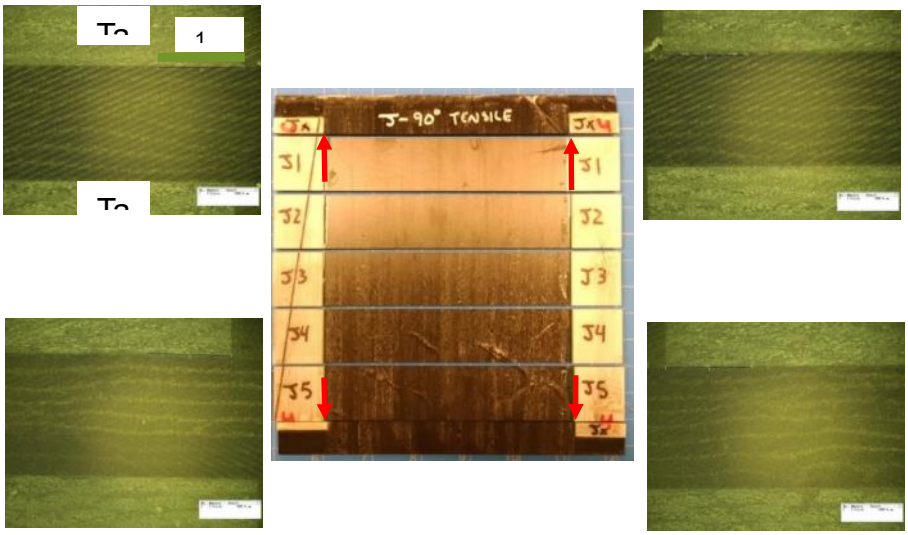

Figure 83. Composite failure modes, 90° tension, edge view.

The 0° flexural strength and modulus of the composites are show in Figures 84 and 85. The composite with IMR had changes of +25% and +15% in strength and modulus, respectively.

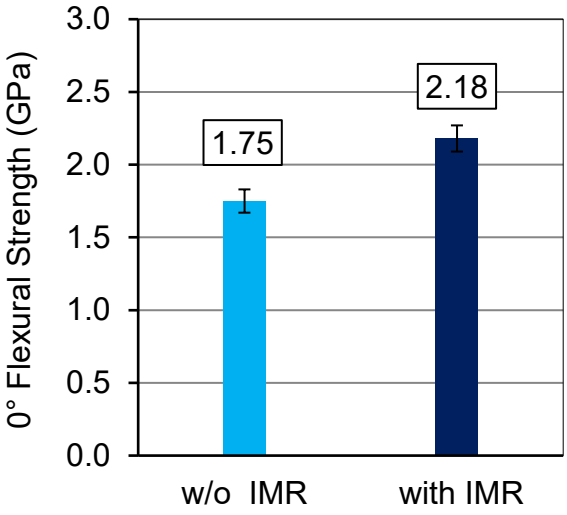

Figure 85. The 0° flexural strength of carbon fibe /Vorafuse™ composites.

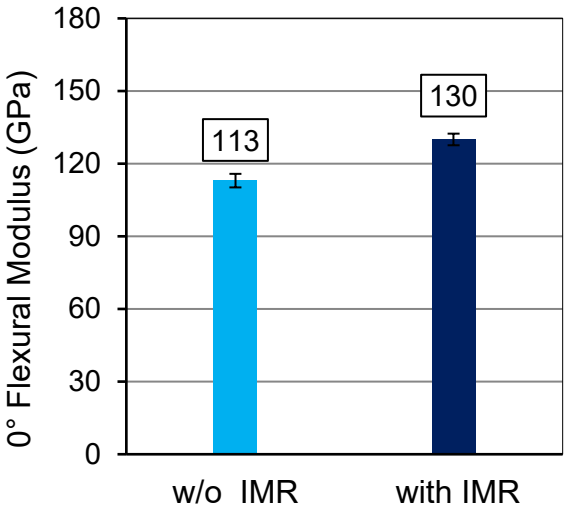

Figure 84. The 0° flexural modulus of carbon fiber/Vorafuse™ composites.

The 0° flexural specimens failed in both the axial and transverse directions. Figure 86 shows the specimens post-testing. Note: The silver lines on the specimens are identification aids, not embedded aluminum foil.

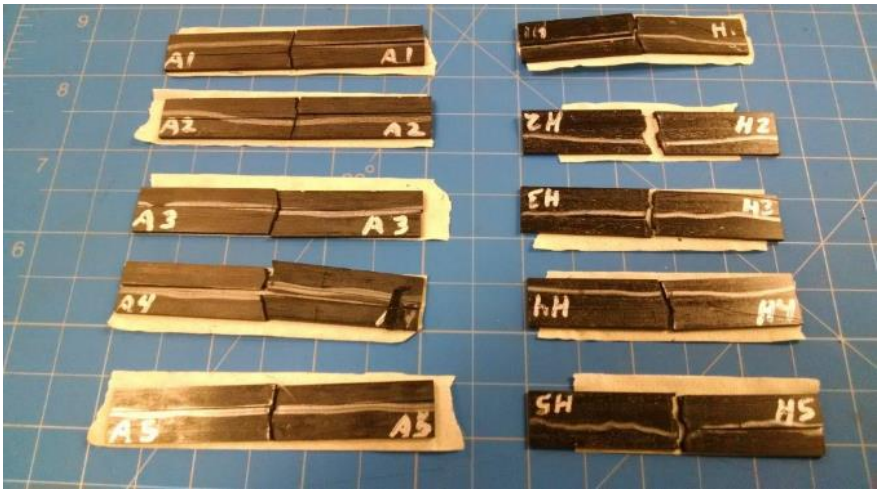

Figure 86. Composite failure modes, 0° flexure.

The 90° flexural strength and modulus of the composites are shown in Figures 45 and 46. The composite with IMR had changes of -22% and +16% in strength and modulus, respectively.

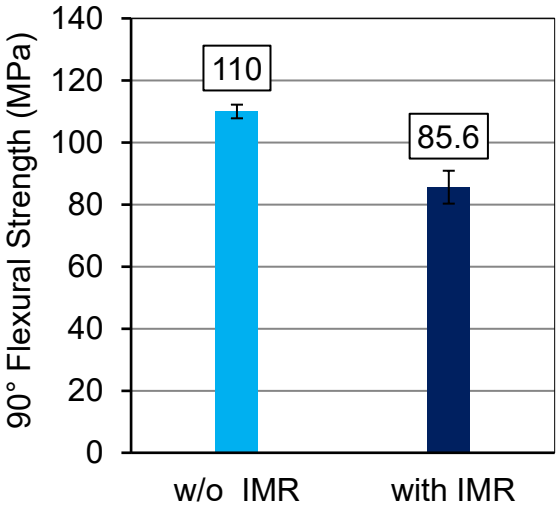

Figure 88. The 90° flexural strength of carbon fiber/Vorafuse™ composites.

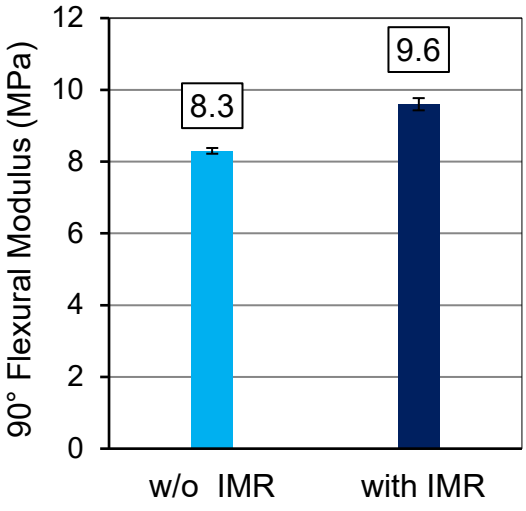

Figure 87.The 90° flexural modulus of carbon fiber/Vorafuse™ composites.

The 90° flexural specimens all failed in the transverse direction. Figure 89 shows the specimens post-testing.

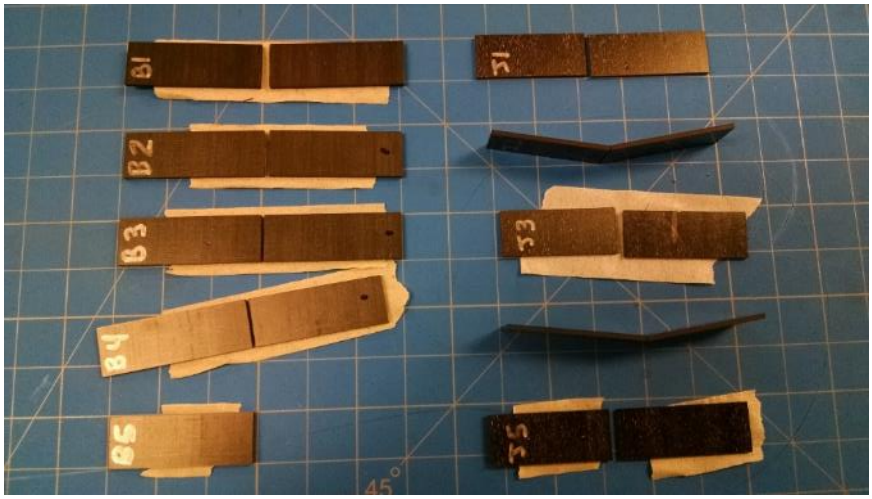

Figure 89 . Composite failure modes, 90° flexure.

SEM examination was performed on the failure surfaces of the 0° and 90° flexure specimens, Figures 90 and 91, respectively.

No IMR With IMR

Figure 90. Composite failure surfaces, 0° flexure.

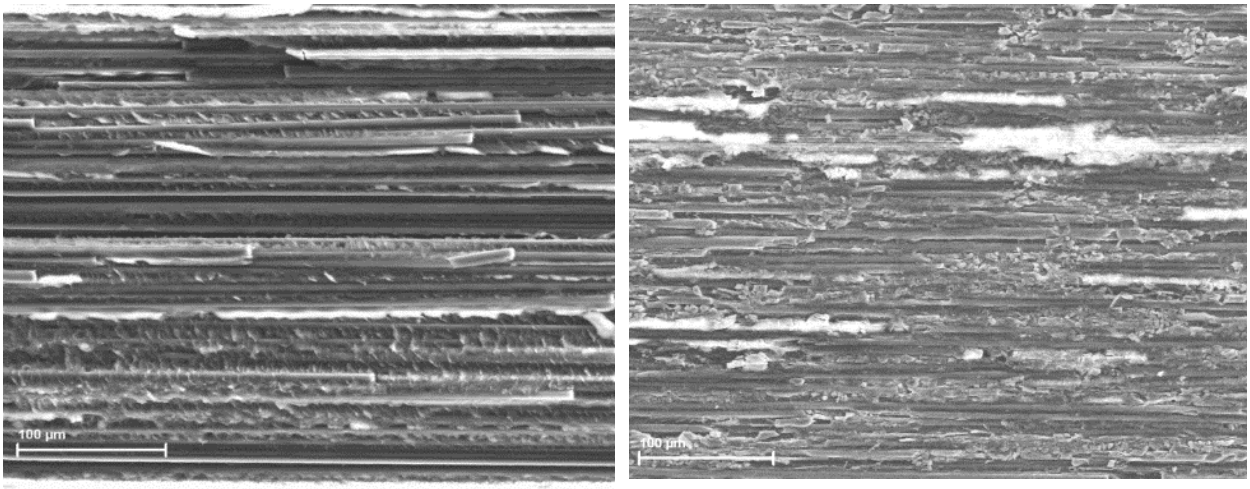

No IMR With IMR

Figure 91 . Composite failure surfaces, 90° flexure.

The apparent interlaminar shear strength of the composites is shown in Figure 92. All failures were interlaminar, and the composite with IMR had a decrease in ILSS of 6.4%. An equal-variance, two-tailed t-test yields a p-value of 0.002.

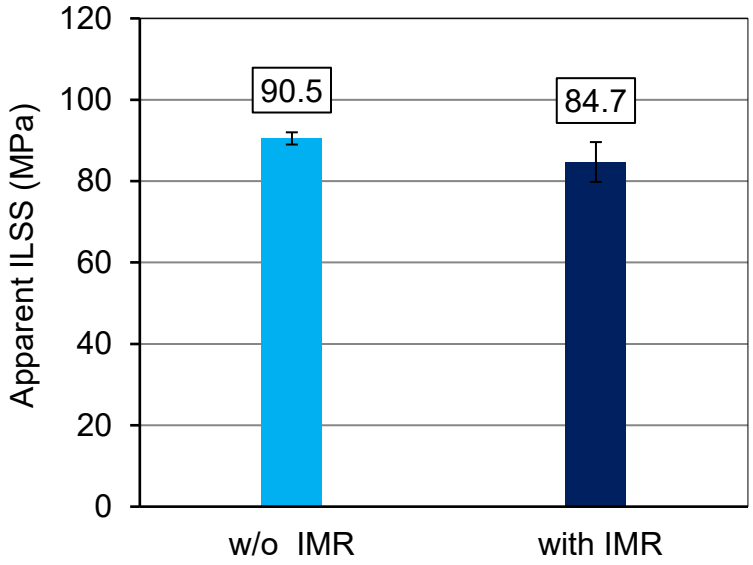

Figure 92. The apparent ILSS of carbon fiber/Vorafuse™ composites.

4.4.4.3 Results: Adhesive Bonding

4.4.4.3.1 Wettability

Water contact angles were measured to determine if the IMR changed the wettability of the resin. Neat resin plaques as well as unidirectional composites made with and without IMR were investigated in their as-received condition. The neat resin without IMR was the only material with a contact angle below 90°. Its contact angle increased from 63.0° to 102.4° when the IMR was added. The composite surfaces also increased in water contact angle, rising from 97.0° to 104.4° when the resin contained the IMR, Figure 93.

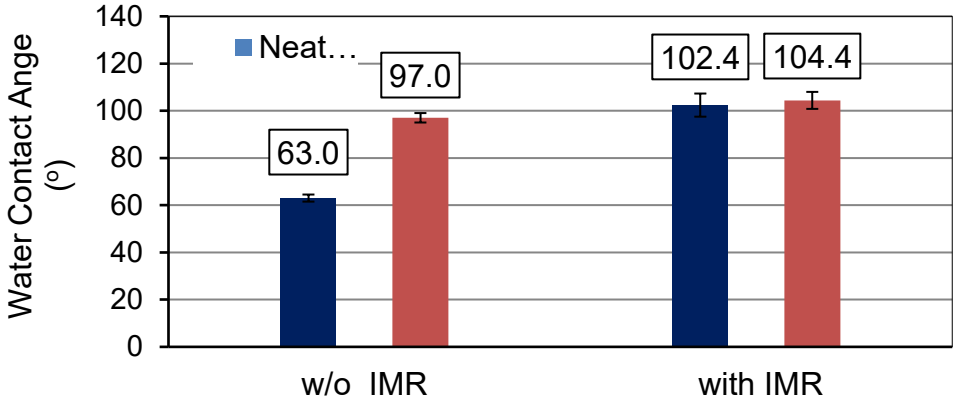

Figure 93. Water contact angles of neat resin plaques and carbon fiber/Vorafuse™ composites.

4.4.4.3.2 PATTI Adhesion Testing on Aluminum

PATTI adhesion testing was performed on aluminum sheet stock supplied by Ford and composites supplied by Dow. The aluminum sheet was tested in the as-received condition as well as after IPA cleaning to remove the oily surface film. The composites were carbon fiber-reinforced Vorafuse™ in an 8 ply, [±45]2s layup, with and without IMR. After the composite test specimens were cut from the larger plates, they were IPA cleaned immediately prior to bonding the pull-off stub. Betamate 73326M/73327M, 1K-Flex and 2K-Flex were the adhesives tested. After testing, the substrate was examined to determine the failure mode of the adhesive joint. The type (cohesive or adhesive) and locus of failure (substrate or adhesive) were noted for each specimen.

Testing on the aluminum substrate examined the effect of IPA cleaning on the development of the bond strength and changes in the failure mode. The Betamate specimens were cured for 30 min at 190 °C. The pull-off tensile strength increased with IPA-cleaning, and the failure mode shifted to purely cohesive failure in the Betamate. The 1K-Flex specimens were cured for 30 min at 190 °C. The pull-off tensile strength did not increase with IPA-cleaning, and the failure mode was cohesive in the 1K-flex for both the as-received and IPA-cleaned conditions. This indicates that the 1K-Flex can bond to an oily surface. The pull-off tensile strength of the 2K-Flex specimens increased with IPA cleaning for both cure cycles studied, 8 hr at 60 °C and 10 min at 190 °C. The high-heat cure cycle resulted in higher pull-off tensile strengths. The IPA-cleaned, high-heat condition had the highest pull-off tensile strength and exhibited cohesive failure in the adhesive. A summary comparison of the PATTI results is shown in Figure 94. Detailed results are given in Figures 95 to 98 and Tables 5 to 7.

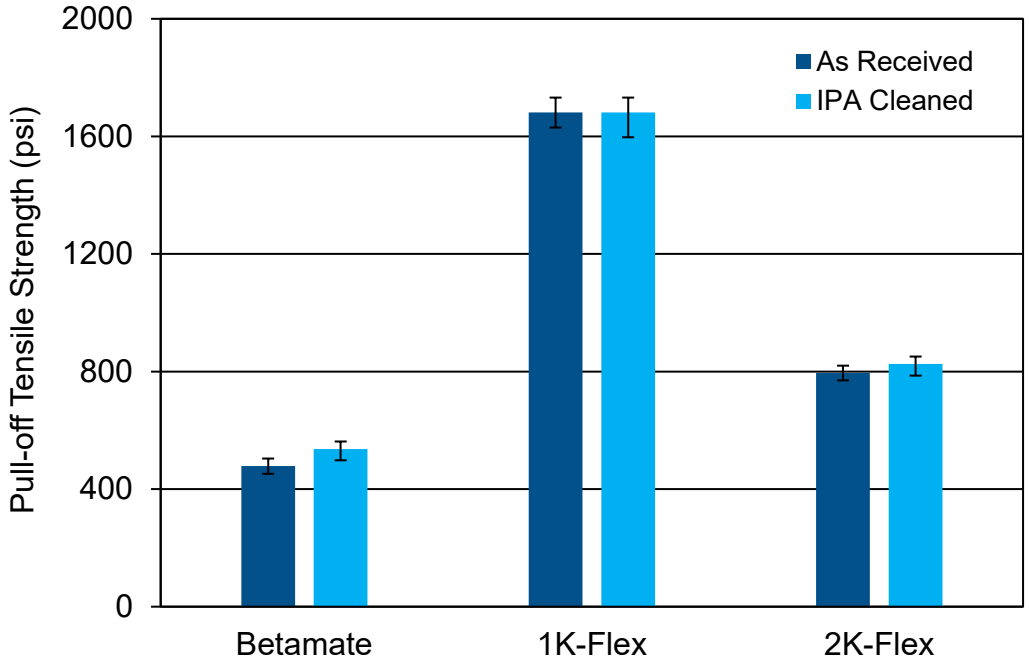

Figure 94. Pull-off tensile strength of the adhesives on aluminum after curing at 190 °C.

Table 5. Pull-off tensile strength of Betamate 73326M/73327M on aluminum.

Material	Pull-off Tensile Strength (psi)	Failure Mode(s)
As-Received 30 min, 190°C	478 ± 26 (n=4)	Cohesive failure in the Betamate Adhesive failure at the aluminum
IPA Cleaned 30 min, 190°C	536 ± 38 (n=4)	Cohesive failure in the Betamate

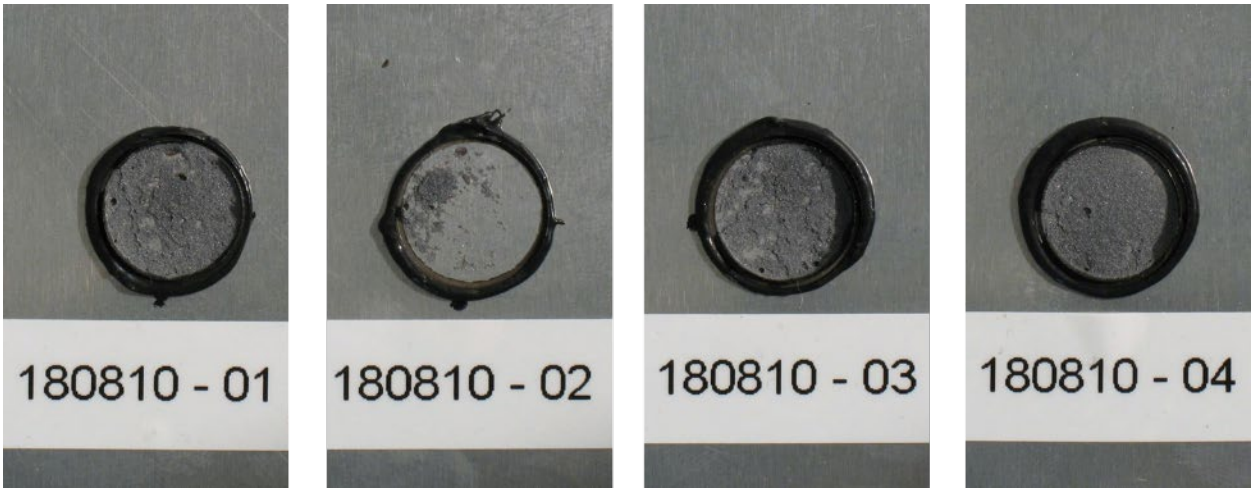

Figure 95. Failure surfaces of as-received aluminum/Betamate PATTI specimens.

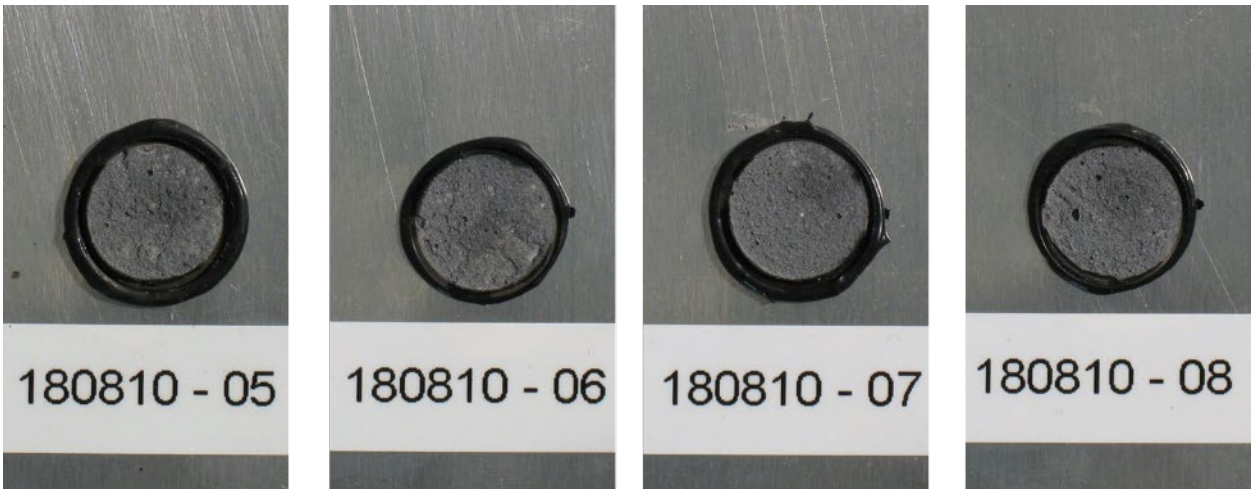

Figure 96. Failure surfaces of IPA-cleaned aluminum/Betamate PATTI specimens.

Table 6. Pull-off tensile strength of 1K-Flex on aluminum.

Material	Pull-off Tensile Strength (psi)	Failure Mode(s)
As-Received 20 min, 190°C	1681 ± 51 (n=4)	Cohesive failure in the 1K-Flex
IPA Cleaned 20 min, 190°C	1681 ± 84 (n=4)	Cohesive failure in the 1K-Flex

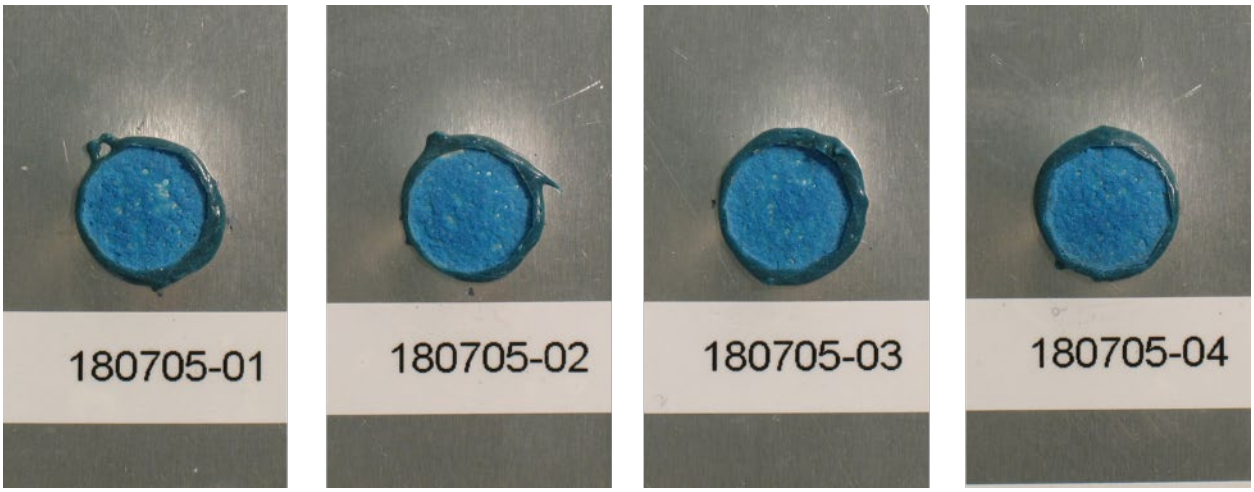

Figure 97. Failure surfaces of as-received aluminum/1K-Flex PATTI specimens.

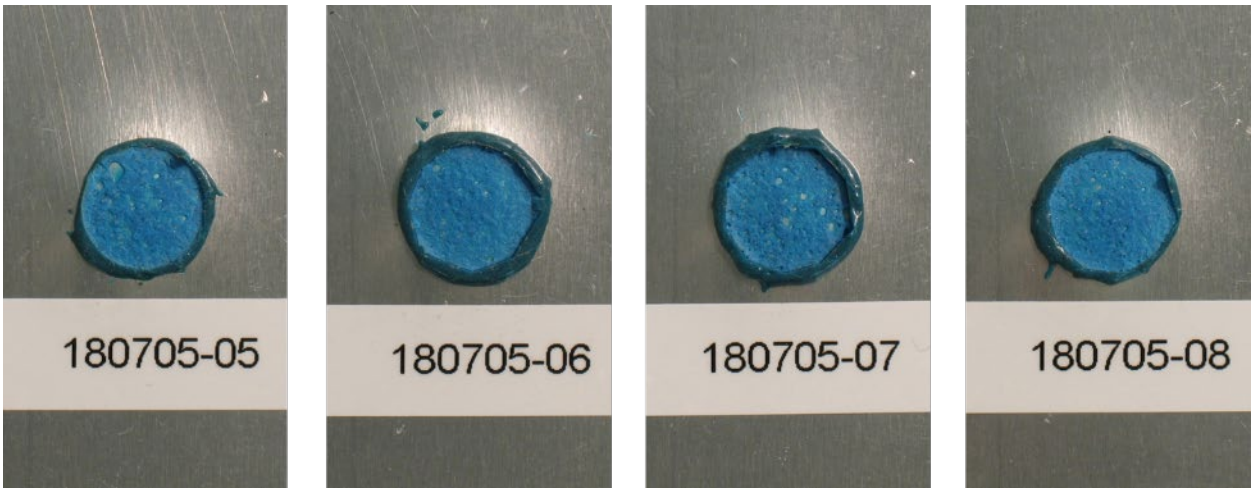

Figure 98. Failure surfaces of IPA-cleaned aluminum/1K-Flex PATTI specimens.

Table 7. Pull-off tensile strength of 2K-Flex on aluminum.

Material	Pull-off Tensile Strength (psi)	Failure Mode(s)
As Received 8 hr, 60 °C	685 ± 44 (n=4)	Adhesive failure at the aluminum Cohesive failure in the 2K-Flex (minor)
As Received 8 hr, 60 °C 10 min, 190 °C.	795 ± 25 (n=4)	Cohesive failure in the 2K-Flex Adhesive failure at the aluminum (minor)
IPA-Cleaned 8 hr, 60 °C	792 ± 47 (n=4)	Adhesive failure at the aluminum Cohesive failure in the 2K-Flex (minor)
IPA Cleaned 8 hr, 60°C 10 min, 190 °C	826 ± 40 (n=4)	Cohesive failure in the 2K-Flex

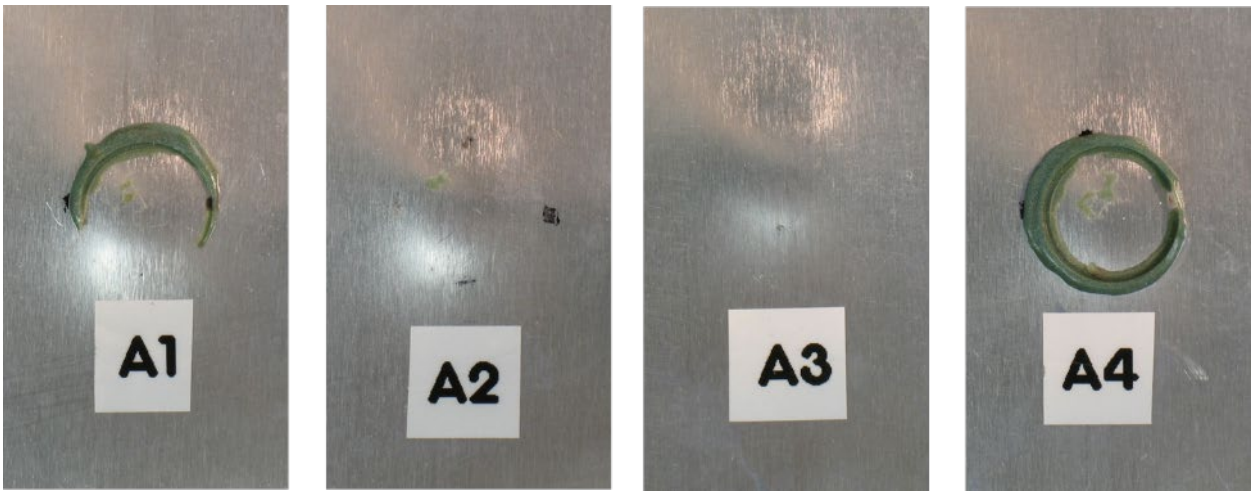

Figure 99. Failure surfaces of as-received aluminum/2K-Flex PATTI specimens (8 hr, 60 °C)

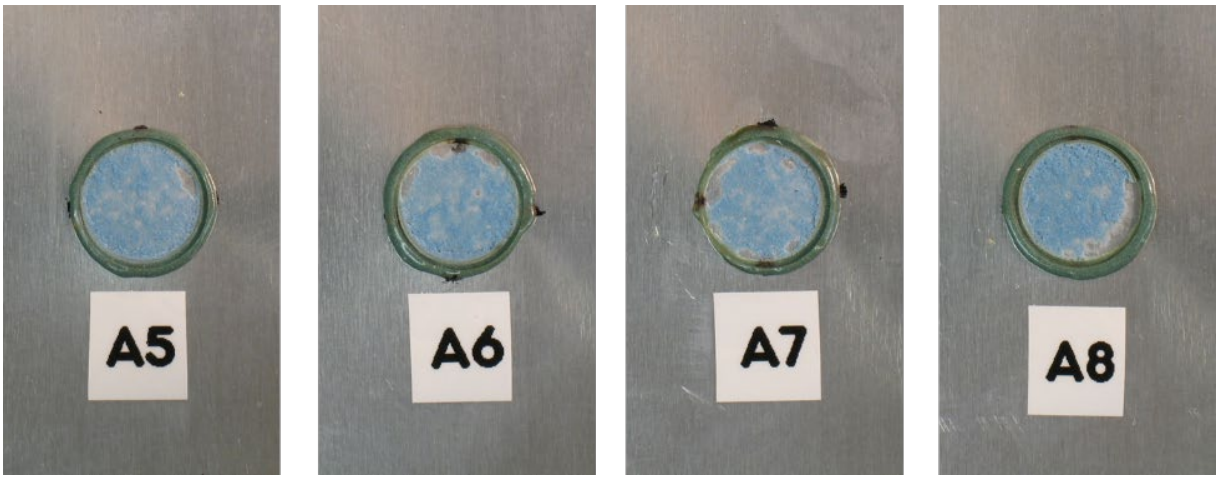

Figure 100. Failure surfaces of as-received aluminum/2K-Flex PATTI specimens (8 hr, 60°C, 10 min, 190 °C).

Figure 101. Failure surfaces of IPA-cleaned aluminum/2K-Flex PATTI specimens (8 hr, 60°C).

Figure 102. Failure surfaces of IPA-cleaned aluminum/2K-Flex PATTI specimens (8 hr, 60 °C, 10 min, 190 °C).

4.4.4.3.3. PATTI. Adhesion Testing on Carbon Fiber-Reinforced Vorafuse™ Composites

Testing on the composites was performed to examine the effect of the IMR on the development of the bond strength and changes in the failure mode. After the cure cycles at 190°C, closed sub-surface delaminations were observed in the composites. They occurred with greater frequency in the composites with IMR, Figure 103

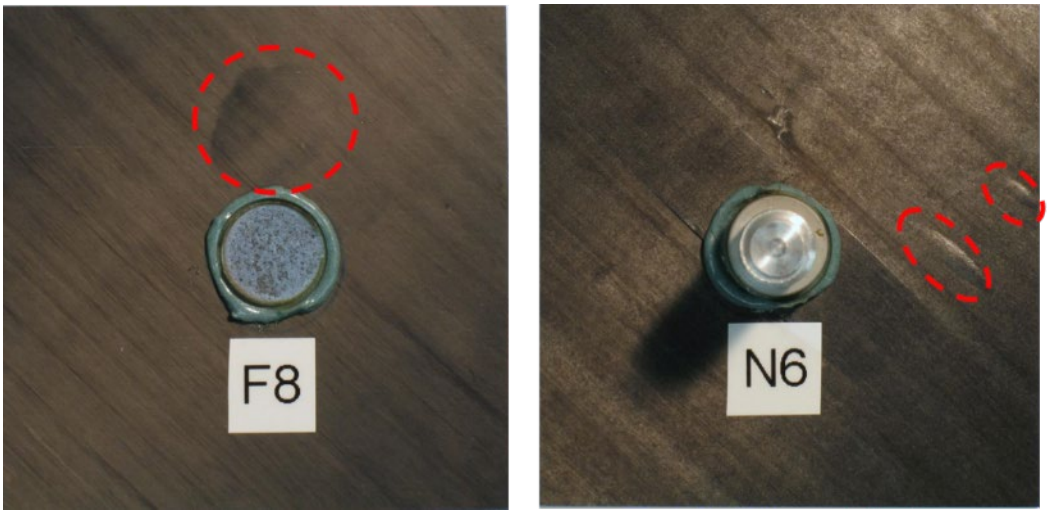

Figure 103. Delaminations enclosed by red dashed lines, F8 = no IMR, N6 = with IMR, adhesive = 2K-Flex.

The Betamate 73326M/73327M test specimens were cured at 190°C for 30 min. The no IMR specimens failed cohesively inside the bond line while those with IMR failed at and below the composite surface. The pull-off tensile strength of the composite with IMR dropped drastically due to failure of the composite surface and delaminations inside the composite. Table 8 and Figures 106 and 107 have detailed results.

The 1K-Flex test specimens were cured at 190°C for 20 min. The pull-off tensile strength was high enough to initiate delamination inside the no-IMR composite. For the composite with IMR, the pull-off tensile strength dropped drastically due to increased delamination inside the composite. Table 9 and Figures 108 & 109 have detailed results.

The pull-off tensile strength of the 2K-Flex specimens cured at 60°C for 8 hr was affected by the presence of the IMR; there was a 38% reduction in the pull-off tensile strength, and the failure locus shifted to the composite surface. The addition of a high-heat cycle had two interesting effects. In the case of the composite without IMR, the pull-off tensile strength dropped and the failure shifted to cohesive failure of the 2K-Flex, Figure 105. This strength drop was also seen in the tensile testing of the neat 2K-Flex. In the case of the composite with IMR, the 8 hr, 60°C failure locus was the surface of the composites. The high-heat soak did shift the failure locus to the inside of the composite. Perhaps the 2K-flex was able to bond to the surface despite the presence of the IMR. The high-heat cycle was the shortest of all, 10 min, 190°C. Table 10 and Figures 110 to 113 have detailed results.

A comparison of the PATTI test results for the three adhesives cured using the high-heat cycle is shown in Figure 104.

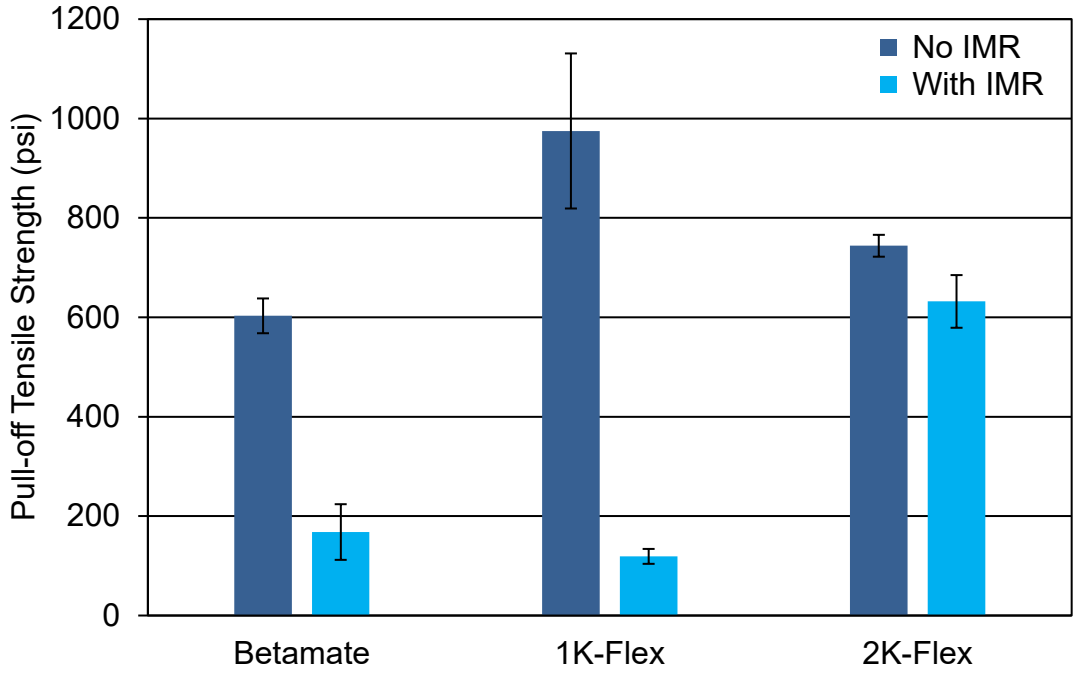

Figure 104. Pull-off tensile strength on carbon fiber reinforced Vorafuse™ composites with and without IMR after curing at 190°C.

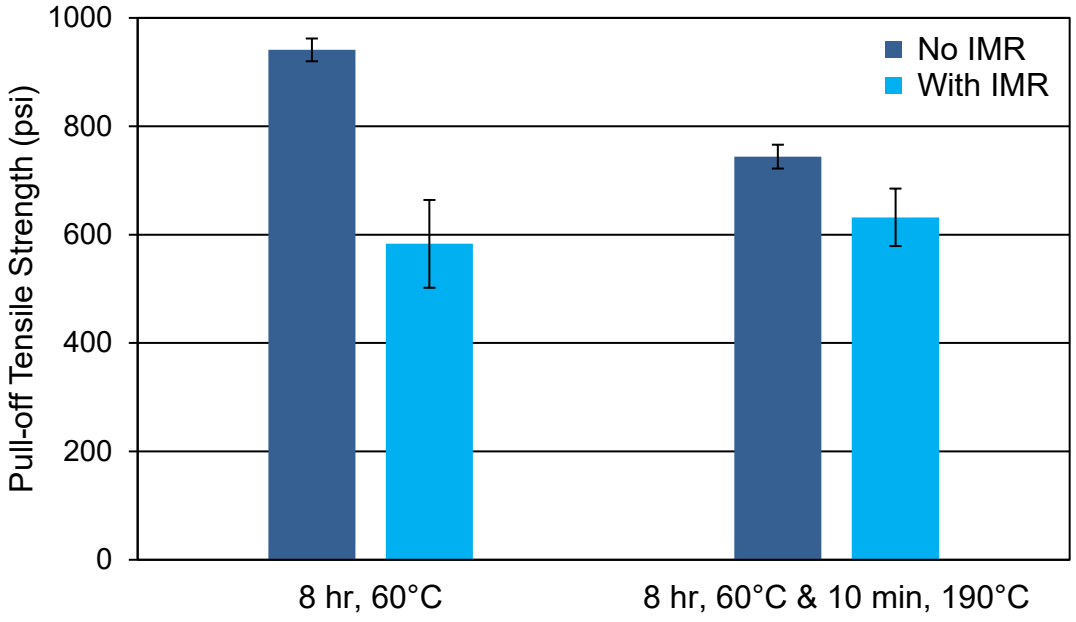

Figure 105. Pull-off tensile strength of 2K-Flex on carbon fiber reinforced Vorafuse™ composites with and without IMR after two different cure cycles.

Table 8. Pull-off tensile strength of Betamate 73326M/73327M on carbon fiber-reinforced Vorafuse™ with and without IMR

Material Cure Cycle	**Pull-off Tensile Strength (psi)**	**Failure Mode(s)**
No IMR 30 min, 190°C	603 ± 34 (n=4)	Cohesive failure in the adhesive
With IMR 30 min, 190°C	168 ± 56 (n=4)	Cohesive failure of the composite surface Delamination in the composite

Figure 106. Failure surfaces of non-IMR composite/Betamate PATTI specimens.

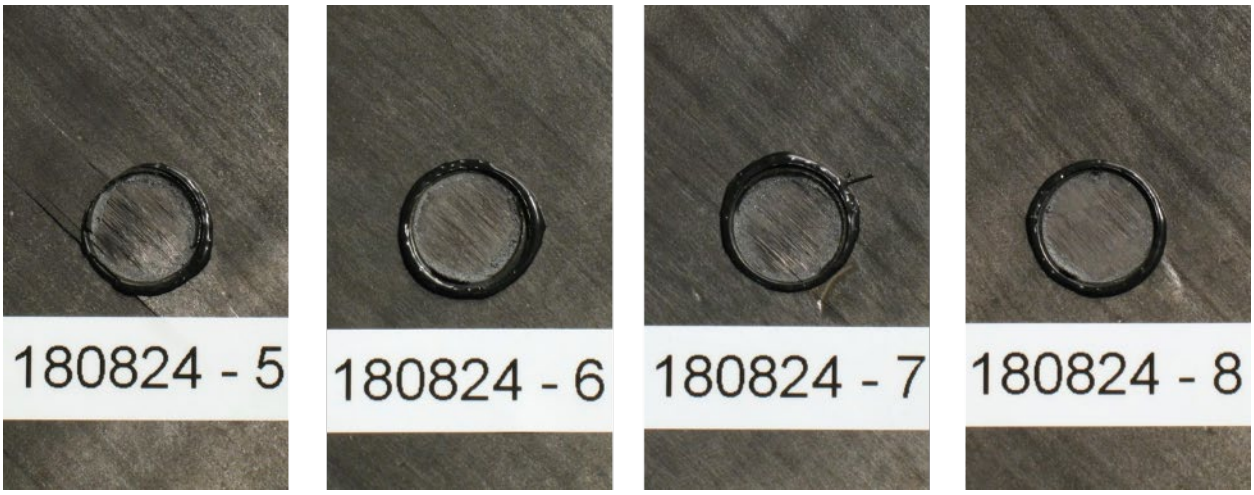

Figure 107. Failure surfaces of composite with IMR/Betamate PATTI specimens.

Table 9. Pull-off tensile strength of 1K-Flex on carbon fiber reinforced Vorafuse™ with and without IMR

Material Cure Cycle	**Pull-off Tensile Strength (psi)**	**Failure Mode(s)**
No IMR 20 min, 190°C	975 ± 156 (n=4)	Cohesive failure in the 1K-Flex (1 & 4) Delamination in the composite (1, 2 & 3)
With IMR 20 min, 190°C	119 ± 15 (n=4)	Delamination in the composite

Figure 108. Failure surfaces of non-IMR composite/1K-Flex PATTI specimens.

Figure 109. Failure surfaces of composite with IMR/1K-Flex PATTI specimens.

Table 10. Pull-off tensile strength of 2K-Flex on carbon fiber reinforced Vorafuse™ with and without IMR.

Material Cure Cycle	**Pull-off Tensile Strength (psi)**	**Failure Mode(s)**
No IMR 8 hr, 60°C	941 ± 21 (n=3)	Adhesive failure at the composite Adhesive failure at the stub Cohesive failure in the 2K-Flex
No IMR 8 hr, 60°C 10 min, 190°C	744 ± 22 (n=4)	Cohesive failure in the 2K-Flex
With IMR 8 hr, 60°C	583 ± 81 (n=4)	Adhesive failure at the composite Cohesive failure of the composite surface
With IMR 8 hr, 60°C 10 min, 190°C	632 ± 53 (n=3)	Delamination of the composite Pull-stub did not detach

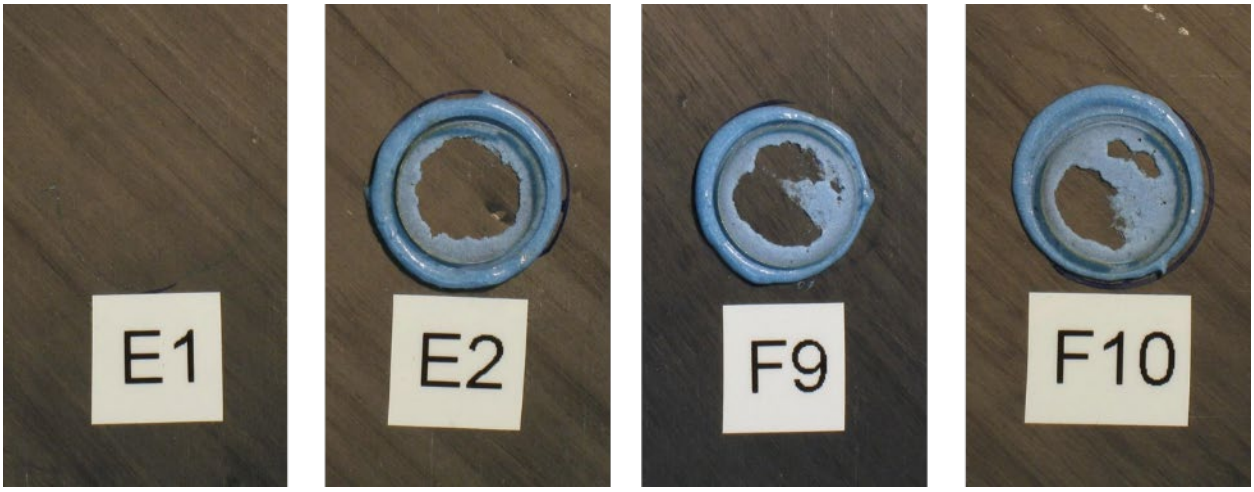

Figure 110. PATTI failure surfaces, no IMR, 2K-Flex (8 hr, 60°C).

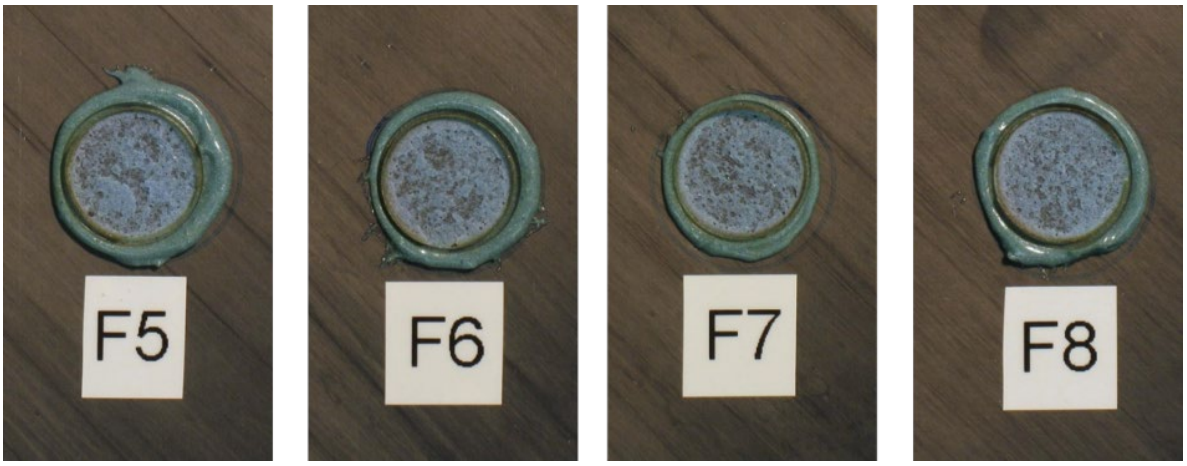

Figure 111. PATTI failure surfaces, no IMR, 2K-Flex (8 hr, 60°C and 10 min, 190°C)

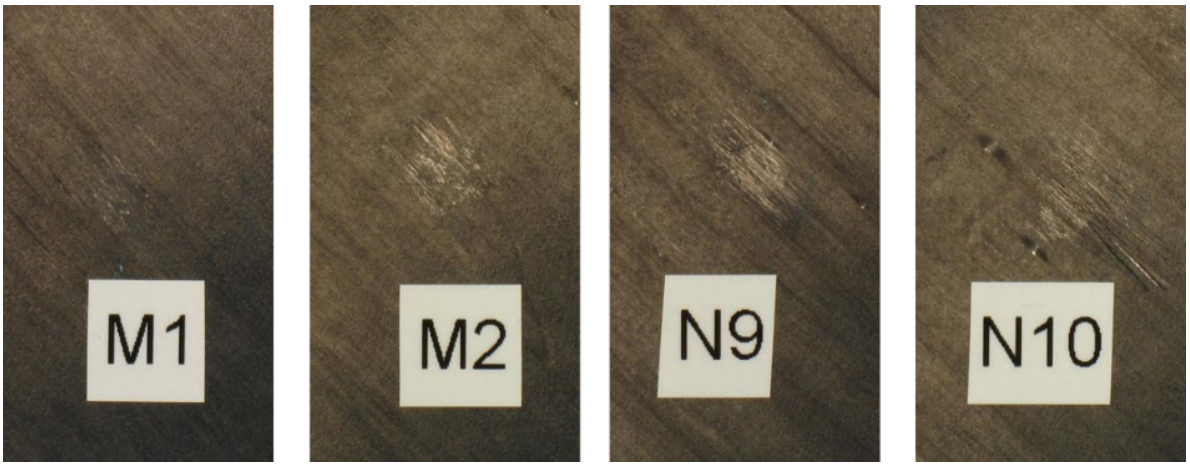

Figure 112. PATTI failure surfaces, with IMR, 2K-Flex (8 hr, 60°C).

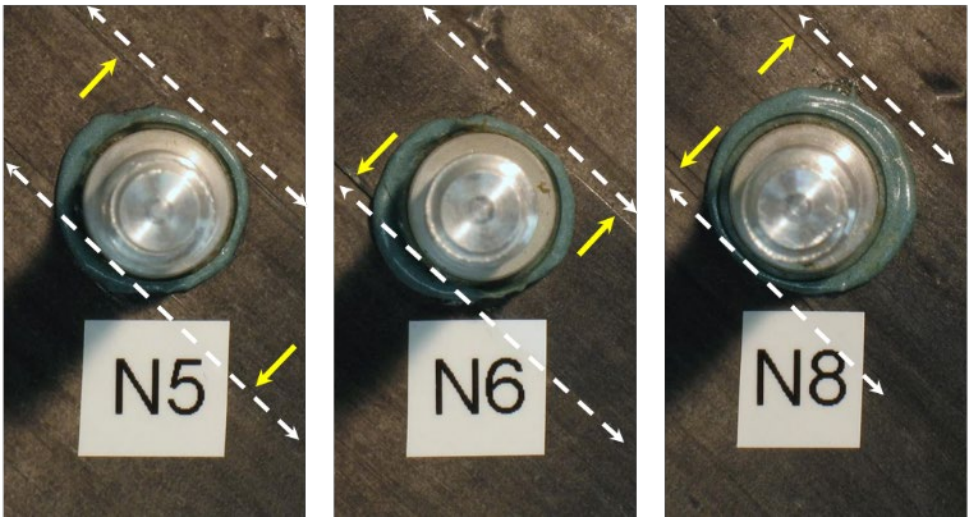

Figure 113. PATTI failure surfaces, with IMR, 2K-Flex (8 hr, 60°C and 10 min, 190°C). Yellow arrows point to the surface crack associated with the delamination;, the dashed lines follow the direction of the cracks.

4.4.4.3.4. Short Beam Shear Strength (Effect of heating and IMR on interfacial strength).
The delamination failures seen in the PATTI composite test specimens that had been exposed to 190°C during their cure cycles prompted further investigation. A second set of ILSS samples were prepared and exposed to 190°C for 30 min. Both of the carbon fiber reinforced Vorafuse™ composite variants, no IMR and with IMR, experienced a reduction in ILLS after heating of 7.2% and 50.1%, respectively (Figure 114).

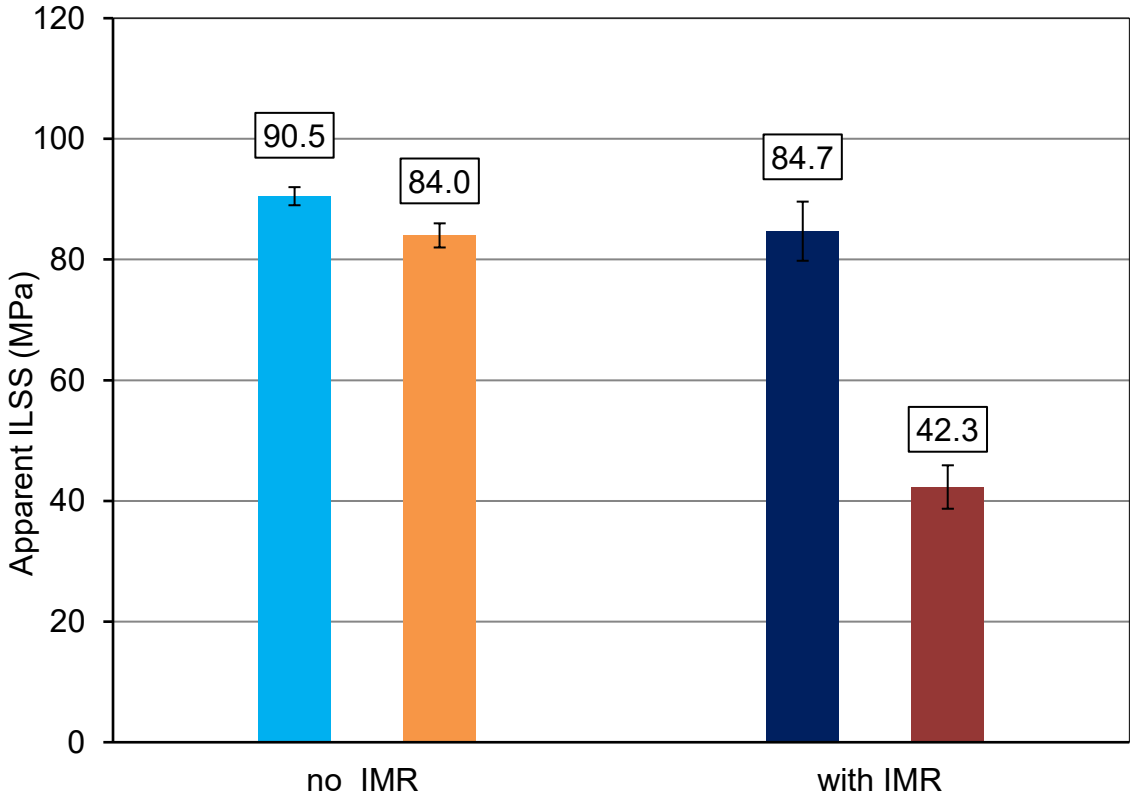

Figure 114. The apparent ILSS of carbon fiber/Vorafuse™ composites with and without IMR, before and after heat treatment at 190°C for 30 min.

4.4.4.4. Results: Primer Adhesion to VORAFUSE M6000 CF-Epoxy Composites

4.4.4.4.1 Surface Treatment and Conditioning
Chopped carbon fiber/Vorafuse™ with IMR composites were used in the primer adhesion experiments. The panels as supplied were 12 in x 12 in. Strips 1 in x 5 in were harvested from one panel to characterize the surface treatment techniques. The remaining panels were sectioned into 5-in x5 in specimens for surface treatment and subsequent priming at Red Spot.

The surface treatments of interest were manual IPA cleaning (baseline), Plasmatreat, and UVO. The degree of modification was determined by the line speed (Plasmatreat) or exposure time (UVO). The line speeds used for the Plasmatreat system are listed in Table 11. Equivalent exposure times for the UVO system were calculated based on the 55-mm footprint of the nozzle.

Table 11 . Plasmatreat line speeds and treatment times, 55 mm nozzle

Line Speed (m/min)	Treatment Time (s)
2.0	1.7
1.0	3.3
0.5	6.6
0.25	13.2

Through the course of this work, water contact angles were measured on materials with and without IMR. The neat resin without IMR had the lowest contact angle, 63.0°, and in fact was the only wettable untreated surface. The water contact angles of the aligned fiber composites with and without IMR increased. Molding conditions may account for the increased contact angle of the aligned fiber composite without IMR versus the neat resin without IMR, 97.0° versus 63.0°, respectively. The chopped fiber composites were only supplied with IMR, their surfaces as well were nonwetting. The results of the contact angle testing are shown in Figure 115.

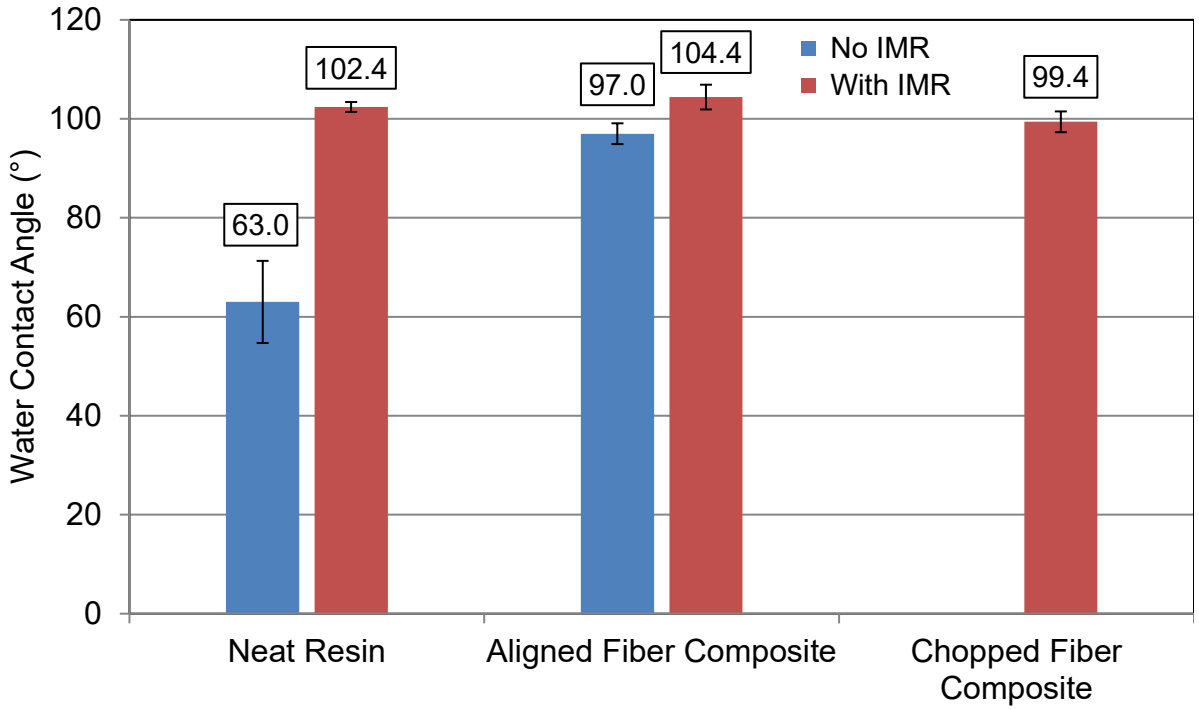

Figure 115. Water contact angles on various surfaces, with and without IMR.

The Plasmatreat system was effective at creating wettable surfaces on the chopped fiber composites at all times studied, Figure 116.

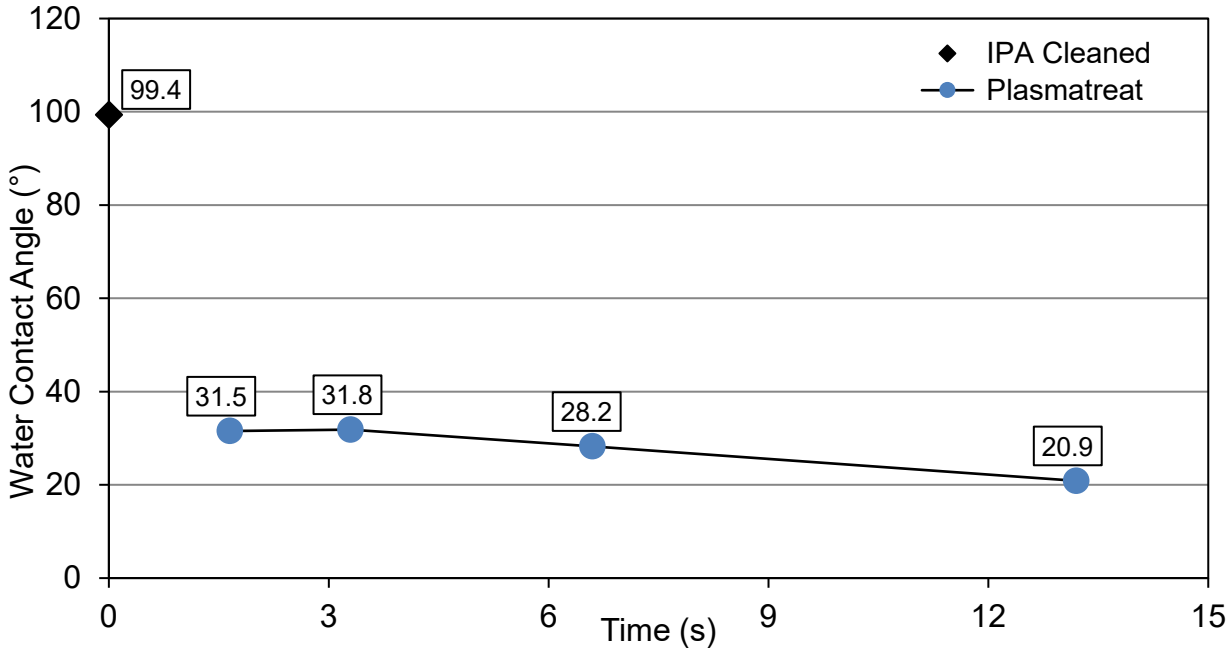

Figure 116. Water contact angles versus treatment time of chopped carbon fiber/Vorafuse™ composite surfaces, Plasmatreat system.

The treated chopped fiber composites were studied using XPS to determine how the oxygen and nitrogen contents of their surfaces changed. The O/C ratio rose quickly and plateaued at just above 0.45, with the nitrogen content increasing for a slightly longer period before leveling off between 0.20 and 0.25, Figure 117.

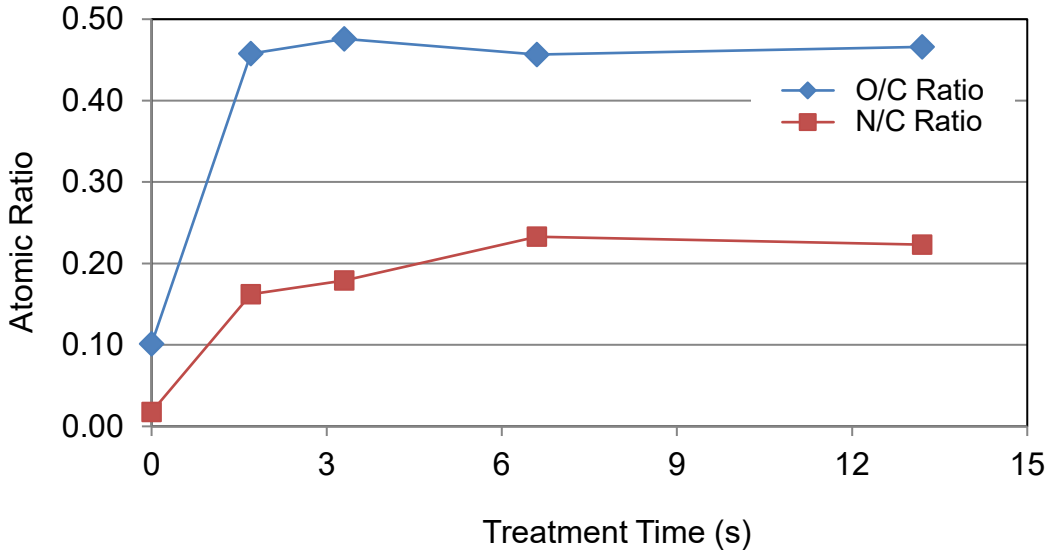

Figure 117. Oxygen and nitrogen content of chopped carbon fiber/Vorafuse™ composite surfaces as a function of treatment time, Plasmatreat system.

The UVO system was able to create a wettable surface at treatment times ≥ 60 s on the chopped fiber composites, Figure 118.

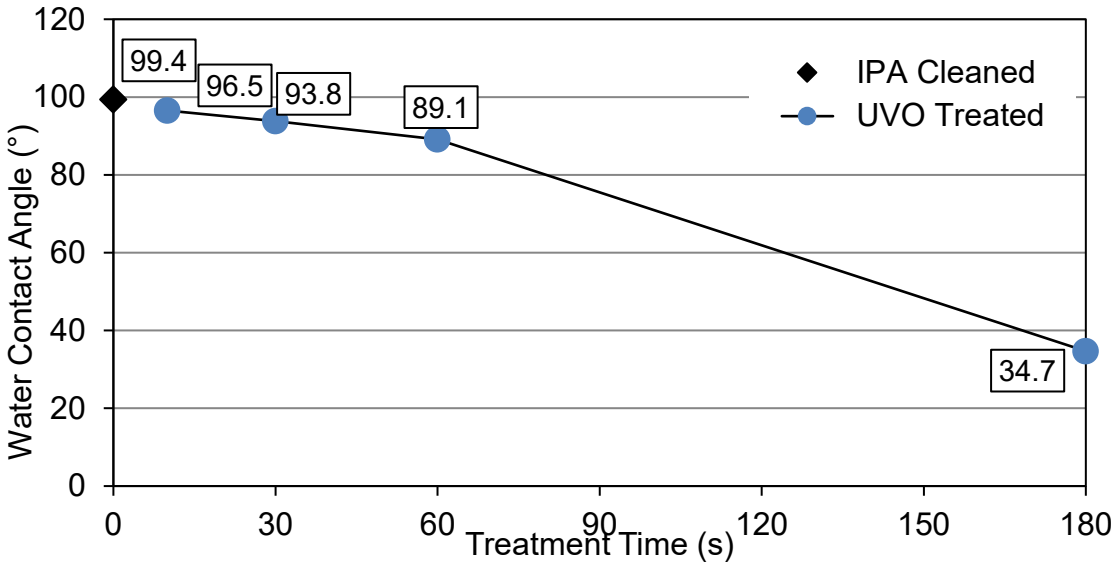

Figure 118. Water contact angles versus treatment time on chopped fiber composite surfaces, UVO system.

The stability of the surface treatments was studied under several conditions. The first was thermal stability after exposure to 190°C for 30 min, Figure 119. It was found that the surface treatment was 'reversed' after this conditioning.

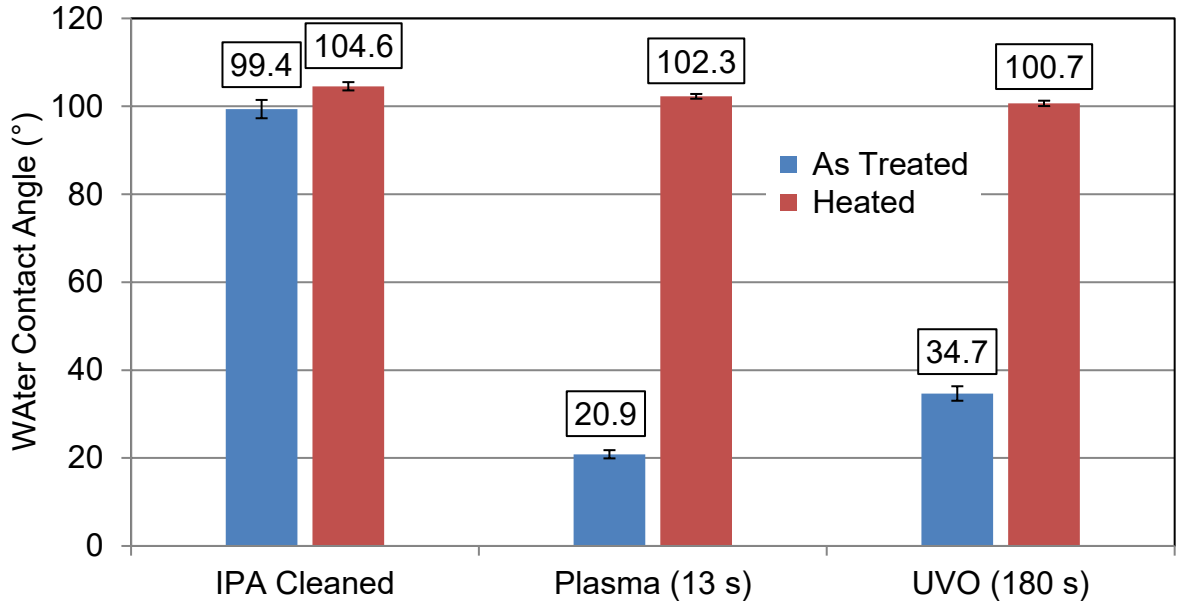

Figure 119. Water contact angles before and after thermal soak (190°C, 30 min).

The long term (> 4 weeks) stability at ambient conditions was also studied, Figure 120. The surface treatment was found to be 'reversed' with aging at room temperature.

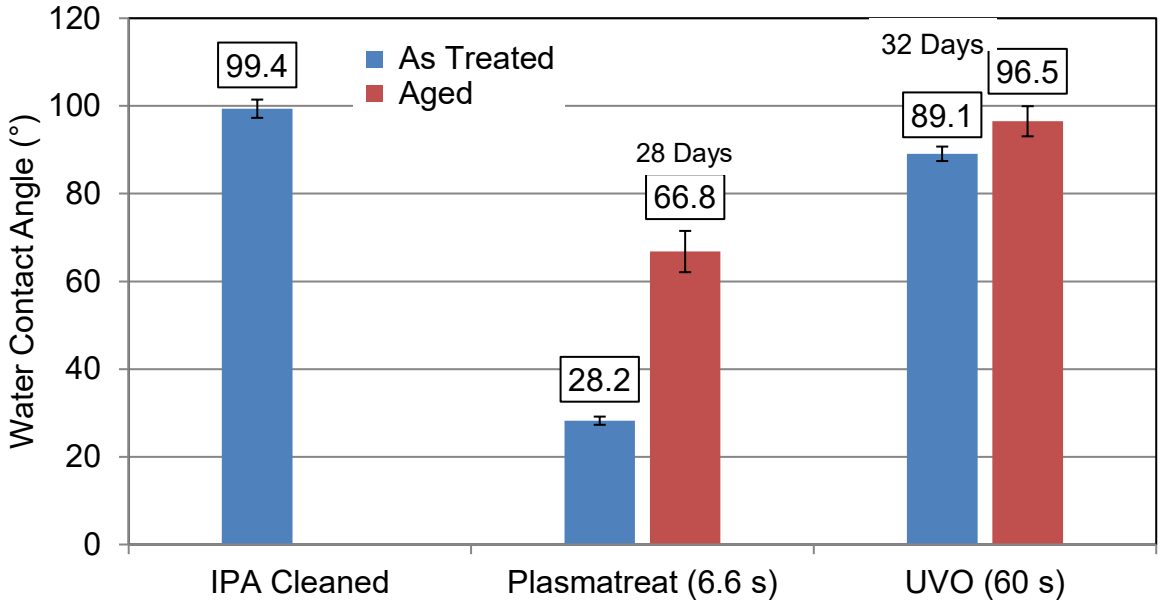

Figure 120. Water contact angles before and after long-term aging at ambient conditions.

Short-term aging at ambient conditions was also studied, Figure 121. It was determined from this study that a 48-hr interval between surface treatment and priming at Red Spot would be acceptable.

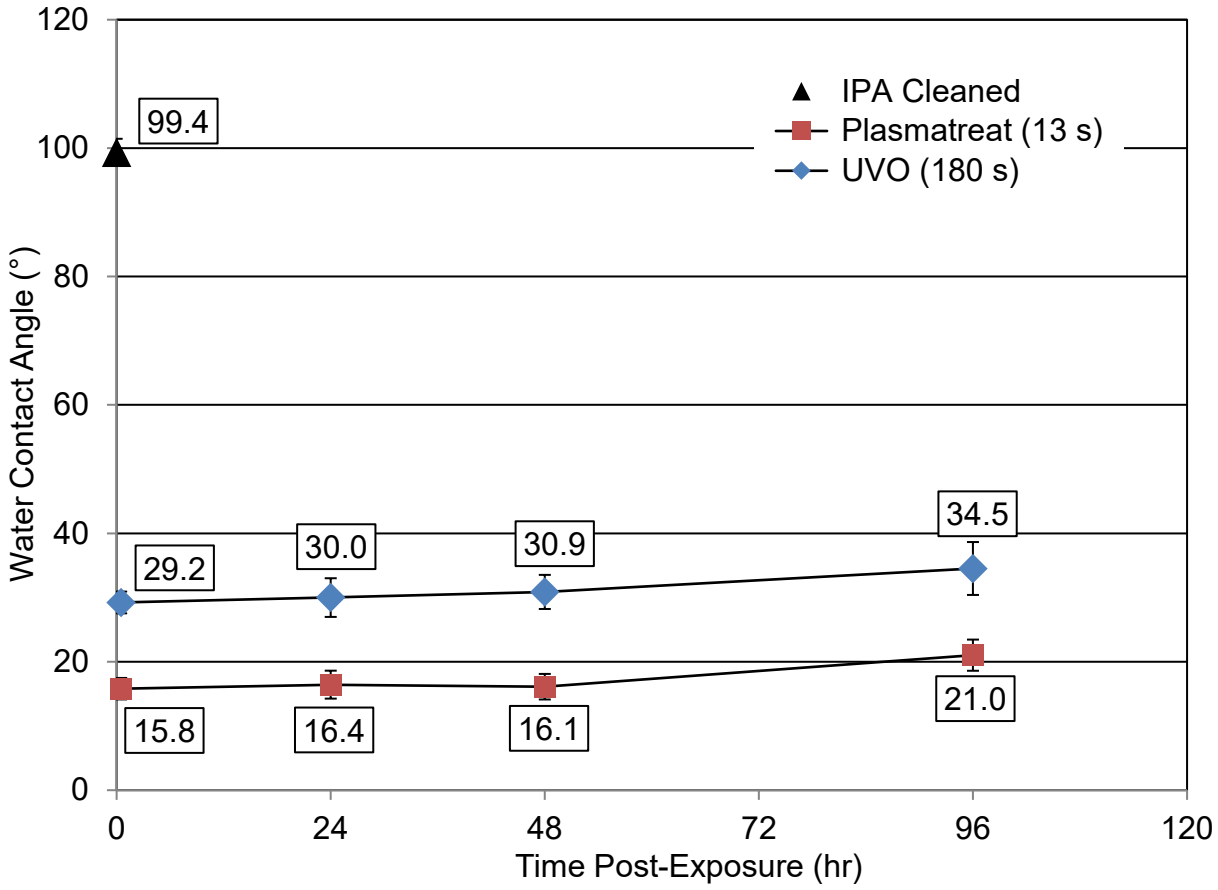

Figure 121. Water contact angles before and after short-term aging at ambient conditions.

4.4.4.4.2 Primer Adhesion after Surface Treatment and Conditioning
For the primer adhesion studies, treatment times of 13.2 and 180 se. were selected for the Plasmatreat and UVO systems, respectively. The chopped carbon fiber panels were sectioned into 5 in x 5 in specimens and all were IPA cleaned. After treatment the samples were individually wrapped in high-purity aluminum foil and sent the same day via next air to the Red Spot facility.

As Primed
Crosshatch adhesion testing was performed on one panel of each surface preparation in the as-primed condition. All tests appeared to be Grade 0; no primer was removed from the surface of the composites, Figure 122.

Figure 122. Crosshatch adhesion test regions, as primed.

Thermal Cycle (Paint Cycle)

The first conditioning cycle studied consisted of exposing the specimens to the thermal cycling that typically follows the application of the primer:

- 30 min, 190°C; cooled 20 min (E-cCoat)
- 20 min, 180°C; cooled 20 min (prime)
- 35 min, 160°C; cooled to RT (paint).

The specimens were wrapped in high-purity foil, taking care that the foil did not touch the primer's surface, and placed in a preheated convection oven for the times indicated. Examination of the panels after this thermal cycling did not reveal any bubbling or delamination as had been seen in the aligned fiber composites used for PATTI testing. All tests appeared to be Grade 0; no primer was removed from the surface of the composites, Figure 123.

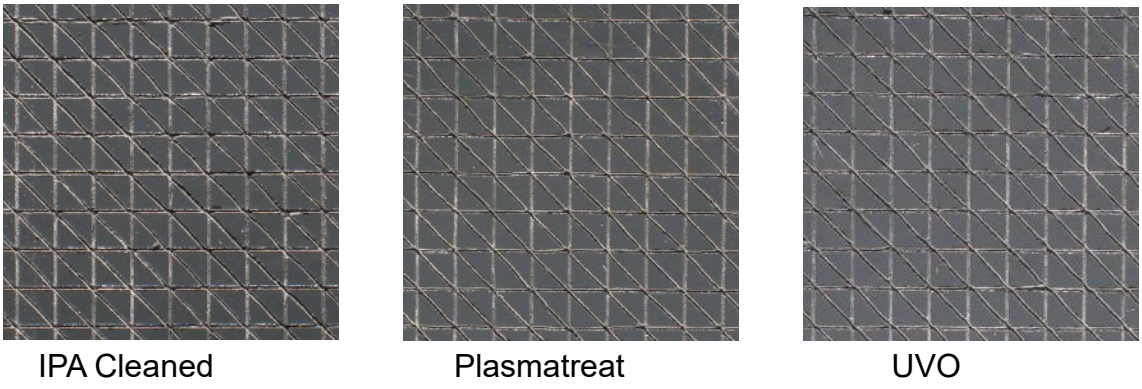

Figure 123. Crosshatch adhesion test regions, thermally cycled.

Thermal Cycle + Water Immersion

Water immersion testing was performed on panels treated with the Plasmatreat and UVO systems. Two "X" scribes were placed in opposite corners before the samples were immersion conditioned for 10 days. After removal from the water bath and drying, changes were noted on both panels.

The Plasmatreat sample had small (< 1 mm) blemishes on its surface, Figure 124.

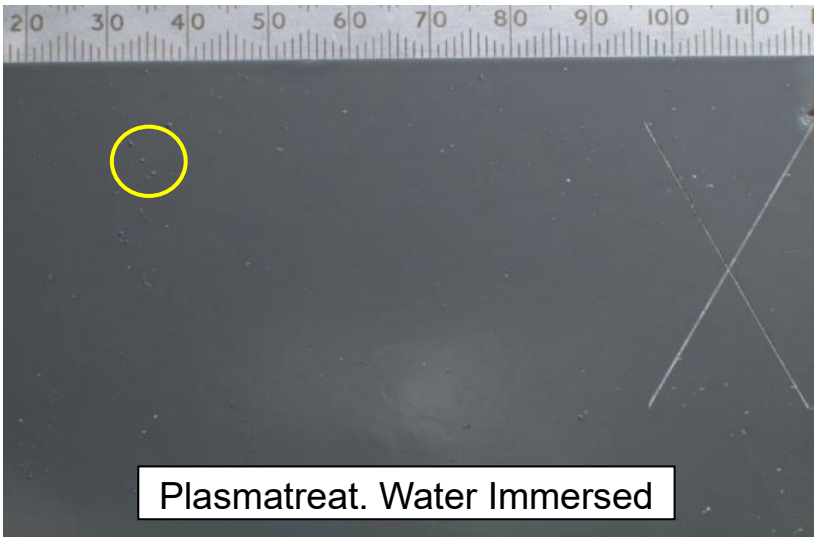

Figure 124. Defects on the surface of a primed panel after water immersion, Plasmatreat system.

The panel treated with the UVO system developed blisters across its surface, Figure 125.

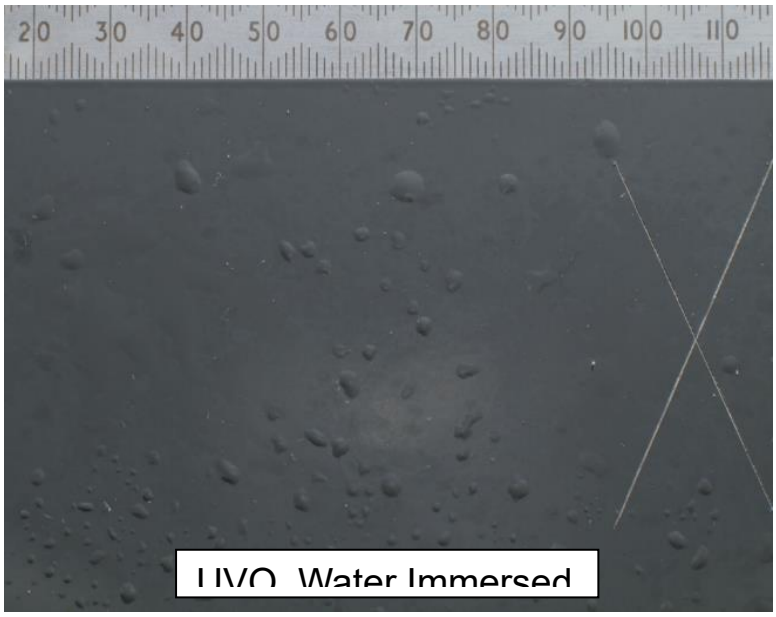

Figure 125. Blisters on the surface of a primed panel after water immersion, UVO system.

The "X-scribe" and crosshatch adhesion testing was performed within 30 min of the samples being removed from the water bath. The adhesion of the primer on the Plasmatreat panel appeared to be unaffected, rated as Grade 0 for the crosshatch adhesion test, Figure 126.

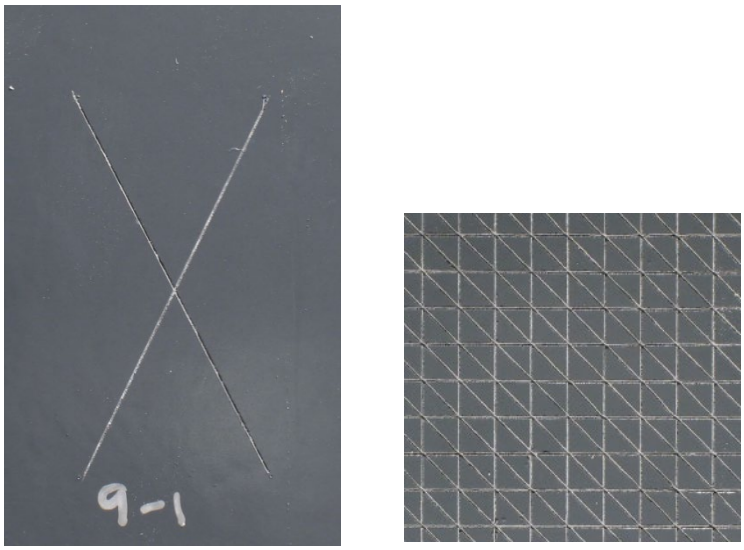

Figure 126. Tested X scribe and crosshatch adhesion test areas, Plasmatreat system.

The adhesion of the primer on the UVO treated panel was affected, rated as Grade 8 for the crosshatch adhesion test (~ 60% removal), Figure 127.

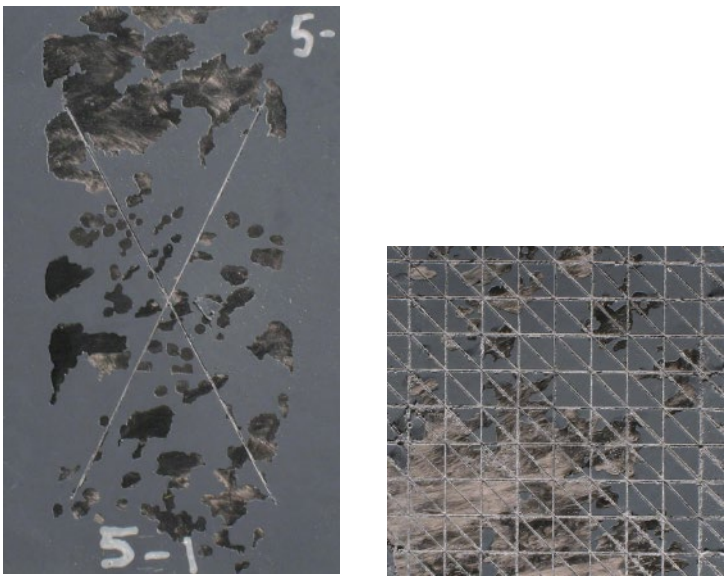

Figure 127. Tested X-scribe and crosshatch adhesion test areas, UVO system.

4.4.5 Discussion and Conclusions from Surface Analysis and Adhesive Bond Durability

The presence of the internal mold release (IMR) as an additive to the epoxy matrix resin of a CF-composite has been investigated for its role in affecting surface and interfacial properties and performance. Specifically,

- Water contact angles measured on the surface of these two systems indicated the neat epoxy produced a wettable surface after curing indicated by a water contact angle range of 63º–97º, while the IMR containing epoxy was nonwettable, giving a water contact angle of 102º–104º (Figure 115).
- Compression molded CF-epoxy plaques fabricated with neat and IMR containing epoxy were tested for tensile and flex properties in the 0º and 90º directions.
    - The 0º tensile and flex modulus was ~ 25% greater for the IMR containing composites. Subsequent cross-section investigation of the composite showed a higher CF volume fraction and closer CF–CF spacing than the system without IMR (Figure 77, 84 85).
    - Interlaminar shear properties using the short beam shear test. The composite without the IMR exhibited ~ 6% greater ILSS (Figure 92).
    - G1c fracture toughness measurements did not show any differences between the samples. Examination of the fracture surfaces showed little difference.
- Adhesion of the cured composites was measured using a pull-off tensile test using the 2K-Flex and 1K-Flex adhesives.
    - The samples with the IMR failed at ~ 40% lower value for the 60ºC cure cycle and ~ 15% lower value after the 190ºC post-cure (Figure 105).
    - The IMR-containing composites failed interfacially and by delamination of the composite surface, while the non-IMR composites failed cohesively in the 2K-Flex (Table 10).
- Adhesion of 2K-Flex and 1K-Flex to aluminum was measured on as-received and IPA-cleaned aluminum.
    - A slight increase in the pull-off test values was measured for the IPA-cleaned surface after both the 60ºC and 190ºC post-cured samples (Table 7).
    - The 1K-Flex adhesive produced identical pull-off values in the as-received and the IPA-cleaned surface conditions, with cohesive failure in the 1K-Flex (Table 6).
- The IMR containing cured composite samples were subjected to surface preparation using a PlasmaTreat process or an Ultraviolet–Ozone treatment process. Both approaches were effective at producing a surface free of IMR and exhibiting increases in surface energy. The water contact angles could be reduced from over 100º (nonwetting) to about 30º (Figures 116, 118).
    - The surface free energy as measured by the water contact angle reverted to ~ 100º for both the PlasmaTreated and UVO-treated composite samples, indicated that the IMR was mobile and could migrate to the surface under the elevated temperature experienced in the paint ovens (Figure 119).
    - Both the PlasmaTreated and UVO-treated composite samples reverted to higher contact angles after ~ 30-day aging at room temperature (Figure 120).

- The kinetic and rheological properties of the adhesives were measured and provided to the Purdue simulation team:
    - Differential scanning calorimetry (DSC) degree of cure as a function of temperature and time (Figures 48–50, 56, 57, 62–66).
    - Rheology as a function of temperature and time (Figures 51,52, 58, 67, 68).
    - Dynamic mechanical analysis (DMA) to measure modulus as a function of temperature and time (Figures 60, 61, 70, 71).

Overall, the presence of the IMR was found to concentrate at the surfaces and interfaces (carbon fiber, prepreg, lamina and cured composite surfaces?) in the CF-epoxy composite. It was also found to be mobile and able to diffuse to surfaces and interfaces over time at ambient conditions and at elevated temperatures expected to be encountered during manufacturing (processing, adhesive bonding, painting) of CF-epoxy composites.

The presence of the IMR decreased the surface energy of the epoxy, changing it from a wettable to a nonwettable surface. As a result, adhesion between the CF and the epoxy was reduced, and shear strength between composite lamina was reduced. It would be expected that the effectiveness of adhesives for part-joining and the durability of paint applied to the cured composite surface would be reduced.

Based upon the data presented, the long-term durability of adhesive joints requires further validation. Application of surface treatments appears to be effective in promoting good bond strength of both adhesives and paint films. Concerns remain, however, over migration of the mold-release agent to these interfaces during service. As a consequence, a further reduction in IMR concentration coupled with an effective surface treatment is recommended to the point where part extraction during the molding process remains feasible without an increase in production downtime or part scrap.

Regarding adhesive selection, both the 1K and 2K options were capable of producing satisfactory bond strengths. However, the distinctly different kinetic and rheology profiles provided the team some options in the prototype assembly process to manage residual stress in the bonded joints when considering dissimilar substrates. As will be shown in Section 4.5, the final selection of adhesive type and the material to be bonded to the CF-SMC have a significant impact on the ability to control warpage and general distortion of the bonded assembly.

4.5. Validation of Material Processing and Performance

To validate the performance of the new carbon fiber SMC system, a couple of rear closure applications were selected for redesign using the CF-SMC material. Target CTQs were used as input into engineering analysis to develop a final design for comparison against the incumbent material system. Figure 128 shows the vehicles selected for this study a Lincoln MKS, with the corresponding decklid assembly, and a Ford Mondeo five-door wagon with a corresponding liftgate assembly. Each of these applications provided an opportunity to assess production feasibility of matching a CF-SMC inner panel with different options for the outer panel. In the case of the Lincoln MKS, the Class A exterior outer panel was manufactured from a glass fiber–based sheet molding compound. On the contrary, for the Mondeo liftgate, the exterior panel was stamped from aluminum sheet. The different material combination provided an opportunity to explore the bonding and assembly options for such a mixed-material closure assembly as it related to processing through a typical vehicle assembly plant paint shop. Due to the significant (5X) increase in thermal expansion of the Al versus the CF-SMC, there were concerns about residual stress in the bond line and distortion of the assembly. Hence, each material combination was examined to determine if a conventional bonding strategy could be applied without further development.

Figure 128. Lincoln MKS and Ford Mondeo demonstrator components.

4.5.1. Decklid Design and Development

Initial attention was placed on redesign of the Lincoln MKS decklid assembly. As Figure 129 indicates, the production release version of the decklid was manufactured from a glass fiber SMC inner and outer combination. Localized steel reinforcements were attached to the inner panel to provide attachment locations for the hinges and latch. For the case of the redesigned decklid, CF-SMC was specified for the inner panel material, in combination with low-density glass fiber SMC outer panel. Note that a transition was also made from a 1.9 g/cm3 standard density outer to a 1.3 g/cm3 low-density outer. This provided additional opportunity for reduction in overall assembly mass. During the manufacturing process, a structural epoxy adhesive was applied to the perimeter of the inner and outer panels to form a bond line on the finished closure assembly. Curing of the adhesive was achieved by subjecting the closure assembly to an elevated temperature cycle.

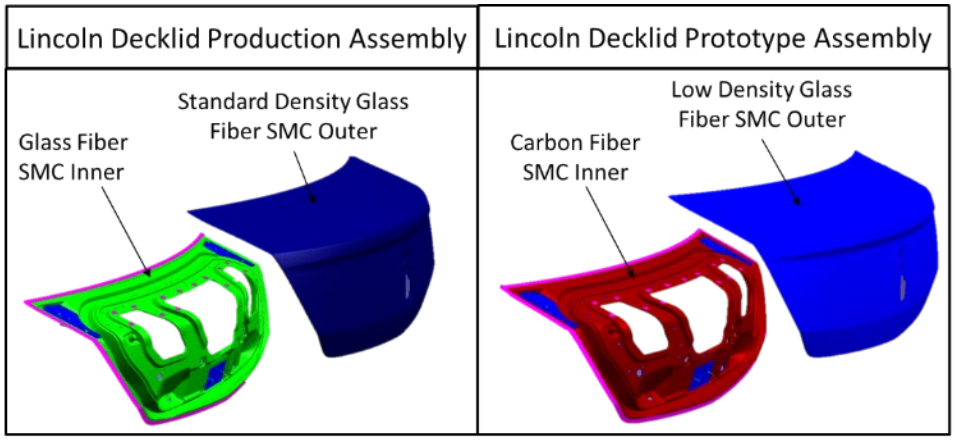

Figure 129. Comparison of production versus prototype carbon fiber SMC decklid assembly.

A series of prescribed load cases were used to guide the design and development of the inner panel. A high-level representation of these is shown in Figure 130. It should be noted that these load cases do not represent a comprehensive set of requirements for the decklid assembly. However, stiffness requirements associated with these loads add useful constraints for early concept development before completing subsequent analysis for a broader set of requirements.

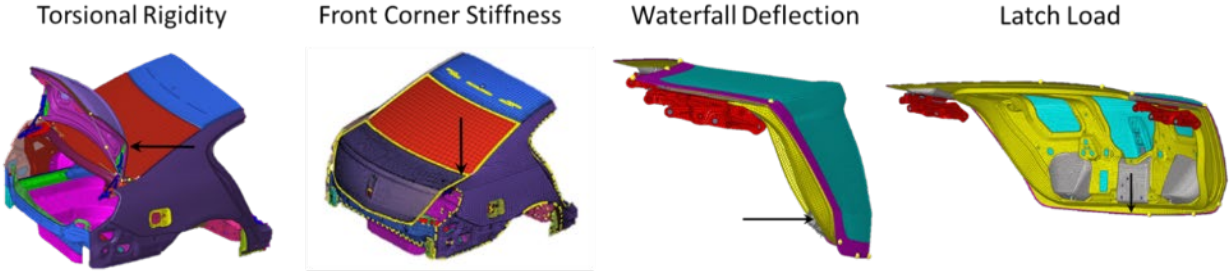

Figure 130. Design load cases used to develop the CF-SMC inner panel design.

Figure 131 shows a comparison of the baseline design versus two designs incorporating the CF-SMC for the inner panel. On the left-hand side of the figure, the inner and outer panel mass for the production release decklid is listed as 10.5 kg. A straight substitution of the inner panel with carbon fiber SMC reduces the mass by 3.17 kg (middle option). This is attributed to the lower density. However, per the properties listed in Table 12, a straight swap with CF-SMC results in an overengineered solution given the stiffness and strength. Hence, the design optimization completed as part of this analysis aimed to maintain equivalent or better performance while downgauging the panel thickness within the limits of manufacturing feasibility. The result on the right-hand side of the figure shows that a further 0.52 kg of mass could be saved, assuming a minimum part thickness of 2.0 mm. That stated, a review of the CAE predictions in Table 12 would suggest that even the optimized design outperforms the baseline by as much as 36%. This would suggest that further scope for weight reduction would be feasible if material could be molded to a thinner gauge. To explore this possibility, follow-up trials were performed later in the project that confirmed that a minimum thickness of 1.5 mm was also achievable.

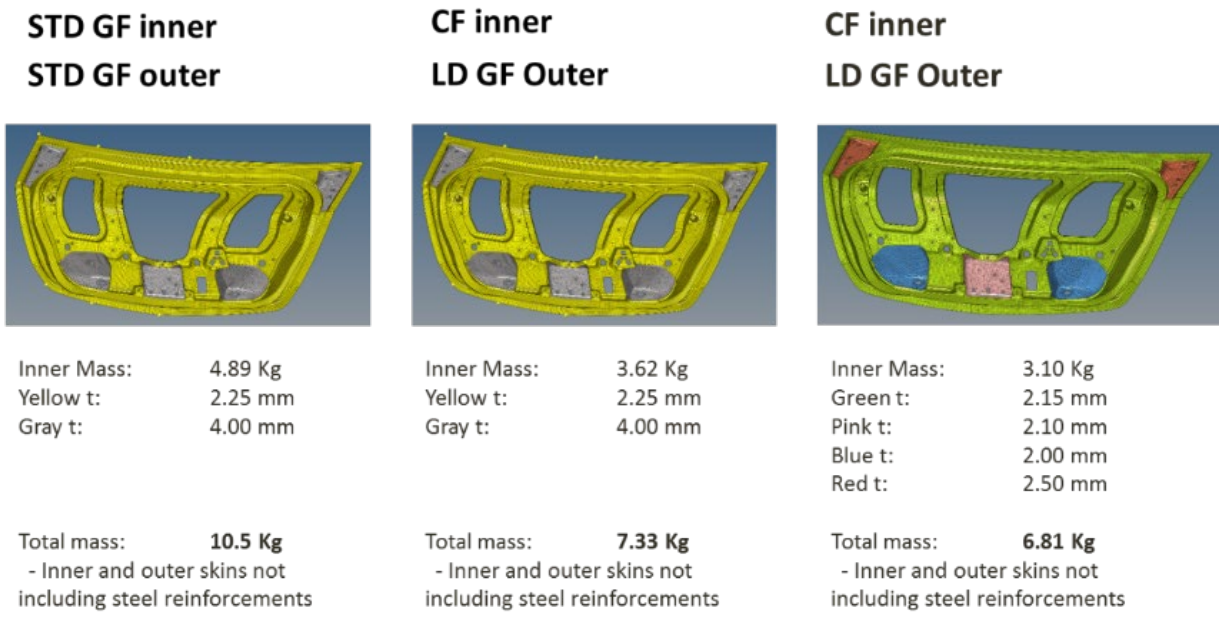

Figure 131. Lincoln MKS decklid baseline design in comparison to carbon fiber inner/glass fiber outer concepts.

Table 12. Summary of Test Results fFor CF-SMC Decklid Assembly

Test	Result units	Baseline vs CF SMC	Baseline vs Optimized CF SMC	Pass/ Fail
Front Corner Deflection	Displacement -Z (mm)	35.8%	28.3%	Pass
Waterfall Deflection	Displacement Z (mm)	47.5%	24.0%	Pass
Latch Loads	Displacement Normal to Surf. (mm)	45.6%	36.3%	Pass
Torsional Rigidity	Angle / meter (degrees/m)	55.0%	30.5%	Pass

4.5.1.1. Prototyping Trials

To validate material performance in a production representative component, decklid inner panels were produced from CF-SMC using molding tools commissioned to supply parts to the original Lincoln MKS vehicle program. The charge pattern used during the prototyping trials was developed based upon the pattern specified for the production glass fiber SMC solution and then modified to account for the lower carbon fiber SMC areal density (Figure 132). This molding tool was used throughout the materials development phase of the project to ensure that the flow and cure characteristics of the epoxy-based compound met requirements. During this stage of the project, approximately 100 parts were produced at Continental Structural Plastics (Tier 1 project partner) to dial in the final material formulation and process setup. This ultimately led to production of five decklid inner panels that were set aside for component and vehicle-level validation testing.

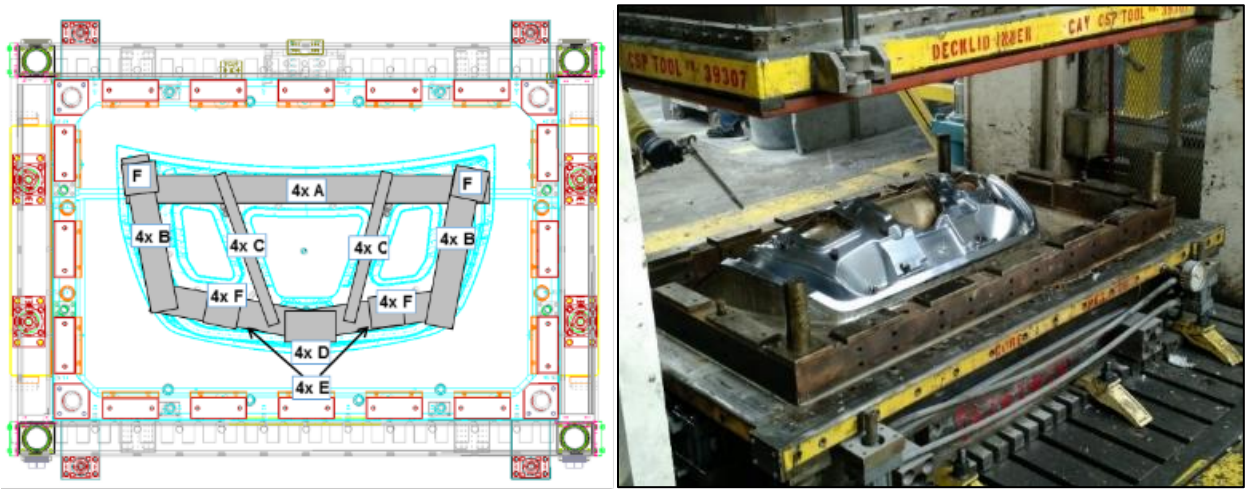

Figure 132. Decklid inner charge pattern and Lincoln MKS decklid inner molding tool.

4.5.1.2 Compression Molding

Figure 133 shows data collected during an example compression molding cycle. A surface-installed thermocouple captures temperature data during the molding cycle. A flush-mounted load cell on the tool surface allows collection of load data that can be converted to pressure measurements. A flush mounted impedance sensor collects resistance data, and the slope of the resulting curve is used to correlate resulting rate and degrees of cure in a molded part. Referring to the example cycle, the temperature starts to drop at the beginning of the cycle once the room temperature blank is placed in the tool. Cavity pressure begins to rise when the tool is closed and machine tonnage is applied. As cavity pressure rises towards the maximum, the temperature of the blank begins to rise and curing begins at approximately 45 seconds, measured by the change in slope of the impedance curve. Approximately 75 seconds into the cycle, the material rate of cure has peaked, and cavity pressure begins to slightly decrease as the part shrinks away from the mold cavity. The impedance curve change in slope approaches zero as the reaction approaches completion, and the tool can be opened at any time after 120 sec. In this case (Figure 133), the tool was opened after 180 secs.

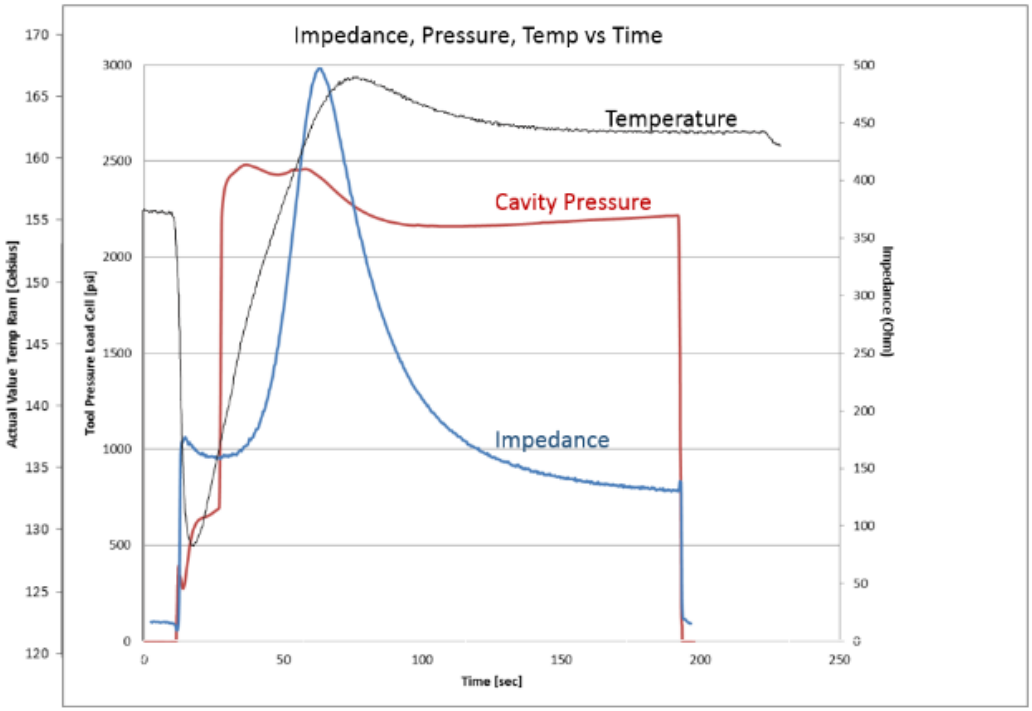

Figure 133. Typical compression molding cycleimpedance, pressure, temp vs time.

The bill of process followed to assemble the decklids for testing is shown in Figure 134. Localized steel reinforcements were attached at the hinge and latch areas using blind rivets and a structural adhesive. The decklid inner and outer panels were then joined using an epoxy adhesive. Although it should be noted that for prototype assemblies, a two-component rather than a single component adhesive was cured at room temperature. Even so, the decklid

assemblies were still subjected to the standard oven thermal cycles for conductive primer, e-coat, primer, and paint. Following the oven cycles, the latch and hinges were installed along with interior trim items.

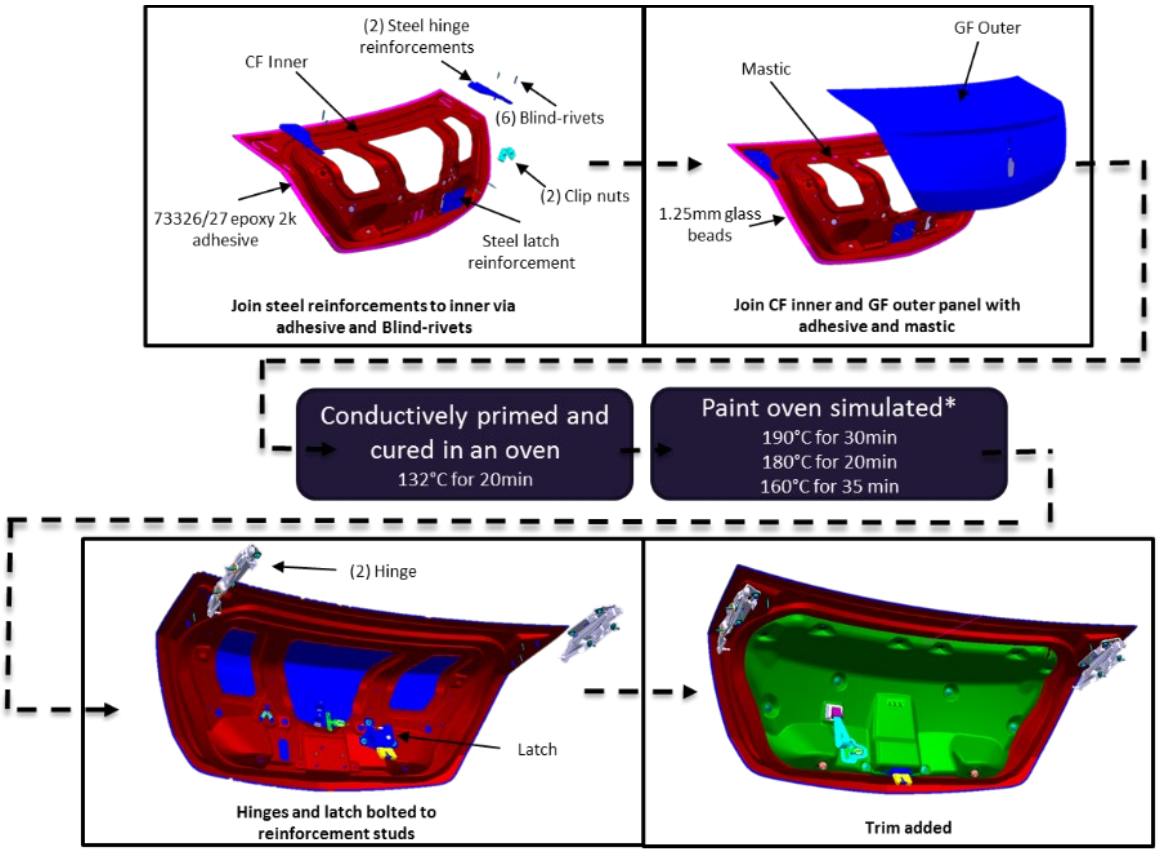

Figure 134. Bill of process for decklid prototype assemblies.

4.5.1.4 Full-scale testing

To complete the design verification process, physical testing of decklids was performed at both the component and vehicle levels. An example of the test setup for the static load cases is shown in Figure 135. For all physical testing, decklids were constrained to match assumptions in the engineering analysis. For full vehicle testing, a drivable test vehicle was procured and the production decklid was replaced with a prototype assembly with the CF-SMC inner panel. As previously stated, it should be noted that the tests performed represent only a subset of all requirements. Additional analysis and testing would be required to fully qualify assemblies for production implementation. However, these key load cases provided significant engineering insight into the performance of the material system under several service load conditions. Following successful completion of all static testing, Figure 136 shows a post-test photograph of a dynamic 55 mph rear crash test completed according to FMVSS301 [27]. While this test is more related to fuel system integrity, this is also used to evaluate the rear crash performance of the decklid assembly as a whole. As Table 13 indicates, all test results met requirements leading

to a successful review of static and dynamic testing in lieu of a final assessment on manufacturing robustness.

Figure 135. Experimental setup for static load cases.

Figure 136. Post-test decklid image from FMVSS301 55 mph rear crash test.

Table 13. Summary of static and dynamic tests performed on the CF-SMC decklid assembly

Component Level Testing		
1. Waterfall deflection	Completed	G
2. Overbend contour (latch loads)	Completed	G
3. Front corner deflection	Completed	G
Vehicle Level Testing		
1. Key Life Test: 50,000 cycle	Completed	G
2. Torsional rigidity	Completed	G
Rear crash test: FMVSS 301	Completed	G

4.5.1.5 Dimensional Analysis

As indicated above, successful completion of physical testing provided confidence that the CF-SMC materials would perform to target requirements. Before the technology could be designated as ready for implementation, however, an evaluation of manufacturing robustness was needed. This included development of corresponding P-Diagrams and FMEAs followed by an assessment of dimensional capability. The images captured in Figure 137 show the conclusions of this analysis as the positions of 27 points around the perimeter of the decklid assembly were compared to nominal CAD. In total, five assemblies were processed through the facility operated by Continental Structural Plastics using production molding and bonding equipment carried over from the Lincoln MKS vehicle program. Of particular relevance was the use of the hot air bonding station to join the inner and outer panels. For production release glass fiber SMC assemblies, this bonding cell had been tuned to meet vehicle fit and finish requirements. Hence, benchmark capabilities were already established and provided an opportunity for comparison against the CF-SMC solution. It should be noted that subsequent to joining the CF-SMC inner panels to the glass fiber SMC outers, decklid assemblies were then subjected to all thermal cycles representative of the regular production process.

The color map in Figure 137 indicates that the sides and trailing edge of the decklid match nominal position with a standard deviation of less than 1 mm. The upper leading edge of the decklid had a? slight crown in the surface, with a standard deviation nominally around 1 mm with a few points exceeding this magnitude. However, overall. the team assessment was that application of some trend setting in the hot air bonding fixture would be able to address any need for adjustment of absolute position at locations 4 through 10. Based upon this conclusion, the physical test program was set as complete, culminating in the receipt of approval from Ford Body Engineering to consider the CF-SMC material on future vehicle programs. Note that this was assumed use of a glass fiber SMC outer panel for the Class A exterior surface.

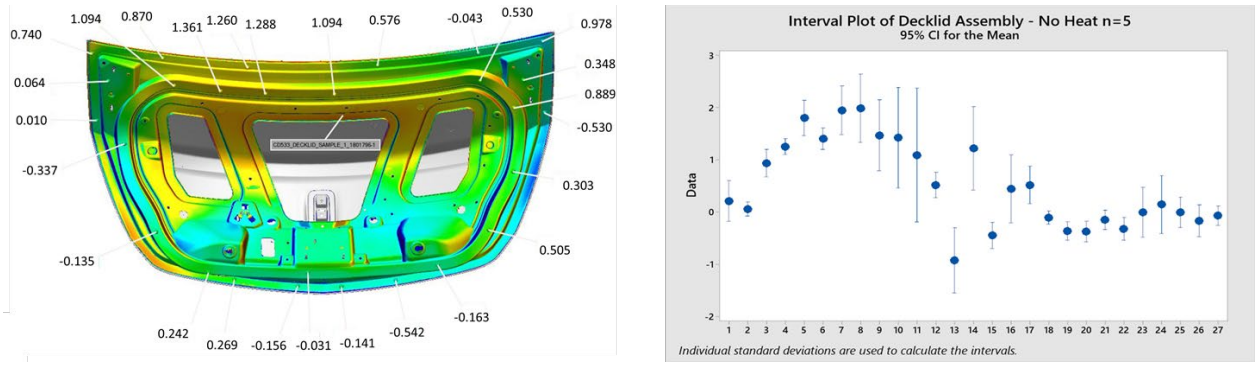

Figure 137. Dimensional assessment of CF-SMC/GF-SMC assemblies after thermal cycling.

4.5.2 Liftgate Closure Development

With validation work on the Lincoln MKS decklid complete, both physical testing and dimensional studies confirmed the potential of using a carbon fiber SMC inner panel in combination with a glass fiber SMC outer panel. While concerns were raised over the mismatch in thermal expansion, data taken from assemblies processed through the standard production process indicated that margin and flushness targets were attainable. Whether or not this could be achieved using carbon fiber SMC in combination with Al outer sheet metal was another question. Therefore, to investigate the viability of this material combination, a redesign of the Ford Mondeo five-door liftgate was completed, replacing the production die cast magnesium inner panel with an equivalent panel produced from carbon fiber SMC. An exploded view of the assembly is shown in Figure 138. To allow use of all carryover hardware and outer panels, key master surfaces and the hemming process for the outer panels were maintained.

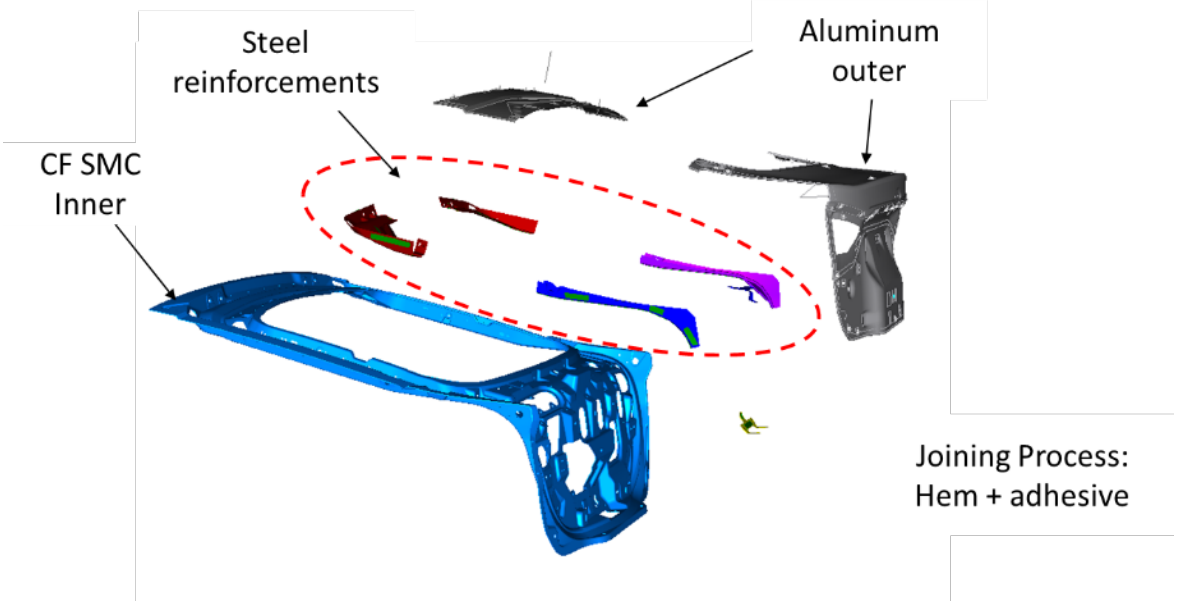

Figure 138. Ford Mondeo liftgate assembly.

4.5.2.1 Prototyping Trials

Molding trials were completed on a 2500T compression press at Continental Structural Plastics and on a 3600T press at IACMI Corktown (Figure 139) to both dial in the processing conditions and produce prototype parts for evaluation. As Figure 140 indicates, and similar to the decklid molding, a 3-min cycle time was demonstrated (tool closure to tool opening). Latitude existed to reduce cycle time further by increasing the mold temperature from 150°C to 160°C. However, a process temperature of 150°C was set to follow the cure profile established through previous trials at Ford. Subsequent to molding, finish machining of the liftgate inner panels was completed prior to buildup of full assemblies for testing.

Figure 139. Liftgate inner panels molded at IACMI Corktown (SURF).

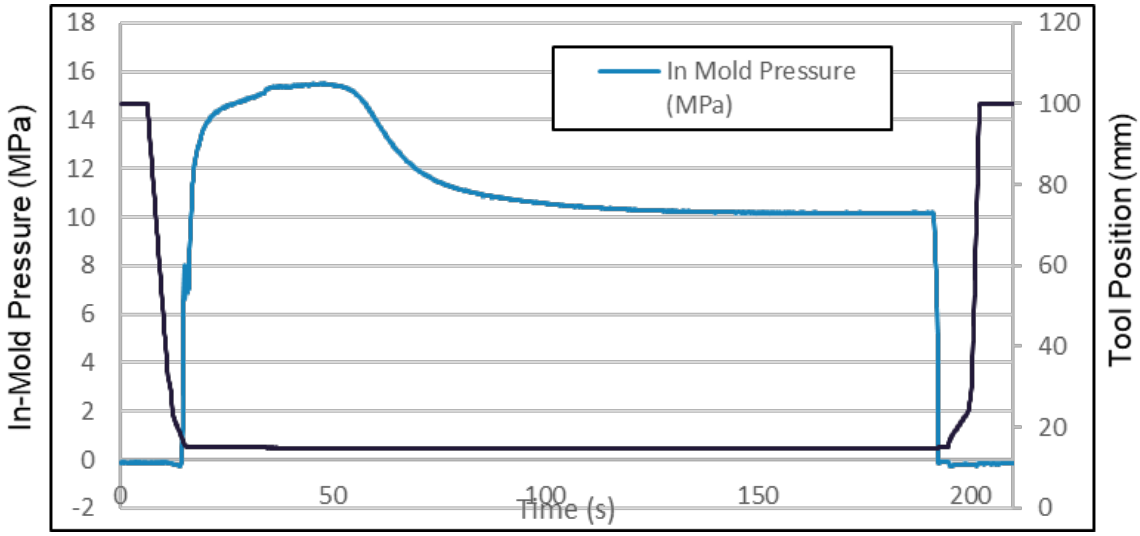

Figure 140. Molding cycle for CF-SMC prototype liftgate inner panels.

4.5.2.. Adhesive Bonding and Cure

A successful ability to bond the CF-SMC inner panel to the two aluminum outers required a review of the adhesive selection and curing strategy. Decisions were required on whether to proceed with room temperature or elevated temperature cure. A room temperature system has the advantage of locking the geometry in place. However, subsequent exposure to the E-coat and paint bake ovens can place considerable stress on the bonded joint. This is influenced largely by the relative stiffness and thermal expansion of the inner and outer panels. Laboratory measurements showed the CF-SMC to have a coefficient of linear expansion between 3.0 to 6.0 x 10^{-6}/C (sample dependent), compared to 24 x 10^{-6}/C for the 6xxx series aluminum outer panels. Hence, in an unconstrained state, the outer panel would normally expand 4 to 8 times that of the composite inner panel. On the other hand, when fully constrained, there is the potential to fail the adhesive bond, as the joint strength diminishes when heated to the oven working temperature (Figure 141). Other disadvantages to room temperature cure include the hold time that is required to avoid relative movement of the inner and outer panels. That stated, techniques such as mechanical fastening or induction cure can be implemented. However, this still creates demand for a substantial manufacturing footprint to store uncured assemblies (work in progress) needed to feed a high-volume production process.

For the reasons above, a single-component adhesive is often a preferred alternative, particularly with common materials for inner and outer panels. In this instance, a geometry setting operation can be executed prior to shipping assemblies directly through the E-Coat and paint baking process. Cure of the bonded joint commences at an elevated temperature below that of the oven working temperature. Hence, given sufficient residence time in the oven, complete cure of the bonded joint can be achieved. For mixed material systems, though, stresses may build in the joint during the cooldown phase of the cycle. Once below the glass transition temperature (T_g), the modulus of the adhesive builds and begins to resist shrinkage of the higher CLTE material. Thus, upon reaching room temperature, significant deformation of the bonded assembly may be evident.

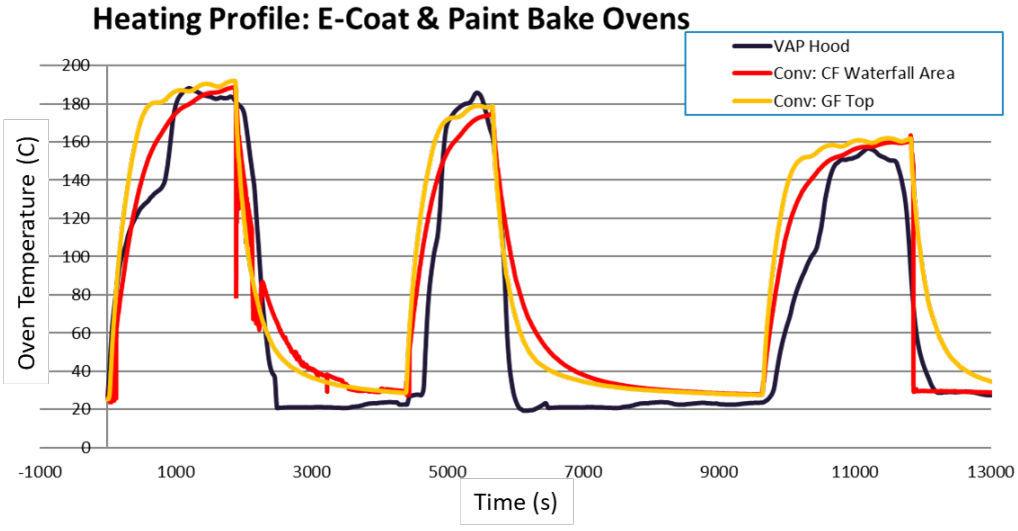

Figure 141. Example e-coat and paint oven heat cycle.

4.5.2.3 Dimensional Analysis

In the case of the liftgate prototypes, a single-component epoxy adhesive system was applied to the first set of assemblies. For baseline purposes, each assembly was transferred to a CMM fixture before a 3D scan of the part was captured. Following initial measurement, assemblies were then mounted onto a fixture to hold the part in vehicle position before transfer to a full-size laboratory oven. Each assembly was then subjected to the thermal cycles shown in Figure 140 before capturing a second 3D scan of the cured assembly. Figure 141 shows an example comparison of the 3D scan before and after the oven cure cycle. The right-hand side of the figure shows the part surface for the post-bake scan in blue compared to the uncured state in tan. Significant distortion of the part is observed, with upper right-hand and left-hand corners rotating further rearward in vehicle position. This is highlighted in the upper two images on the left-hand side of Figure 142. Likewise, the lower edge of the liftgate has also moved further rearward as the profile of the inner panel is distorted to become less concave. Once again, this is highlighted in the magnified images on the left-hand side of the figure. Clearly, displacements of > 7 mm in the top corners of the liftgate and > 15 mm at the lower present a major obstacle when considering the fit and finish of the liftgate assembly into the vehicle body aperture. This also ignores any potential detrimental effects due to the magnitude of the residual stress in the bonded joint. Therefore, further development was required to minimize distortion for this combination of carbon fiber SMC and aluminum outer panels.

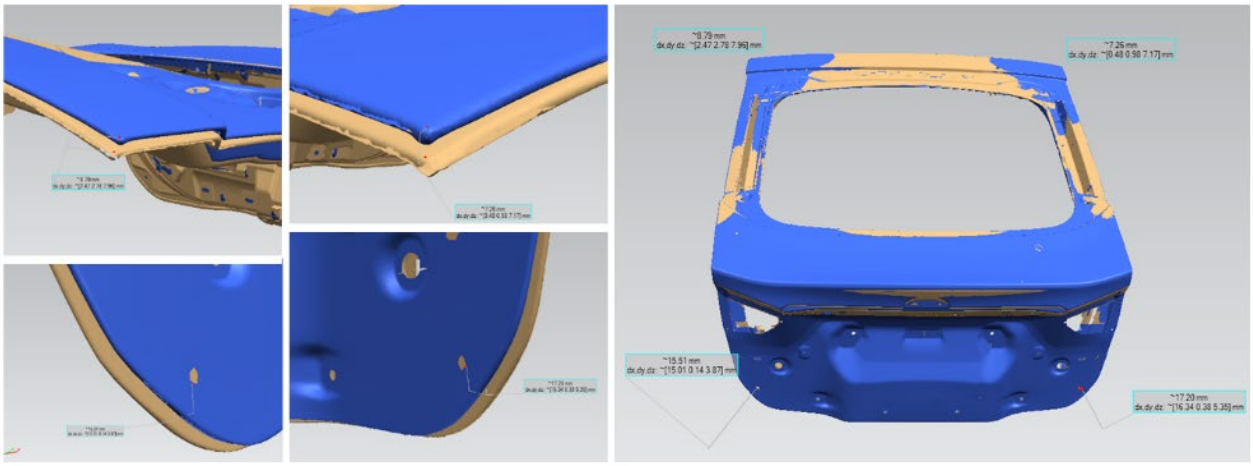

Figure 142. 3D scan of liftgate prototype assembly before and after oven cure.

Strategies to improve dimensional control included the use of localized bonding through techniques such as induction or hot-air impingement heating. The latter already is being used to bond Lincoln MKS decklid inners and outers in the original production assembly. Furthermore, replacement of the structural epoxy with more recent innovations in lower-modulus, more-compliant adhesives would be considered another option. Together with the adoption of a lower temperature bake oven, significant potential exists to maintain dimensional tolerances to within acceptable limits. That stated, the capital requirement and material resources to undertake a development of this nature was too large to be contained within the scope of the project. Therefore, continued validation of the CF-SMC/aluminum closure combination was put on hold until a more comprehensive bonding strategy could be developed. Instead, for the time being,

carbon fiber SMC/glass fiber SMC combination was declared as ready for deployment on future Ford vehicles.

5.0 Major Conclusions

The ongoing drive for improvements in vehicle fuel economy continues to spur innovation in a wide array of vehicle technologies, with vehicle-mass reduction considered a critical element to achieving this goal. The latter has prompted renewed interest in lightweight body and chassis systems that take advantage of advances in materials such as high-strength steel, light metals, and composites. This report summarizes a joint effort by Ford Motor Company, Dow Chemical, Purdue University, Michigan State University, University of Tennessee, and Oak Ridge National Laboratory on the development and implementation of novel carbon fiber composites. The result of this joint development has yielded an epoxy-based prepreg designed for high-volume manufacture. The system enables room-temperature, shelf-stable technology conducive to automated fast manufacturing of composite parts. The performance of these materials was validated in production processing scenarios, culminating in full vehicle testing.

6.0. Acknowledgments

The information, data, or work presented herein was funded in part by the Office of Energy Efficiency and Renewable Energy (EERE), U.S. Department of Energy, under Award DE-EE0006926. The authors also would like to recognize contributions from a broad array of team members at the partner companies and institutes. Throughout the duration of this project the team representing all aspects of research, material development and production have contributed to the success of the program.

7.0 Benefits Assessment

The material and processing technology developed throughout this project aims to support U.S. Department of Energy goals for reducing greenhouse gas emissions and conserving energy. Both of these targets are realized through achievement of substantial mass reduction that results in improvements in fuel consumption for vehicles with internal combustion engines and extended range for battery electric vehicles. These achievements are made feasible due to the increased intrinsic stiffness and strength of the novel carbon fiber SMC derivative. These improvements in mechanical performance have enabled replacement of metallic designs in restricted design spaces that would normally exclude the option for a polymer composite solutions. Consequently, these CF-SMC materials provide a new class of material that meets component performance targets and also provide a high-volume manufacturing pathway that can meet the production throughput demands of a mainstream vehicle program.

8.0 Commercialization

Following a successful gateway review at Ford Motor Company, the CF-SMC material system has been designated as ready for commercial implementation. In practice, this means that the design solutions that feature the carbon fiber SMC material can be formally proposed for inclusion on future vehicle models. That stated, details of future vehicle programs are considered confidential to Ford Motor Company. Therefore, at the time of this publication, the details of components under consideration for future release cannot be disclosed.

9.0 Accomplishments

Throughout the course of this research and development program, the project team was able to successfully develop a full suite of materials and processing technology capable of delivering lightweight automotive structure at high volume. The final form of the VORAFUSE M6400 carbon-epoxy SMC was able to leverage existing infrastructure in the supply base to be processed in a fashion very similar to glass-based SMC. This is achieved using a material that is stable at room temperature while offering a threefold increase in tensile modulus. The resulting properties of materials enable application to a new series of applications that have been off limits due to the inability to design cost effective solutions within the constraints of the design space. Prototype demonstrations on the Lincoln MKS decklid and Ford Mondeo liftgate validated material and process performance and the ability to support the U.S. Dept of Energy's mandate for improved fuel economy and reductions in greenhouse gas emissions. The conclusion of the test program has now led to a material system that has been approved at Ford for future implementation.

10.0. References

[1] S. G. Kravchenko, D. E. Sommer, and R. B. Pipes, "Uniaxial strength of a composite array of overlaid and aligned prepreg platelets," Compos. Part A Appl. Sci. Manuf., vol. 109, no. October 2017, pp. 31–47, 2018.

[2] S. G. Kravchenko, D. E. Sommer, B. R. Denos, W. B. Avery, and R. B. Pipes, "Structure-property relationship for a prepreg platelet molded composite with engineered meso-morphology," Compos. Struct., 2019.

[3] S. G. Kravchenko et al., "Tensile properties of a stochastic prepreg platelet molded composite," Compos. Part A Appl. Sci. Manuf., vol. 124, no. June, p. 105507, 2019.

[4] A. J. Favaloro, B. R. Denos, D. E. Sommer, R. A. Cutting, and J. E. Goodsell, "Manufacturing-Informed Performance of Prepreg Platelet Molding Compound," in Proceeds of CAMX, 2019.

[5] e-Xstream an MSC Software Company, "Digimat MAP."

[6] J. Görthofer et al., "Virtual process chain of sheet molding compound: Development, validation and perspectives," Compos. Part B Eng., vol. 169, pp. 133–147, Jul. 2019.

[7] R. Byron Pipes, R. L. McCullough, and D. G. Taggart, "Behavior of discontinuous fiber composites: Fiber orientation," Polym. Compos., vol. 3, no. 1, pp. 34–39, 1982.

[8] A. J. Favaloro, "Rheological Behavior and Manufacturing Simulation of Prepreg Platelet Molding Systems," 2017.

[9] A. J. Favaloro, D. E. Sommer, B. R. Denos, and R. B. Pipes, "Simulation of prepreg platelet compression molding: Method and orientation validation," J. Rheol. (N. Y. N. Y)., vol. 62, no. 6, pp. 1443–1455, 2018.

[10] A. J. Favaloro, D. E. Sommer, and R. B. Pipes, "Flow Pattern Predictions & Validation for Discontinuous Prepreg Using Anisotropic Viscous Flow Simulation," in Proceedings of the 18th Annual SPE Automotive Composites Conference and Exhibition, 2018.

[11] N. Sharp, J. Goodsell, and A. Favaloro, "Measuring Fiber Orientation of Elliptical Fibers from Optical Microscopy," J. Compos. Sci., vol. 3, no. 1, p. 23, 2019.

[12] G. B. Jeffery, "The Motion of Ellipsoidal Particles Immersed in a Viscous Fluid," Proc. R. Soc. A Math. Phys. Eng. Sci., vol. 102, no. 715, pp. 161–179, 1922.

[13] S. G. Advani and C. L. Tucker, "The Use of Tensors to Describe and Predict Fiber Orientation in Short Fiber Composites," J. Rheol. (N. Y. N. Y)., vol. 31, no. 8, p. 751, Nov.

1987.
[14] S. Kravchenko and B. Pipes, “Virtual tensile testing of prepreg platelet composite molded with stochastic morphology,” in SAMPE 2018, 2018.
[15] R. Cutting, V. Sharma, and J. Goodsell, “Crush Response of Prepreg Platelet Molding Compound Tubes,” in Proceedings of the American Society of Composites, 2018.
[16] R. A. Cutting, J. E. Goodsell, and R. B. Pipes, “Failure Morphology and Energy Absorption of Prepreg Platelet Molding Compound Tubes,” in Proceedings of the Society of Plastics Engineers Automotive Composites Conference and Exhibition, 2018.
[17] Feraboli P, Peitso E, Deleo F, Cleveland T, Stickler PB. "Characterization of Prepreg-Based Discontinuous Carbon Fiber/Epoxy Systems". Journal of Reinforced Plastics and Composites. 2009;28(10):1191-214.
[18] Selezneva M, Lessard L. "Characterization of mechanical properties of randomly oriented strand thermoplastic composites. Journal of Composite Materials". 2016;50(20):2833-51.
[19] Feraboli P, Cleveland T, Ciccu M, Stickler P, DeOto L. "Defect and damage analysis of advanced discontinuous carbon/epoxy composite materials". Composites Part A: Applied Science and Manufacturing. 2010;41(7):888-901.
[20] Feraboli P, Peitso E, Cleveland T, Stickler PB. "Modulus Measurement for Prepreg-based Discontinuous Carbon Fiber/Epoxy Systems". Journal of Composite Materials. 2009;43(19):1947-65.
[21] Feraboli P, Peitso E, Cleveland T, Stickler PB, Halpin JC. "Notched behavior of prepreg-based discontinuous carbon fiber/epoxy systems". Composites Part A: Applied Science and Manufacturing. 2009;40(3):289-99.
[22] Kravchenko SG, Sommer DE, Denos BR, Avery WB, Pipes RB. "Structure-property relationship for a prepreg platelet molded composite with engineered meso-morphology. Composite Structures. 2019;210:430-45".
[23] Benjamin R. Denos SGK, R. Byron Pipes. "Progressive Failure Analysis in Platelet Based Composites Using CT-Measured Local Microstructure". SAMPE2017.
[24] ASTM. ASTM D3039 / D3039M - 17 "Standard Test Method for Tensile Properties of Polymer Matrix Composite Materials". 2017.
[25] Advani S. "The Use Tensors to Describe and Predict Fiber Orientation in Short Fiber Composites". Journal of Rheology. 1987;31(8).
[26] Pradere C, Sauder C. "Transverse and Longitudinal Coefficient of Thermal Expansion of Carbon Fibers at High Temperatures (300–2500 K)" 2008.
[27] U.S Department of Transportation National Highway Traffic Safety Administration, Laboratory Test Procedure for FMVSS 301R, Fuel System Integrity – Rear Impact